

## REVIEW

[View Article Online](#)  
[View Journal](#) | [View Issue](#)Cite this: *J. Mater. Chem. A*, 2020, **8**, 4700Received 25th October 2019  
Accepted 5th February 2020

DOI: 10.1039/c9ta11778d

[rsc.li/materials-a](https://rsc.li/materials-a)An overview of Cu-based heterogeneous electrocatalysts for CO<sub>2</sub> reductionJian Zhao,<sup>a</sup> Song Xue,<sup>a</sup> James Barber,<sup>b</sup> Yiwei Zhou,<sup>a</sup> Jie Meng<sup>a</sup> and Xuebin Ke<sup>a,c</sup>

The electrochemical (EC) reduction of CO<sub>2</sub> is a promising approach for value-added fuel or chemical production. Cu-based electrodes have been extensively used as a 'star' material for CO<sub>2</sub> reduction to hydrocarbons. This review mainly focuses on the recent progress of Cu-based heterogeneous electrocatalysts for CO<sub>2</sub> reduction from 2013 to 2019. Various morphologies of oxide-derived, bimetallic Cu species and their activity in EC CO<sub>2</sub> reduction are reviewed, providing insights for the standardization of Cu-based heterogeneous systems. We also present a tutorial manual to describe parameters for the EC CO<sub>2</sub> reduction process, especially for the pretreatment of the reaction system. This will offer useful guidance for newcomers to the field. Aqueous and non-aqueous electrolyte effects based on Cu electrodes are discussed. Finally, an overview of reaction systems of EC/PEC CO<sub>2</sub> reduction and H<sub>2</sub>O oxidation for Cu-based heterogeneous catalysts is provided.

## 1. Introduction

According to the "World Energy Outlook 2015" from the International Energy Agency (IEA), global energy demand reached 18 TW in 2013 and will increase to 26 TW by 2040.<sup>1</sup> More than 80% of this energy is derived from fossil fuels,<sup>1–3</sup> resulting in a series of problems such as energy supply. Another aspect is environmental issues involving the continuous increase of CO<sub>2</sub>

emissions from fossil fuels combustion, which will increase from 32 Gt up to 44 Gt per year.<sup>1</sup> In terms of alleviating the energy crisis and environmental problems, therefore, there is an increasing demand for recycling CO<sub>2</sub> to produce value-added fuels and chemicals.

In recent years, CO<sub>2</sub> reduction to fuels and chemical products has been investigated by various methods, such as biochemical approaches,<sup>4</sup> building blocks for organic synthesis,<sup>5</sup> thermal hydrogenation,<sup>6–11</sup> photocatalysis,<sup>12–14</sup> electrocatalysis<sup>15–18</sup> and dry reforming with methane.<sup>19,20</sup> Among them, electrochemical (EC) reduction has attracted much attention.<sup>21–23</sup> However, as researchers have acknowledged, electrochemical CO<sub>2</sub> reduction is strongly influenced by the pH<sup>24–27</sup> and conductivity or concentration of electrolyte,<sup>23,28</sup> applied potentials and currents,<sup>29</sup> CO<sub>2</sub> concentration<sup>30</sup> and flow

<sup>a</sup>Tianjin Key Laboratory of Organic Solar Cells and Photochemical Conversion, School of Chemistry and Chemical Engineering, Tianjin University of Technology, Tianjin 300384, China. E-mail: zjtjbd@hotmail.com

<sup>b</sup>Department of Life Sciences, Imperial College London, London, UK

<sup>c</sup>Department of Chemical Engineering, University of Hull, HU6 7RX, UK. E-mail: X.Ke@hull.ac.uk



Jian Zhao is a professor at the School of Chemistry and Chemical Engineering, Tianjin University of Technology. Prior to this, she conducted post-doctoral research at Nanyang Technological University and Singapore University of Technology and Design after receiving her PhD degree from Queensland University of Technology in 2013. Her research area mainly focuses on electro-

chemical CO<sub>2</sub> reduction and photo/thermal heterogeneous catalytic organic synthesis.



Song Xue is a professor at the School of Chemistry and Chemical Engineering, Tianjin University of Technology. Before entering Tianjin University of Technology in 2007, he worked at the Institute of Chemistry, Chinese Academy of Sciences, Beijing. The focus of his research has been the design and synthesis of organic dyes for dye-sensitized solar cells, hole-transporting materials for

perovskite solar cells, and nanomaterials for photochemical conversion of CO<sub>2</sub>.

rate,<sup>30,31</sup> and temperature,<sup>32,33</sup> making a direct, quantitative comparison of data from different groups difficult. To help provide information and to push for a more standardized “benchmark” for EC CO<sub>2</sub> reduction, we provide a tutorial manual for researchers who intend to start EC CO<sub>2</sub> reduction and clearly state the experimental parameters when comparing different systems.

EC reduction of CO<sub>2</sub> is involved in a variety of products ranging from CO, HCOO<sup>−</sup>, HCHO, CH<sub>4</sub>, CH<sub>3</sub>OH, C<sub>2+</sub> hydrocarbons (e.g. C<sub>2</sub>H<sub>4</sub>, C<sub>2</sub>H<sub>6</sub>) and oxygenates, to higher hydrocarbons. The standard potentials for selected CO<sub>2</sub> reduction reactions are listed in Table 1. Since Hori's work in 1989 (ref. 34) and 1994,<sup>35</sup> Cu electrodes have attracted much attention due to their unique advantages for hydrocarbon production compared with other pure metallic electrodes.<sup>36–38</sup> However, a large overpotential is required and low selectivity is observed due to the wide range of products and the competing hydrogen evolution reaction. Numerous publications on Cu-based electrodes have reported a lower overpotential and/or improved product selectivity, especially since 2013, as shown in Fig. 1. Different

selectivity is sometimes reported with similar Cu-based materials. The difference may be caused by the experimental conditions and the material itself, such as the oxidation state of Cu, dimensional structure or surface roughness. Therefore, there is a need to compare these results under certain experimental conditions to further understand their differences and to provide a guide for the development of Cu-based electrocatalysts for CO<sub>2</sub> reduction.

In this review, we first provide a tutorial guide for conducting EC CO<sub>2</sub> reduction experiments. Also, various conditions such as the catalyst state, flow rate and type of electrolyte are specified when comparing studies from different research groups. CO<sub>2</sub> electrocatalysts are usually divided into two categories: homogeneous and heterogeneous systems. Some reviews on molecular electrocatalysts have covered the advantages of homogeneous systems.<sup>39–43</sup> Readers interested in Cu-based complexes could refer to other work.<sup>44–51</sup> Cu-based heterogeneous photocatalysts have been reviewed for direct conversion into solar fuels.<sup>52</sup> In contrast to the reviews of Cu-based heterogeneous catalysts reported for EC CO<sub>2</sub> reduction (review



*James Barber (1940.7–2020.01) was the Emeritus Ernst Chain Professor of Biochemistry, Senior Research Fellow at Imperial College London. He was also the Visiting Canon Professor to Nanyang Technological University in Singapore and the Lee Kuan Yew Distinguished Visitor to Singapore in 2009. Much of his research focused on PSII and the water-splitting process that it catalyzes, and its crystal structure obtained in 2004. His research area also included investigating inorganic systems to mimic PSII in order to develop technology for non-polluting solar fuels.*

yzes, and its crystal structure obtained in 2004. His research area also included investigating inorganic systems to mimic PSII in order to develop technology for non-polluting solar fuels.



*Jie Meng received her B.S. from the School of Chemistry and Chemical Engineering, Tianjin University of Technology. She is currently under the supervision of Prof. Jian Zhao for her Master's degree. Her main area of research is plasmonic gold-based nanomaterials for photocatalytic organic synthesis.*



*Yiwei Zhou received his B.S. from the School of Chemistry and Chemical Engineering, Tianjin University of Technology. He is currently under the supervision of Prof. Jian Zhao for his Master's degree. His main area of research is electrochemical CO<sub>2</sub> reduction and Cu-based nanomaterials for photo/thermal-catalytic organic transformations.*



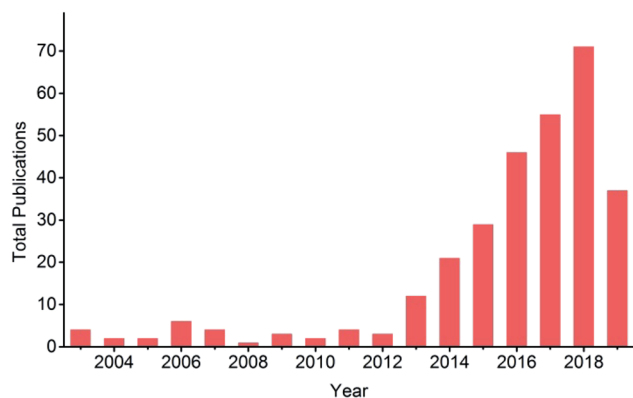
*Xuebin Ke majored in Chemical Engineering and received his BS from Dalian University of Technology (Dalian, China) and his PhD degree from Nanjing Tech University (Nanjing, China). After that he worked at Queensland University of Technology (Brisbane, Australia) for ten years with the continuous support of funding and fellowships. In 2016, he moved to the University of Hull (Hull, UK) to*

*hold a lectureship. He is one of the pioneers who introduced the surface plasmon resonance effect into organic synthesis. His research focuses on materials chemistry, separation science and sustainable process technology.*



**Table 1** The standard potentials for selected CO<sub>2</sub> reduction reactions in aqueous solution at 25 °C and 1 atm

Reactions	$E^0$ (V) vs. NHE (pH = 7)	$E^0$ (V) vs. RHE
$\text{CO}_2 + \text{e}^- \rightarrow \text{CO}_2^{\cdot-}$	−1.90	−1.48
$2\text{H}^+ + 2\text{e}^- \rightarrow \text{H}_2(\text{g})$	−0.42	0.00
$\text{CO}_2 + 2\text{H}^+ + 2\text{e}^- \rightarrow \text{HCOOH}(\text{l})$	−0.55	−0.19
$\text{CO}_2 + 2\text{H}^+ + 2\text{e}^- \rightarrow \text{CO}(\text{g}) + \text{H}_2\text{O}$	−0.52	−0.10
$\text{CO}_2 + 4\text{H}^+ + 4\text{e}^- \rightarrow \text{HCHO}(\text{l}) + \text{H}_2\text{O}$	−0.48	−0.06
$\text{CO}_2 + 6\text{H}^+ + 6\text{e}^- \rightarrow \text{CH}_3\text{OH}(\text{l}) + \text{H}_2\text{O}$	−0.39	+0.03
$\text{CO}_2 + 8\text{H}^+ + 8\text{e}^- \rightarrow \text{CH}_4(\text{g}) + 2\text{H}_2\text{O}$	−0.25	+0.17
$2\text{CO}_2 + 12\text{H}^+ + 12\text{e}^- \rightarrow \text{C}_2\text{H}_4(\text{g}) + 4\text{H}_2\text{O}$	−0.38	0.08
$2\text{CO}_2 + 12\text{H}^+ + 12\text{e}^- \rightarrow \text{C}_2\text{H}_5\text{OH}(\text{l}) + 3\text{H}_2\text{O}$	−0.35	0.09
$2\text{CO}_2 + 14\text{H}^+ + 14\text{e}^- \rightarrow \text{C}_2\text{H}_6(\text{g}) + 4\text{H}_2\text{O}$	−0.28	0.14
$3\text{CO}_2 + 18\text{H}^+ + 18\text{e}^- \rightarrow \text{C}_3\text{H}_7\text{OH}(\text{l}) + 5\text{H}_2\text{O}$	−0.30	0.10

**Fig. 1** Total publication results from a search for title “carbon dioxide electrochemical reduction” or “CO<sub>2</sub> electrochemical reduction”, refined by topic “copper”, across all databases from 2003 to present at Web of Science. Date: 13th July, 2019.

of Cu-based nanocatalysts,<sup>53</sup> review of Cu-binary alloys,<sup>54</sup> review mainly focused on theoretical studies, nanostructured Cu and bimetallics<sup>55</sup>), our review includes a tutorial guide for newcomers, lists the parameters specified by different research groups for comparison (Table 2), summarizes the benchmark activity for special products (Section 3) and covers more types of Cu-based heterogeneous electrocatalysts. Different types of Cu-based heterogeneous electrocatalysts, including film and power systems, will be discussed in five main categories: (1) morphology. Morphology control allows us to improve the catalytic activity by tailoring the structure of active sites and increasing the surface area/number of active sites. (2) Oxide-derived Cu. One recent method to enhance CO<sub>2</sub> reduction is the oxidation and subsequent reduction of Cu. Cu<sub>x</sub>O formed by annealing, electrodeposition, Cl<sup>−</sup> and plasma induction all exhibited improved performance for EC CO<sub>2</sub> reduction after *in situ* or *ex situ* redox processes. (3) Bimetallic species. Alloys are known to be able to tune the geometric and electronic properties of their parent metals. A bifunctional interface (separated composite) without forming an alloy could also improve the performance of each metal while showing fewer changes to the intrinsic electronic properties. The synergistic effects between

different metals could create novel catalytic properties. (4) Surface modification. Modification with inorganic species to enhance durability and organic ligands to capture key intermediates is another strategy to improve the performance of Cu-based electrodes. (5) Supports. Supports or substrates are critical to uniformly deposit the catalyst and create novel catalytic features at the interface. Following these sections, as shown in Fig. 2, the electrolyte effects and the overall reaction systems coupling CO<sub>2</sub> reduction and H<sub>2</sub>O oxidation will be discussed for Cu-based heterogeneous electrocatalysts.

## 2. A note on conducting EC CO<sub>2</sub> reduction

Conducting EC CO<sub>2</sub> reduction may be difficult for many newcomers. A slight oversight will result in the failure of the experiment. Here, we introduce several considerations for conducting EC CO<sub>2</sub> reduction experiments, including pre-treatment of the electrolyte, pre-treatment of the electrolysis cell, flow rate of CO<sub>2</sub> gas and the electrolyte, electrolysis cell type and product analysis.

### 2.1 Pre-treatment of electrolyte

The purpose of electrolyte pre-treatment is to remove any metallic contaminants that might be present. The deposition of metal ion impurities will poison the electrocatalytic activity and cause the deactivation of the Cu electrode.<sup>43,56</sup> This may be also the reason why some beginners observed that almost all the products are H<sub>2</sub>. Proper operation could suppress H<sub>2</sub> evolution, a competing reaction accompanying EC CO<sub>2</sub> reduction.

Pre-electrolysis of the electrolyte is one method, in which two platinum gauzes could be used as the working and counter electrodes in a two-electrode configuration and a negative cathodic potential was applied for certain period (*e.g.* −2 V for 24 h,<sup>57,58</sup> Pt black cathode at 0.025 mA cm<sup>−2</sup> for more than 15 h (ref. 34)). The electrolyte could be also purified by electrolysis between two graphite rods,<sup>59</sup> or two high purity Ti foils (99.99%).<sup>60</sup> Here, the electrodes used should be of high purity and should be removed from the solution before pre-electrolysis





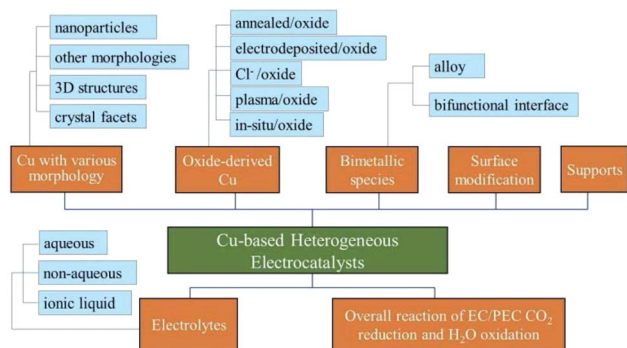


Fig. 2 Diagram of the structure of this review.

stops to avoid recontamination of the electrolyte caused by the dissolution of electrodeposited impurities on the electrode.

Another method is treating the electrolyte with an ion exchange resin (*e.g.* Chelex).<sup>61–63</sup> Generally the ion exchange resin was stirred with the electrolyte for at least 24 h to minimize the concentration of transition metal impurities. During electrolysis, trace metal ions coordinated *in situ* with ethylenediaminetetraacetic acid (EDTA) or *ex situ* with solid-supported iminodiacetate resin should also be considered.<sup>62</sup>

## 2.2 Pre-treatment of electrolysis cell

The purpose of cell pre-treatment is similar to that of electrolyte pre-treatment. Normally the electrochemical cell should first be cleaned with strong acid and finally boiled with de-ionized water (18.2 MΩ cm). For example, it could be sonicated in 20 wt% HNO<sub>3</sub> for 1 h,<sup>64</sup> cleaned in a “nochromix” bath and concentrated HNO<sub>3</sub> for 1 h respectively,<sup>65</sup> cleaned overnight in HNO<sub>3</sub>,<sup>62</sup> or first cleaned by boiling in a mixture of 1 : 1 concentrated HNO<sub>3</sub> and HSO<sub>4</sub> and then boiling in ultra clean water before each experiment.<sup>66</sup>

## 2.3 Flow rate of CO<sub>2</sub> gas and electrolyte

Before the electrolysis experiments, the electrolyte should first be saturated with CO<sub>2</sub> gas by bubbling for at least 0.5 h. Newcomers to the field should pay attention to the pH value before and after CO<sub>2</sub> bubbling as well as the cation size (*e.g.* NaHCO<sub>3</sub>, KHCO<sub>3</sub>, *etc.*), since both these parameters have effects on the selectivity of products. The pH of 0.1 M, 0.2 M, 0.3 M and 0.5 M KHCO<sub>3</sub> saturated with CO<sub>2</sub> is 6.8, 6.9, 7.0 and 7.2 respectively. More information on the electrolyte effect is discussed in Section 5.

During electrolysis, there are three types of CO<sub>2</sub> gas and electrolyte flow: (1) continuously bubbling CO<sub>2</sub> during the process,<sup>31,60,62,63,67–84</sup> (2) CO<sub>2</sub> bubbling plus flow electrolyte<sup>58,85–87</sup> (the CH<sub>4</sub>/C<sub>2</sub>H<sub>4</sub> ratio could be tuned by varying the CO<sub>2</sub> gas and KHCO<sub>3</sub> electrolyte flow rates),<sup>58</sup> (3) no report of any form of convection at all.<sup>33,88</sup>

The unit of flow rate is standard cubic centimetres per minute (sccm) or ml min<sup>−1</sup>. Certain flow rates of CO<sub>2</sub> gas were chosen by different research groups, such as 5 sccm,<sup>63,67–72</sup> 10 sccm,<sup>73–76</sup> 20 sccm (ref. 60, 77–84) and 30 sccm. The cell design and catalyst itself should also be considered when choosing the

flow rate. The Takanabe group<sup>73</sup> chose 10 sccm to ensure sufficient CO<sub>2</sub> supply to the electrode surface while preventing the catalyst dropping off the electrode by gas bubbles. The Koper group<sup>31</sup> investigated the influence of CO<sub>2</sub> flow rate on the activity of 3D porous hollow fibre Cu and observed a maximum FE of 75% CO at −0.4 V vs. RHE when flow rate >30 sccm. In a flow setup, the flow rate of the CO<sub>2</sub> gas was set to 50 sccm and that of the electrolyte was 100 sccm.<sup>85</sup> To suit a specific system, one could also choose to adjust the flow of electrolyte with the applied potential.<sup>86</sup>

With CO<sub>2</sub> gas bubbling, the catholyte could be stirred.<sup>62,89,90</sup> The rotating rate also has an influence on the catalyst activity.<sup>30</sup> H<sub>2</sub> evolution increased and the product selectivity switched from CH<sub>4</sub> to CO when the rotating rate was increased, although there was increased availability of CO<sub>2</sub> at the electrode surface. This was caused by the enhanced mass transfer of dissolved CO away from the electrode surface and then less adsorbed CO was left for further reduction.<sup>90</sup>

## 2.4 Electrolysis cell types

A variety of cells have been reported in the literature, but the most commonly used is a H-type cell. The total number of publications from 2007 to 2017 on selected metal-based electrocatalysts for CO<sub>2</sub> reduction in H-cell experiments was 1083, and 21 in continuous flow reactors.<sup>91</sup> In a typical H-type cell, two compartments are separated by an activated ion exchange membrane such as a Nafion membrane (*e.g.* Nafion@117 with 0.180 mm thickness and >0.90 meq g<sup>−1</sup> exchange capacity). The Nafion membrane should be activated first, usually by boiling in 3–5 wt% H<sub>2</sub>O<sub>2</sub>, DI water, 0.5 M H<sub>2</sub>SO<sub>4</sub> and DI water at 80 °C, respectively, for 0.5–1 h. The working electrode and reference electrode are in the cathode compartment with a CO<sub>2</sub> gas inlet and outlet. The counter electrode is in the anode compartment with or without a gas inlet and outlet.

## 2.5 Product analysis

Gas chromatography (GC) with a thermal conductivity detector (TCD) and a flame ionization detector (FID) is a universal method for gas product analysis. FID with a methanizer is normally used to quantify CO, CH<sub>4</sub>, C<sub>2</sub>H<sub>4</sub> and C<sub>2</sub>H<sub>6</sub>, and TCD is used to quantify H<sub>2</sub>. It is also able to detect a mixture of 100 ppm CO and 100 ppm H<sub>2</sub> with TCD, and 50 ppm CH<sub>4</sub>, 50 ppm C<sub>2</sub>H<sub>4</sub> and 50 ppm C<sub>2</sub>H<sub>6</sub> with FID, as shown in Fig. 3. High performance liquid chromatography (HPLC) and nuclear magnetic resonance (NMR) are used for detecting liquid products. For example, methanol, ethanol, formate and acetic acid products could be quantified by 1D <sup>1</sup>H NMR with DMSO as an internal standard (Fig. 4). More detailed information on gas and liquid product detection can also be found in other reviews.<sup>92,93</sup>

Faradaic efficiency (FE) is the ratio between the amount of product actually detected by an analysis technique such as GC, HPLC or NMR, and the amount of product theoretically formed based on the charge passed during electrolysis. The faradaic efficiency or selectivity for each product in EC CO<sub>2</sub> reduction could be calculated according to the following equation:

Without CO<sub>2</sub> gas bubbling during electrolysis:



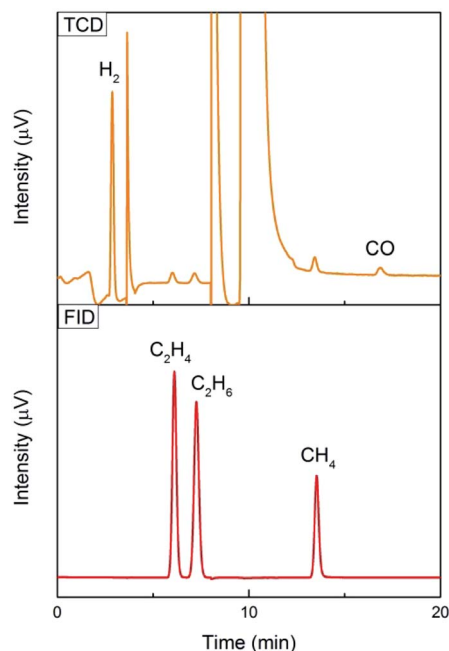


Fig. 3 100 ppm CO and 100 ppm H<sub>2</sub> tested with TCD, and 50 ppm CH<sub>4</sub>, 50 ppm C<sub>2</sub>H<sub>4</sub> and 50 ppm C<sub>2</sub>H<sub>6</sub> tested with FID using an online GC system for one-time injection.

$$\text{Faradaic efficiency (FE)} = \frac{n}{Q/ZF} = \frac{nZF}{Q}$$

$n$  is the amount of product detected (number of moles, mol);  $Q$  is the total charge passed through the system, recorded during electrolysis (coulombs, C);  $F$  is the Faraday constant (96 485 C mol<sup>-1</sup>);  $Z$  is the number of electrons required to obtain 1 molecule of the product. As shown in Table 1, the number of electrons required to form 1 molecule of CO, CH<sub>3</sub>OH, CH<sub>4</sub>, C<sub>2</sub>H<sub>4</sub> and C<sub>2</sub>H<sub>6</sub> is 2, 6, 8, 12 and 14, respectively.

CO<sub>2</sub> gas was continuously bubbled during electrolysis (the first and second measurements are not used to calculate faradaic efficiency to ensure that the data is from a system under equilibrium conditions):

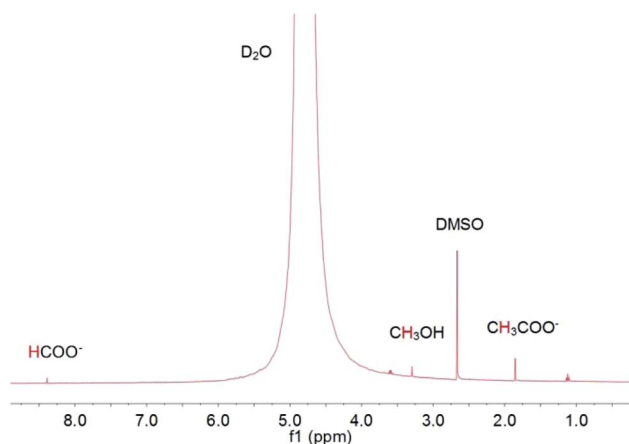


Fig. 4 1D <sup>1</sup>H NMR analysis of methanol, ethanol, formate and acetic acid products with DMSO as internal standard.

$$\text{Faradaic efficiency (FE)} = \frac{nZF}{Q} = \frac{nZF}{It} = \frac{nZF}{IV/\nu}$$

$I$  is the recorded current (A);  $t$  is the time required to fill the sampling loop (s);  $V$  is the volume of the sampling loop (cm<sup>3</sup>);  $\nu$  is the recorded flow rate (ml s<sup>-1</sup>).

As stated, therefore, the most important thing for newcomers before conducting EC CO<sub>2</sub> reduction in aqueous electrolyte is the pre-treatment of the reaction system. Otherwise, H<sub>2</sub> may be the sole product rather than CO<sub>2</sub> reduction products, as the potential needed for water reduction to H<sub>2</sub> is less negative than that for CO<sub>2</sub> reduction. In addition, attention should be paid to the flow and convection state of CO<sub>2</sub> gas and the electrolyte to make sure that all the experiments are conducted under certain conditions for comparison.

### 3. Significant progress in the study of Cu-based heterogeneous electrocatalysts for EC CO<sub>2</sub> reduction

Before a detailed summary and comparison between the work of different research groups, we provide here the benchmark activity of Cu-based heterogeneous electrocatalysts for each EC CO<sub>2</sub> reduction product (Fig. 5). Significant progress has been made in C<sub>1</sub> and C<sub>2</sub> products, whereas the selectivity for C<sub>3</sub> and C<sub>4</sub> products is relatively low. New insights into the mechanistic study of Cu are also given in Fig. 5 (orange). According to the reported studies, C<sub>3+</sub> products are rarely formed and we will focus on the mechanisms for C<sub>1</sub> and C<sub>2</sub> products. Most mechanisms agree that the first step involves the adsorption/activation of CO<sub>2</sub>.<sup>55,110–113</sup> Various adsorption or activation geometries have been proposed, which are reduced to CO and HCOO<sup>-</sup>, respectively. The adsorption intermediate on Cu *via* a carbon or oxygen atom is the key distinction governing the selectivity of CO or HCOO<sup>-</sup>. Therefore, altering the adsorption site and/or the stability of the adsorption intermediate is crucial for the formation of either CO or HCOO<sup>-</sup>. On the Cu surface, CO is adsorbed long enough to react further, forming HCHO, CH<sub>3</sub>OH, CH<sub>4</sub> and C<sub>2</sub> products. Fig. 6 shows the three most likely pathways from adsorbed \*CO. Two pathways have been identified for the formation of C<sub>2</sub> products, \*CO dimerization for \*C(O)(O)C\* intermediates at low overpotentials and \*CO hydrogenation for \*CHO intermediates at high overpotentials. High pH values will favour the major C<sub>2</sub>H<sub>4</sub> pathway (plain red arrows) and low pH value will favour the CH<sub>4</sub> pathway (plain blue arrows). Additionally, these intermediates are sensitive to the Cu structure and composition, supports and electrolyte, which will be discussed in detail in the next section.

### 4. A brief review of Cu-based heterogeneous catalysts for EC CO<sub>2</sub> reduction

#### 4.1 Cu with various morphologies

In order to improve the activity of Cu-based electrodes, diverse morphologies have been investigated and developed,



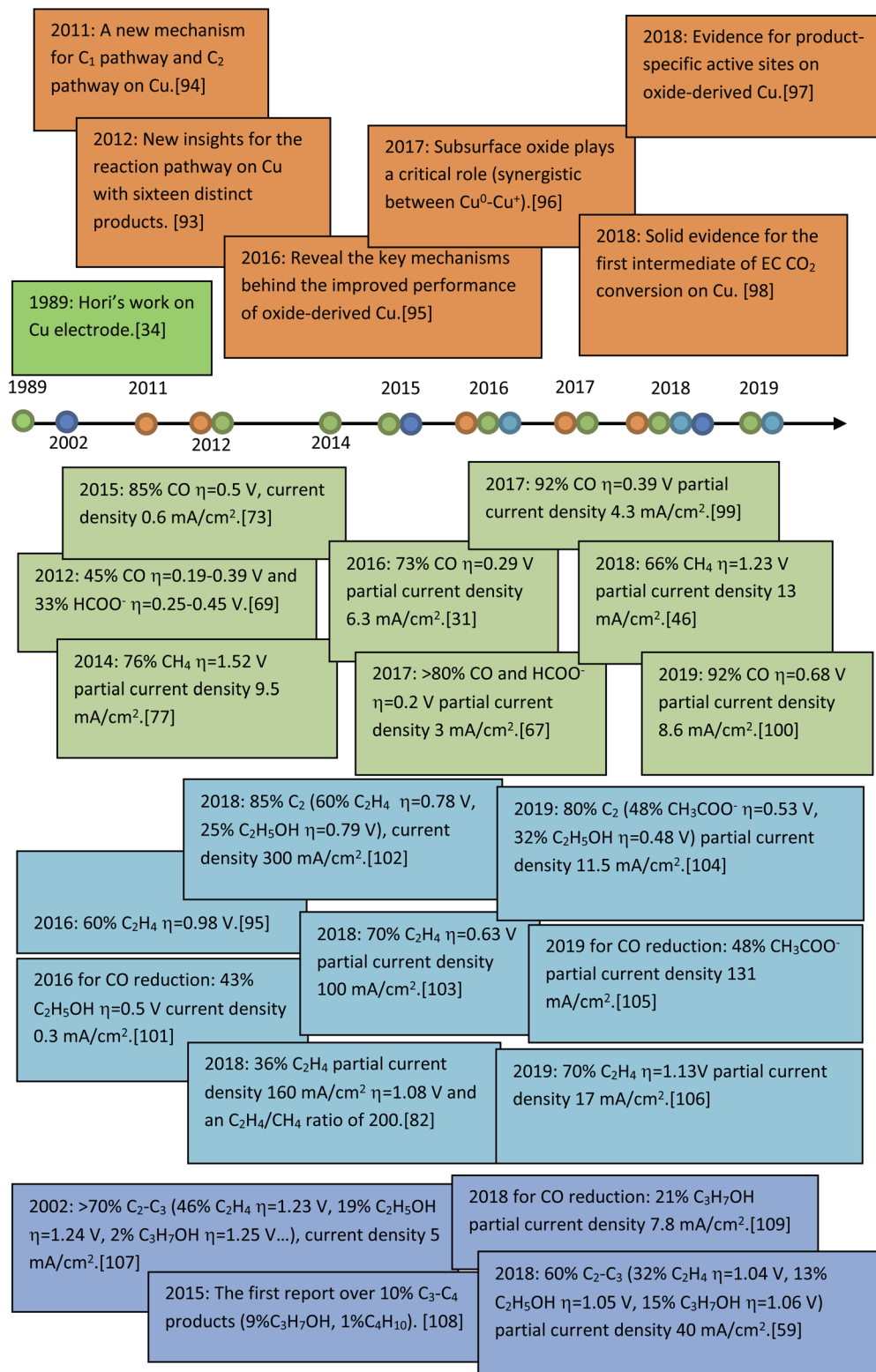


Fig. 5 The benchmark activity and progress of mechanism studies on Cu-based heterogeneous catalysts for EC CO<sub>2</sub> reduction.

including nanoparticles, nanocubes, nanoneedles, and three-dimensional (3D) structures. The relevant surface roughness, size effects, interparticle spacing, nanoparticle loading level and crystal-facets are explored for these various morphologies.

**Nanoparticles.** Compared with smooth Cu, its roughened counterpart could provide a high electrochemical surface area to enhance the current density for CO<sub>2</sub> reduction. By pretreating polycrystalline Cu foil *via* electropolishing, electrochemical cycling (50–100 nm Cu nanoparticles) and argon sputtering, I.



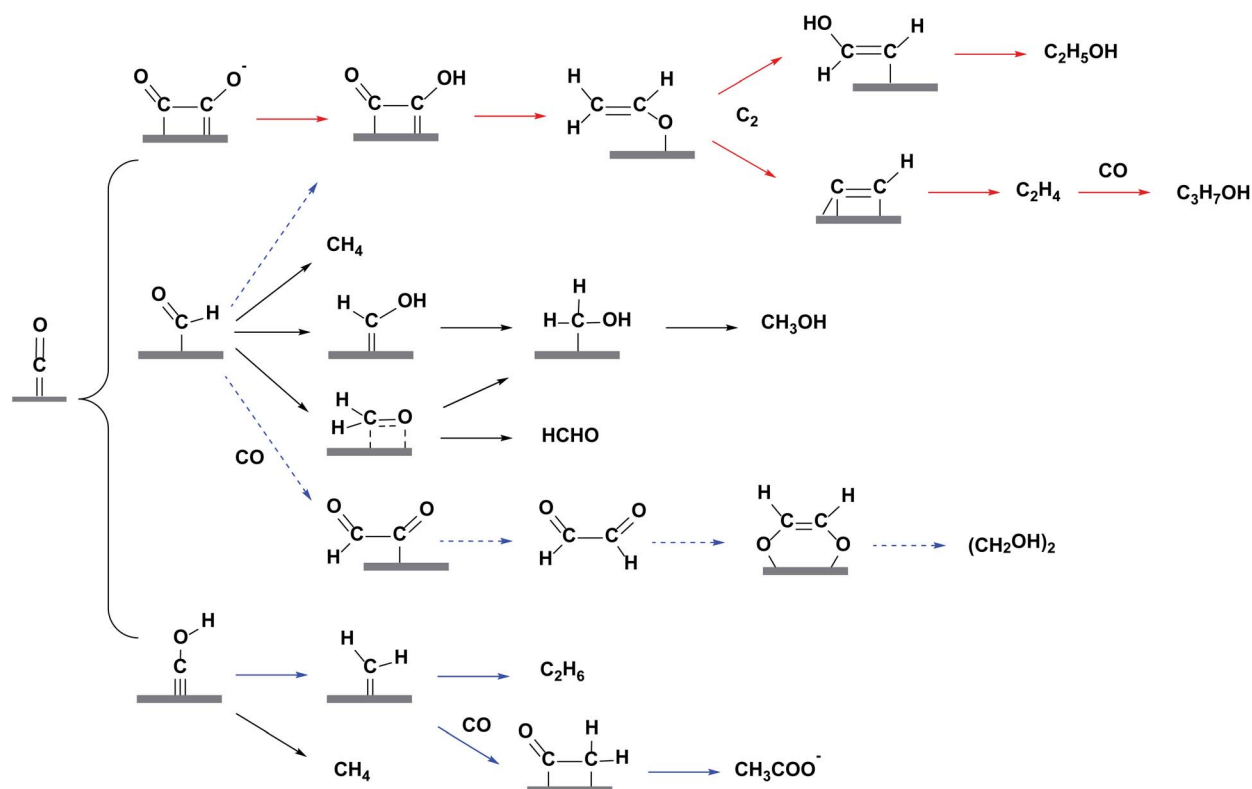


Fig. 6 Most likely reaction pathways from adsorbed  $\ast\text{CO}$  on Cu surface for  $\text{C}_1$  and  $\text{C}_2$  products. Plain red, plain blue and dashed blue routes are for major, minor and trace  $\text{C}_2$  products.

Chorkendorff and co-workers<sup>114</sup> found that high surface roughness showed higher activity for hydrocarbon formation ( $\text{CH}_4$  and  $\text{C}_2\text{H}_4$ ) in  $\text{KClO}_4$  electrolyte. The enhanced activity was ascribed to the greater abundance of undercoordinated sites on the roughened surfaces. The high activity of the roughened surface of Cu nanoparticles was also reported by H. M. Zhang, X. F. Li and co-workers.<sup>115</sup> In their work, Cu nanoparticles with a diameter of 100 nm (thickness 47 nm) were coated on carbon paper *via* pulse electrodeposition.

Compared with constant potential electrodeposition, pulse electrodeposition created a more roughened surface to provide abundant active sites, leading to 85%  $\text{CH}_4$  formation at  $-2.1$  V vs. RHE ( $0.5$  M  $\text{NaHCO}_3$ ,  $1$  sccm  $\text{CO}_2$ ). According to these studies, the promoting effect of the roughened surface on  $\text{C}_2\text{H}_4$  and/or  $\text{CH}_4$  formation is independent of the catalyst preparation method and the electrolyte used for  $\text{CO}_2$  reduction.

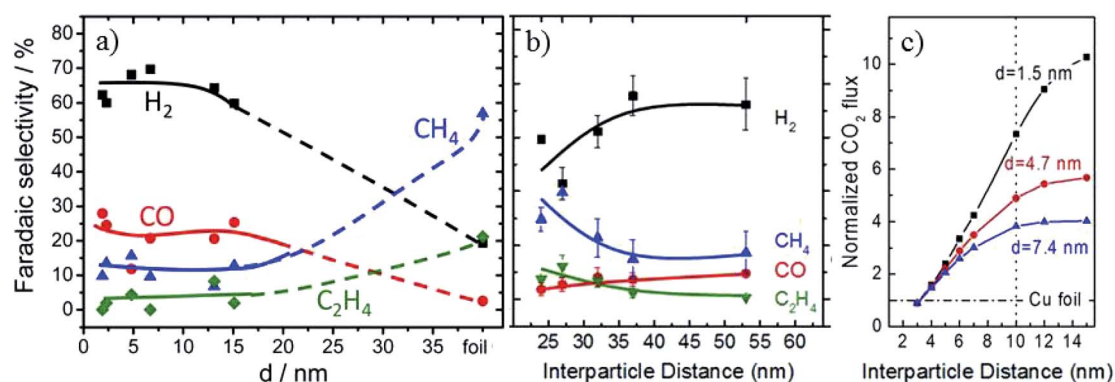


Fig. 7 (a) The faradaic efficiency of reaction products during EC  $\text{CO}_2$  reduction on Cu nanoparticles. (b) The faradaic efficiency as a function of interparticle distances over  $4.7$  nm Cu nanoparticles. (c)  $\text{CO}_2$  flux obtained for Cu nanoparticles with different sizes and interparticle distances based on diffusion equations. Experimental conditions:  $0.1$  M  $\text{KHCO}_3$ ,  $-1.1$  V vs. RHE,  $30$  sccm  $\text{CO}_2$ . Reproduced from ref. 65 for (a) and ref. 119 for (b) and (c), with permission from the American Chemical Society, 2014 and 2016.



Particle size is a critical parameter in tuning the activity and selectivity of Cu nanoparticle catalysts. It may be difficult to control smaller particle sizes and interparticle distances directly *via* an electrochemical method. Therefore, although powder systems have to be assembled into electrodes for further application in CO<sub>2</sub> reduction, many studies have been reported based on Cu powder systems with a controlled small particle size. ~5 nm Cu nanoparticles embedded in a thin film of metal organic framework (MOF, used to restrict the particle size) on fluorine-doped SnO<sub>2</sub> (FTO) exhibited 31% (major HCOO<sup>−</sup>, minor CO) CO<sub>2</sub> reduction selectivity at −0.82 V *vs.* RHE (0.1 M NaClO<sub>4</sub>, pH = 4.6).<sup>116</sup> B. R. Cuenya, P. Strasser and co-workers<sup>65</sup> prepared Cu nanoparticles with a mean size range of 2–15 nm on glassy carbon. The hydrocarbon production decreased as the particle size decreased and vanished for sizes ≤2 nm, as shown in Fig. 7a. Cu nanoparticles (12 nm, 19 nm, 24 nm, 37 nm)/four types of carbon support also showed higher C<sub>2</sub>H<sub>4</sub>/CH<sub>4</sub> production than smooth copper film, and smaller particle sizes were more favorable for C<sub>2</sub>H<sub>4</sub> formation (pH = 6.8).<sup>117</sup> These individual studies give different trends for product distribution, probably caused by different preparation methods, supports and pH of the electrolytes.

Another critical parameter for Cu nanoparticle catalysts is the interparticle spacing.<sup>118</sup> B. R. Cuenya and co-workers<sup>119</sup> designed 1.5 nm, 4.7 nm and 7.4 nm Cu nanoparticles with interparticle distances of 10–22 nm, 24–53 nm and 41–92 nm, respectively. Smaller interparticle spacing was favorable for re-adsorption of the CO intermediate and its further reduction to hydrocarbons, and with the increase of interparticle spacing the CO<sub>2</sub> flux increased, as shown in Fig. 7b and c. P. Strasser and co-workers<sup>120</sup> also showed that C<sub>2</sub>H<sub>4</sub> selectivity could be tuned by particle density caused by diffusional interparticle coupling that controlled CO desorption/re-adsorption and in turn the effective CO<sub>ad</sub> coverage. Recently, it was also reported that stacked small Cu nanoparticles could be formed by *in situ* electrochemical fragmentation during the CO<sub>2</sub> reduction, promoting C–C coupling reaction.<sup>121</sup>

The Cu nanoparticles loading level also has a significant influence on the morphology evolution and product selectivity.<sup>77</sup> P. D. Yang and co-workers<sup>122</sup> assembled densely packed Cu nanoparticles (6.7 nm) on carbon paper electrode. These densely packed nanoparticles changed to cube-like structures intermixed with smaller nanoparticles (Fig. 8a). Compared with spatially separated nanoparticles and *ex situ* prepared nanocubes, the *in situ* formation of cube-like particles from densely packed nanoparticles suppressed C<sub>1</sub> products and improved C<sub>2</sub>–C<sub>3</sub> formation (C<sub>2</sub>H<sub>4</sub>, C<sub>2</sub>H<sub>5</sub>OH, and *n*-C<sub>3</sub>H<sub>7</sub>OH 50% at −0.75 V *vs.* RHE, Fig. 8b).

Therefore, small interparticle distances and densely packed nanoparticles would lead to higher hydrocarbon formation. The above Cu nanoparticles are crystalline in form. Compared with the crystalline form, the amorphous form seems to be more favourable for C<sub>2</sub> products. J. M. Yan and co-workers<sup>78</sup> synthesized amorphous Cu nanoparticles (average size 3.3 nm), and achieved 37% HCOOH and 22% C<sub>2</sub>H<sub>5</sub>OH at −1.0 V *vs.* RHE (0.1 M KHCO<sub>3</sub>, 20 sccm CO<sub>2</sub>). The crystalline Cu nanoparticles

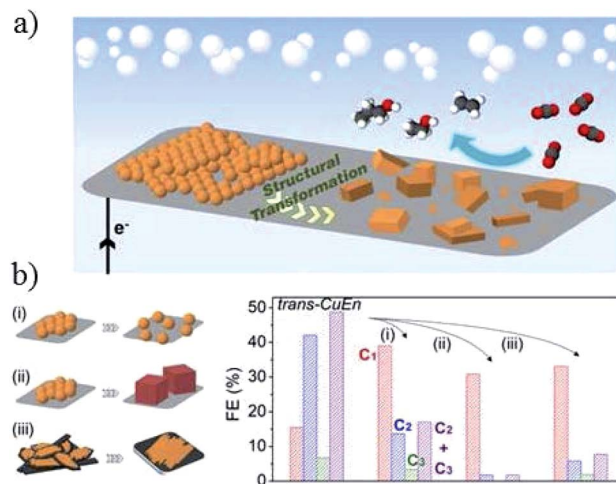


Fig. 8 (a) Schematic illustration of Cu nanoparticle ensembles as an active catalyst for C<sub>2</sub>–C<sub>3</sub> product formation. (b) Investigation of the parameters affecting structural transformation of Cu nanoparticle ensembles and their catalytic activity. (i) Separation of the NPs from their initial densely packed assembly, (ii) use of Cu nanocubes as starting materials, and (iii) change of support to a low surface area carbon plate. Experimental conditions: 0.1 M KHCO<sub>3</sub>, (i) −0.84 V, (ii) −0.86 V, and (iii) −0.81 V *vs.* RHE, respectively. Reproduced from ref. 122.

(average size 3.4 nm) only showed 26% HCOOH and no C<sub>2</sub>H<sub>5</sub>OH at the same potential. They ascribed the enhanced activity to the high electrochemically active surface area (ECSA) and CO<sub>2</sub> adsorption on the amorphous surface.

Similar to Cu nanoparticles formed on film *in situ* as an electrode, the morphology of powder nanoparticles could also have an effect on product selectivity, and a surface morphology with more defects and boundaries promotes C<sub>2</sub> products. Star decahedron Cu nanoparticles<sup>123</sup> and branched CuO nanoparticles<sup>106</sup> are reported to achieve high faradaic efficiency of ethylene (C<sub>2</sub>H<sub>4</sub>) up to 52% and 70% at −1.0 V *vs.* RHE, respectively.

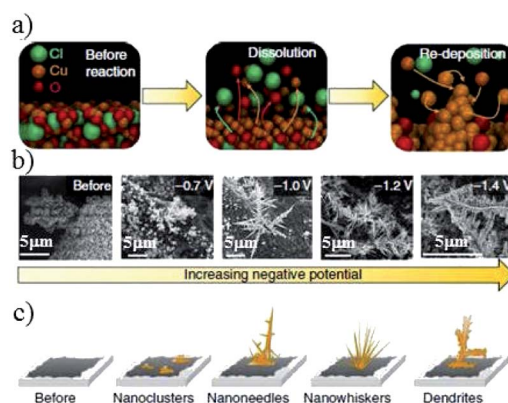


Fig. 9 (a) Schematic of the electrogrowth process of Cu from Cu<sub>2</sub>(-OH)<sub>3</sub>Cl. (b) Corresponding SEM images and (c) structure evolution of the key structural features after applying various potentials for at least 1 h in 0.1 M KHCO<sub>3</sub>. Reproduced from ref. 82 with permission from Springer Nature, 2018.





**Morphology evolution.** The influence of other morphologies on CO<sub>2</sub> reduction activity may be caused by many aspects. Although the enhancement effects and mechanisms of certain products are different for different morphologies, morphologies with more edges, corners or sharp tips seem to promote C<sub>2</sub> and even C<sub>3</sub> products. B. R. Cuenya and co-workers<sup>124</sup> electro-deposited prism-shaped Cu catalysts which exhibited higher C<sub>2</sub>H<sub>4</sub> current density than planar Cu foil. A total FE of ~73% for C<sub>2</sub> and C<sub>3</sub> products (~45% C<sub>2</sub>H<sub>4</sub>, 22% C<sub>2</sub>H<sub>5</sub>OH, 9% C<sub>3</sub>H<sub>7</sub>OH) at -1.0 V vs. RHE was obtained. They attributed the enhanced selectivity to the increased local pH and high abundance of defect sites on the roughed prism Cu surface. Cu pillar structure<sup>125</sup> achieved much higher HCOO<sup>-</sup> selectivity than planar Cu foil at -0.5 V vs. RHE (0.1 M KHCO<sub>3</sub>). Through electro-redeposition, dissolution and redeposition of Cu from Cu<sub>2</sub>(-OH)<sub>3</sub>Cl sol-gel, E. H. Sargent and co-workers<sup>82</sup> prepared Cu nanoneedles with sharp tips (Fig. 9). These Cu nanoneedles with sharp tips could produce high local electric fields that concentrate electrolyte cations and CO<sub>2</sub> molecules at the catalyst surface, resulting in a high partial C<sub>2</sub>H<sub>4</sub> current density (160 mA cm<sup>-2</sup> at -1.0 V vs. RHE) and C<sub>2</sub>H<sub>4</sub>/CH<sub>4</sub> ratio of up to 200 (flow cell). The effect of sharp tips was also explained from a kinetic point of view instead of a reaction barrier.<sup>126</sup> However, enhanced C<sub>1</sub> products were observed instead of C<sub>2</sub> products. N. F. Zheng and co-workers<sup>99</sup> reported a simple strategy to prepare ultrathin Cu/Ni(OH)<sub>2</sub> nanosheets with atomically thick ultra-stable Cu nanosheets in the presence of sodium formate (HCOONa), which achieved 92% CO at -0.5 V vs. RHE. The presence of surface formate inhibited the oxidation of Cu(0) and the hybrid structure probably had an effect on the promoted CO production. Hybrid structure-enhanced C<sub>1</sub> product formation has been observed by other groups.<sup>127,128</sup>

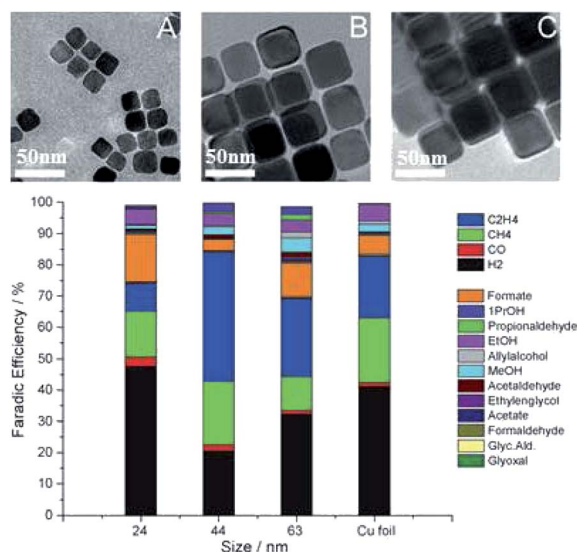


Fig. 10 TEM images of Cu cubes with an average edge length of 24 nm (A), 44 nm (B), 63 nm (C), and corresponding faradaic efficiency after subtracting the substrate signals. Experimental conditions: 0.1 M KHCO<sub>3</sub>, -1.1 V vs. RHE, 5 sccm CO<sub>2</sub>. Reproduced from ref. 129 with permission from Wiley, 2016.

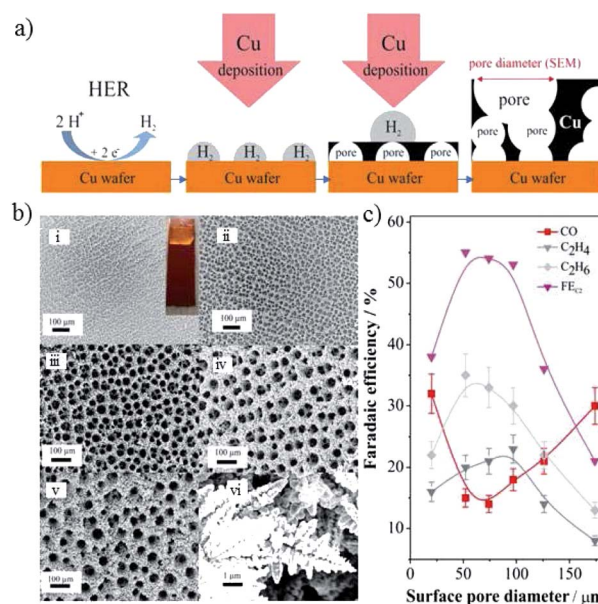


Fig. 11 (a) Schematic representation of the key aspects of Cu electrodeposition using H<sub>2</sub> as a template. (b) SEM images of Cu foams with different pore sizes on Cu substrate, electrodeposited for different times. (c) The faradaic efficiency of CO<sub>2</sub> reduction products for Cu foam with various pore sizes (experimental conditions: 0.5 M NaHCO<sub>3</sub>, -0.8 V vs. RHE). Reproduced from ref. 131 for (a) and (c), and ref. 88 for (b) with permission from the American Chemical Society, 2014 and 2016.

Similar trends in the role of morphology are observed for nanocube structures in powder systems, especially for C<sub>2</sub>H<sub>4</sub> production. R. Buonsanti and co-workers<sup>129</sup> fabricated different sizes of Cu nanocrystal spheres (7.5 nm and 27 nm) and Cu nanocrystal cubes (24 nm, 44 nm, and 63 nm). There was a monotonic size-dependent trend for both shapes – the smaller, the more active. Cube-shaped copper nanocrystals showed better performance than spheres. The overall CO<sub>2</sub> reduction activity changed from 50% to 80% and 63% for 24 nm, 44 nm, and 63 nm, respectively, and the highest faradaic efficiency of C<sub>2</sub>H<sub>4</sub> was 41% for 44 nm nanocubes at -1.1 V vs. RHE (Fig. 10). Edges and Cu(100) were responsible for maximizing C<sub>2</sub>H<sub>4</sub> selectivity. However, edges were also reported to promote CH<sub>4</sub> selectivity in nanowire structures. P. D. Yang and co-workers<sup>130</sup> prepared ultrathin (~20 nm) 5-fold twinned Cu nanowire on carbon black/glassy carbon plates. The catalyst could achieve 55% CH<sub>4</sub> at -1.25 V vs. RHE with <5% other CO<sub>2</sub> reduction products, likely due to the high density of edge sites. With the evolving morphology, CH<sub>4</sub> decreased and C<sub>2</sub>H<sub>4</sub> increased. Wrapping Cu nanowires with graphene oxide could prevent morphology changes and in turn prevent the decrease of CH<sub>4</sub> selectivity.

**3D structure.** The importance of the influence of three-dimensional (3D) structures on local pH, retention time of intermediates, gas permeability or liquid diffusion has been demonstrated by many researchers. G. Mul, M. T. Koper and co-workers<sup>31</sup> designed a 3D porous hollow fibre Cu electrode, and the rate of formation of CO was one order of magnitude larger



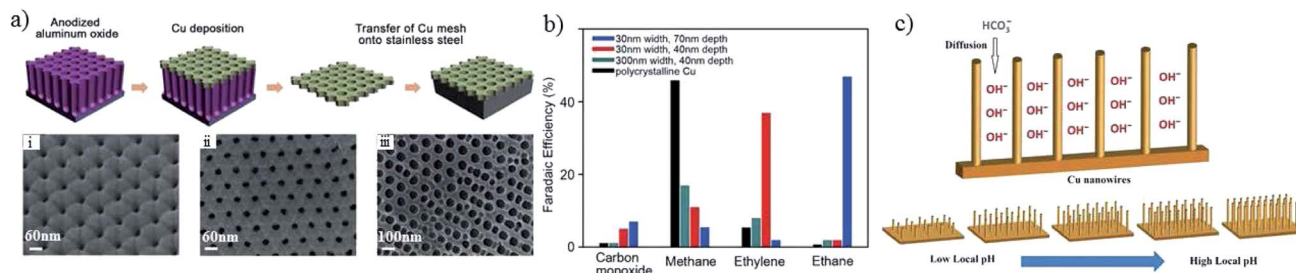


Fig. 12 (a) Scheme of Cu mesopore electrode preparation and corresponding SEM images; (i–iii) are 30 nm/40 nm, 30 nm/70 nm and 300 nm/40 nm width/depth, respectively. (b) The faradaic efficiencies of  $\text{CO}_2$  reduction products for the prepared Cu mesopores. Experimental conditions: 0.1 M  $\text{KHCO}_3$ ,  $-1.3$  V vs. RHE. (c) Schematic illustration of the diffusion of electrolytes into Cu nanowire arrays. Reproduced from ref. 133 for (a) and (b), and ref. 134 for (c) with permission from Wiley, 2016.

than for nanocrystalline Cu. Using hydrogen bubbles as a template, G. T. R. Palmore and co-workers<sup>88</sup> fabricated Cu nanofoams with connected pores of 20–50  $\mu\text{m}$  (Fig. 11b). Compared with an electropolished Cu electrode, they observed increased selectivity for  $\text{HCOOH}$ , decreased selectivity for  $\text{CO}$ ,  $\text{CH}_4$  and  $\text{C}_2\text{H}_4$ , and novel production of  $\text{C}_2\text{H}_6$  and  $\text{C}_3\text{H}_6$ . A maximum of 37%  $\text{HCOOH}$  was obtained at  $-0.9$  V vs. RHE (0.1 M  $\text{KHCO}_3$ ). They attributed these differences to the high surface roughness, hierarchical porosity, and confinement of reactive species. For the 3D nanoporous structure, the authors also showed that the inner surface area of the nanopores only becomes accessible above a critical electrolyte concentration of 0.5 M  $\text{KHCO}_3$  due to the overlapping electrical double layer (EDL). In another study, P. Broekmann and co-workers<sup>131</sup> prepared oxide-derived Cu nanofoams. The faradaic efficiency of  $\text{C}_2$  ( $\text{C}_2\text{H}_4$  and  $\text{C}_2\text{H}_6$ ) could reach 55% at  $-0.8$  V vs. RHE (0.5 M  $\text{NaHCO}_3$ ). Compared with the copper foam prepared by the Palmore group, there was a significant difference in the production distribution, which may be caused by the formation of  $\text{Cu}_2\text{O}$  and different pore sizes.  $\text{C}_2$  reached a maximum value for the surface pore size ranging from 50 to 100  $\mu\text{m}$ , while it decreased significantly below 50  $\mu\text{m}$  (Fig. 11c). The Broekmann group<sup>132</sup> also found more efficient trapping of reaction intermediates (e.g.  $\text{C}_2\text{H}_4$ ) in the presence of  $\mu\text{m}$ -sized pores within

the Cu foam on a 3D skeleton structure, favoring fully reduced  $\text{C}_2$  products. Using a similar preparation method to the Palmore and Broekmann groups,<sup>88,131</sup> E. H. Sargent, D. Sinton and co-workers<sup>79</sup> prepared a Cu nanofoam with pore sizes in the range of microns and then oxidized it in a mixed solution of 60 mM  $\text{HCl}$  and 60 mM  $\text{H}_2\text{O}_2$ . They again proved that higher surface roughness and porosity favored  $\text{C}_2\text{H}_4$  over  $\text{CH}_4$  (0.1 M  $\text{KHCO}_3$ , 20 sccm  $\text{CO}_2$ ).

In addition to pore sizes on the micron scale, nano-porous structures could also change the local pH and retention time of key intermediates<sup>133,135</sup> and, in turn, the product selectivity. Using a sputtering method on anodized aluminium oxide, as shown in Fig. 12a, the pore widths and depths of the Cu mesopore electrode could be precisely controlled. Compared with an electrode of 300 nm (width)/40 nm (depth),  $\text{C}_2\text{H}_4$  formation was enhanced from 8% to 38% when the pore width was narrowed to 30 nm, whereas the major  $\text{C}_2$  product changed to  $\text{C}_2\text{H}_6$  with a faradaic efficiency of 46% when the depth was increased to 70 nm at  $-1.3$  V vs. RHE (Fig. 12b). A pH change with 3D morphology was also reported by other groups. Using Cu foil with a mixed solution of  $(\text{NH}_3)_2\text{S}_2\text{O}_8$  and  $\text{NaOH}$  for different times, W. A. Smith and co-workers<sup>134,136</sup> obtained  $\text{Cu}(\text{OH})_2$  nanowires with various lengths and densities. The nanowires with high lengths and densities had an influence on the diffusion of  $\text{HCO}_3^-$ , leading to a high local pH, since  $\text{HCO}_3^-$  can neutralize  $\text{OH}^-$  ( $\text{HCO}_3^- + \text{OH}^- \rightarrow \text{CO}_3^{2-} + \text{H}_2\text{O}$ ), as shown in Fig. 12c. With higher lengths ( $\geq 2.4 \pm 0.56$   $\mu\text{m}$ ),  $n\text{-C}_3\text{H}_7\text{OH}$  was detected along with  $\text{CO}$ ,  $\text{HCOOH}$  and  $\text{C}_2\text{H}_4$ . For even higher lengths ( $\geq 7.3 \pm 1.3$   $\mu\text{m}$ ),  $\text{C}_2\text{H}_6$  and  $\text{C}_2\text{H}_5\text{OH}$  could be formed. In summary, high lengths or depths of 3D nanostructures favor higher hydrocarbon formations.

**Crystal facets.** The crystal facet dependence of  $\text{CO}_2$  reduction for Cu foil and Cu single crystals has been widely explored by experimental and theoretical methods,<sup>137</sup> especially for (111) and (100).<sup>138</sup> On a single-crystal copper electrode, M. T. Koper and co-workers<sup>26,66,139,140</sup> observed that one pathway for the formation of  $\text{CH}_4$  preferentially occurs on (111) facets, while the other pathway leads to  $\text{C}_2\text{H}_4$  formation on (100) facets.<sup>66</sup> The Koper group also distinguished the reactivity of (100) terraces versus (100) steps, where selective reduction of  $\text{CO}$  to  $\text{C}_2\text{H}_4$  at low overpotentials occurs on terrace sites.<sup>139</sup> The theoretical calculation stated that the coupling of two  $\text{CO}$  molecules

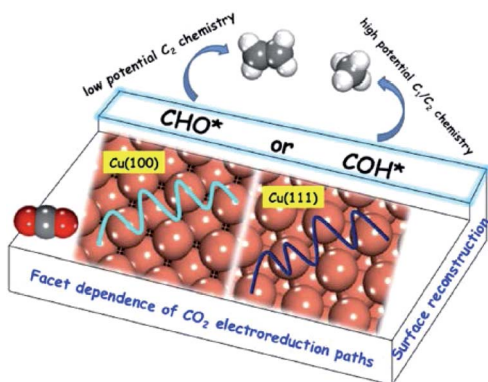


Fig. 13 Schematic illustration of reaction pathways on Cu(100) and (111) single crystals. Reproduced from ref. 138 with permission from the American Chemical Society, 2016.



mediated by electron transfer to form a  $^*C_2O_2$  dimer is a rate-determining step involved on Cu(100) for  $C_2$  ( $C_2H_4$  and  $C_2H_5OH$ ) formation.<sup>140</sup> Experiments on CO and  $CO_2$  reduction in electrolytes with various pH values also showed a pH-dependent pathway for  $CH_4$  mainly on Cu(111) and a pH-independent pathway for  $C_2H_4$  on Cu(100).<sup>26</sup> Results from other groups suggest that Cu(100) favors  $CHO^*$  intermediates and follows  $C_2H_4$  formation at relatively low overpotentials ( $-0.4$  to  $-0.6$  V vs. RHE), while Cu(111) favors  $COH^*$  intermediates and  $CH_4/C_2H_4$  formation at high overpotentials ( $<-0.8$  V vs. RHE), as shown in Fig. 13.<sup>138</sup>

B. S. Yeo and co-workers<sup>141</sup> studied  $Cu_2O$  (hydrothermally prepared)-derived Cu and Cu single-crystal surfaces. Of the three single-crystal surfaces (100), (111) and (110), Cu(100) exhibited the lowest energy barrier for the dimerization of  $CO^*$ . A. Nilsson and co-workers<sup>157</sup> investigated single crystal copper (100), (111), and (211) for comparison with Cu nanocubes. The (100) surface was the most comparable to the Cu nanocube surface in terms of  $C_2H_4$  production, whereas  $CH_4$  was not suppressed. One possibility is that it has the ideal terrace length or active sites for  $C_2H_4$  formation. K. Chan, H. T. Wang and co-workers<sup>59</sup> galvanostatically cycled Cu foil in  $Cu(NO_3)_2$  to obtain a  $Cu_2O$  nanocube layer with smooth (100) facets on the surface. They also suggested that Cu(100) and stepped (211) facets favored  $C_{2+}$  products over Cu(111). From the present results, Cu(100) crystal facets favor  $C_{2+}$  products compared with other facets for most reported systems.

As stated above, understanding the effects of Cu morphology on the selectivity is highly complex since there is a combined effect of properties, such as low-coordinated sites, catalyst density or dispersion,  $CO_2$  flux and electrical double layers in

the electrolyte, on the activity of  $CO_2$  electrochemical reduction. Although there is wide variation in the activity trends for Cu with various morphologies, the selectivity for possible products may be adjusted by tuning the particle size and interparticle spacing/particle density of Cu nanoparticles/nanocubes, tuning the pore size and depth/length of 3D structures, or tuning the energy facets of Cu crystals. In addition, attention should be paid to morphology evolution during the electrochemical  $CO_2$  reduction process.

## 4.2 Oxide-derived Cu electrocatalysts

Recently, oxide-derived Cu has drawn much attention in electrocatalytic  $CO_2$  reduction. Various oxide-derived Cu electrocatalysts have been designed and the mechanisms involved have been discussed widely. Some groups<sup>68–71,142,143</sup> suggest that grain boundaries are the active sites. Some groups<sup>80,144,145</sup> believe that low-coordinated atoms act as active sites. There are also many groups<sup>85,114,146–148</sup> which believe that the active phase is metallic  $Cu^0$  since there is a significant driving force for  $Cu_2O$  reduction under  $CO_2$  reduction conditions. Many groups<sup>82,95,149,150</sup> proved that the  $Cu^+$  site is key for enhanced activity and remained on the catalyst surface during the reaction. Some groups<sup>96,151,152</sup> found that sub-surface oxygen stabilized in reduced oxide-derived Cu plays an important role and there is synergy between surface  $Cu^+$  and surface  $Cu^0$  sub-oxide species.

Although the true active site is still under debate, oxide-derived Cu has shown excellent performance in decreasing the potential required and enhancing selectivity for specific products. Most recent reports also confirmed that two ( $Cu^{\delta+}$  and  $Cu^0$ ) were better than one.<sup>100,154</sup> In this section, we will discuss

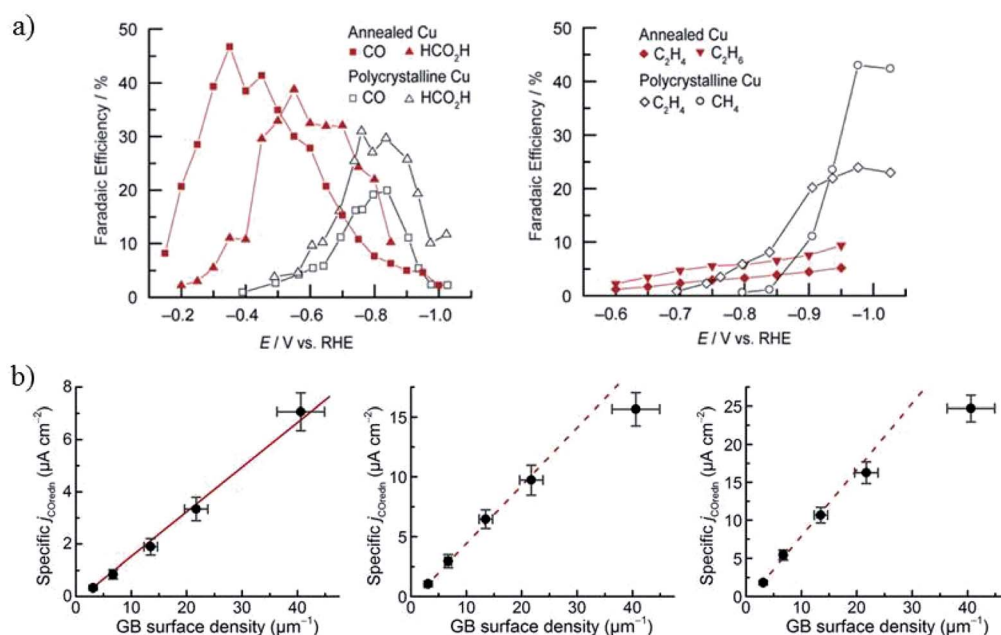


Fig. 14 (a) The faradaic efficiency of  $CO_2$  reduction products for annealed Cu and polycrystalline Cu foil. 0.1 M  $NaHCO_3$ , 5 sccm  $CO_2$ . (b) The specific current density of CO reduction versus the grain boundary density at  $-0.3$  V,  $-0.4$  V and  $-0.5$  V, respectively. Reproduced from ref. 69 for (a) and ref. 71 for (b) with permission from the American Chemical Society, 2016.





oxide-derived Cu in detail based on the fabrication process, including annealed/oxide-derived Cu, electrodeposited/oxide-derived Cu,  $\text{Cl}^-$ /oxide-derived Cu, plasma/oxide-derived Cu, and *in situ*/oxide-derived Cu. Since the wide variation in experimental conditions results in various results for similar materials, detailed experimental conditions are included for different groups.

**Annealed/oxide-derived Cu.** Annealing is a simple and effective strategy to enhance the activity of Cu. During this process, the annealing temperature and the following redox process all have an influence on the  $\text{CO}_2$  reduction activity. M. W. Kanan and co-workers<sup>69</sup> annealed Cu foil at different temperatures in air, forming  $\text{Cu}_2\text{O}$  layers with different thicknesses. Thick  $\text{Cu}_2\text{O}$  layers formed at  $500^\circ\text{C}$  ( $\geq 3\ \mu\text{m}$ ) exhibited higher selectivity and lower overpotential to CO (45% at  $-0.3$  to  $-0.5\ \text{V}$  vs. RHE) and  $\text{HCOO}^-$  (33% at  $-0.45$  to  $-0.65\ \text{V}$  vs. RHE) compared with the Cu foil counterpart (Fig. 14a). Later, using oxide-derived Cu (electrochemical reduction and thermal reduction with  $\text{H}_2$ ), they<sup>68</sup> investigated CO electroreduction to liquid fuels in CO-saturated  $0.1\ \text{M KOH}$  ( $\text{pH} = 13$ ). Engineering the grain boundaries by altering the redox process could tune the product distribution. 57% carbon oxygenated species ( $\text{C}_2\text{H}_5\text{OH}$ ,  $\text{C}_2\text{H}_5\text{COO}^-$  and  $n\text{-C}_3\text{H}_7\text{OH}$ ) were obtained at potentials ranging from  $-0.25\ \text{V}$  to  $-0.5\ \text{V}$  vs. RHE. Temperature-programmed desorption (TPD) experiments<sup>70</sup> showed that the active sites for CO reduction on oxide-derived Cu surfaces were strong CO binding sites supported by grain boundaries. The Kanan group<sup>71</sup> also prepared electrodes of Cu nanoparticles on carbon nanotubes (Cu/CNT) with different average grain boundaries *via* e-beam evaporation and subsequent annealing. The CO reduction activity was directly correlated to the density of grain boundaries in Cu nanoparticles, exhibiting a linear relationship at potentials ranging from  $-0.3\ \text{V}$  to  $-0.5\ \text{V}$  vs. RHE (Fig. 14b). A maximum faradaic efficiency of  $>70\%$   $\text{C}_2\text{H}_5\text{OH}$  and  $\text{C}_2\text{H}_5\text{COO}^-$  was obtained at  $-0.3\ \text{V}$  vs. RHE. I. E. L. Stephens, I. Chorkendorff and co-workers<sup>101</sup> investigated CO electroreduction on oxide-derived Cu prepared by the Kanan group. They showed that  $\text{CH}_3\text{CHO}$  was a key intermediate in the electroreduction of CO to  $\text{C}_2\text{H}_5\text{OH}$  and formed at a low steady-state concentration.

Higher temperature annealing forms both  $\text{Cu}_2\text{O}$  and CuO nanowires and the corresponding derived Cu also exhibits superior performance for  $\text{CO}_2$  reduction. C. Wang and co-workers<sup>80</sup> annealed Cu gauze in air at  $600^\circ\text{C}$  to get CuO nanowires (with  $\text{Cu}_2\text{O}$  present inside the nanowires) with a diameter of  $50\text{--}100\ \text{nm}$  and length of  $10\text{--}50\ \mu\text{m}$ . Then they obtained high density Cu nanowires by electrochemical reduction (ECR) or forming gas reduction (FGR). The Cu nanowires obtained *via* the ECR method exhibited a higher surface roughness and a thin surface layer of  $\text{Cu}_2\text{O}$  nanocrystals less than  $10\ \text{nm}$ , while FGR led to larger Cu crystal segments ( $>100\ \text{nm}$  size) without  $\text{Cu}_2\text{O}$  present on the surface. At low overpotentials ( $-0.3\ \text{V}$  to  $-0.5\ \text{V}$  vs. RHE), the total faradaic efficiency of CO and  $\text{HCOOH}$  was as high as  $70\text{--}80\%$  for ECR nanowires, whereas  $\text{H}_2$  was the dominant product for Cu gauze and FGR nanowires ( $0.1\ \text{M KCHCO}_3$ ,  $20\ \text{scm CO}_2$ ). They ascribed the high activity to the high-density grain boundaries and low-coordinated surface

sites associated with the small crystalline features, as well as more open facets (*e.g.* (100) and (211)) on the surface. Later studies by C. Wang, T. Mueller and co-workers<sup>144,145</sup> further suggested that the high activity and selectivity of the ECR nanowires could be ascribed to the (110) surface, high-angle grain boundaries, or some closely related metastable surface feature. Pre-reduction of annealed Cu in different solutions led to different activities, as also reported by J. J. Zhang's group.<sup>155</sup> Reduction of annealed Cu in  $1\ \text{M NaOH}$  formed only a layer of nanofibers with  $30\text{--}100\ \text{nm}$  diameters, whereas in  $1\ \text{M H}_3\text{PO}_4$  the nanofibers were surrounded by kernels and achieved  $43\%$   $\text{HCOO}^-$ , which was much higher than for the pre-reduced annealed Cu in  $\text{NaOH}$  ( $1\% \text{HCOO}^-$ ) in  $0.5\ \text{M KHCO}_3$ .

Summarizing the above reports, the annealed/oxide-redox method could enhance the selectivity and lower the overpotential required for  $\text{HCOO}^-$  and CO during  $\text{CO}_2$  reduction, while promoting the selectivity of  $\text{C}_{2+}$  products during CO reduction.

With related mechanism studies on enhanced  $\text{HCOO}^-$  and CO formation, using ambient pressure X-ray photoelectron spectroscopy interpreted with quantum mechanical predictions of the structures and free energies, W. A. Goddard III, J. Yano, E. J. Crumlin and co-workers<sup>96</sup> showed that the presence of sub-oxide species below the Cu surface played a crucial role in the adsorption and activation of  $\text{CO}_2$  on annealed/oxide-derived Cu. This thin layer of sub-oxide was essential for converting chemisorbed  $\text{CO}_2$  in the presence of  $\text{H}_2\text{O}$  as the first step toward  $\text{CO}_2$  reduction products such as  $\text{HCOO}^-$  and CO. Quantum mechanical calculations and experimental results also showed that there was an optimized amount of subsurface oxide. More or none at all would destabilize the bent (chemisorbed)  $\text{CO}_2$ . (1) In the case of Cu(111) without subsurface oxide (Fig. 15a), the C atom of  $\text{CO}_2$  was chemically bonded to a  $\text{Cu}^0$ . One of the O atoms was stabilized by hydrogen bonding to  $\text{H}_2\text{O}_{\text{ad}}$  on another  $\text{Cu}^0$ . (2) When the subsurface oxide was increased to  $1/4\ \text{ML}$  (Fig. 15b), the C atom was chemically bonded to two surface  $\text{Cu}^0$ . One O atom was chemically bonded to one  $\text{Cu}^0$ , and the other O atom was stabilized by the  $\text{Cu}^+$  pulled up by  $\text{H}_2\text{O}_{\text{ad}}$ . (3) When the subsurface oxide was increased to  $1/2\ \text{ML}$  (Fig. 15c), the C atom was chemically bonded to a  $\text{Cu}^+$  that shares one O atom stabilized by hydrogen bonding to  $\text{H}_2\text{O}_{\text{ad}}$  on another  $\text{Cu}^+$ . Later they<sup>153</sup> found that only surface  $\text{Cu}^+$  itself could not improve the performance of  $\text{CO}_2$  reduction, and proposed Cu metal embedded in an oxidized matrix model as a partially oxidized Cu surface, where the synergy between the surface  $\text{Cu}^+$  and surface  $\text{Cu}^0$  was responsible for  $\text{CO}_2$  activation.

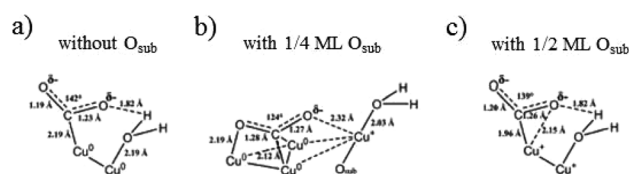


Fig. 15 Predicted structures for chemisorbed- $\text{CO}_2$  with  $\text{H}_2\text{O}$  on Cu(111) with different levels of subsurface oxide  $\text{O}_{\text{sub}}$ : (a)  $0\ \text{ML}$ , (b)  $1/4\ \text{ML}$  and (c)  $1/2\ \text{ML O}_{\text{sub}}$ . Reproduced from ref. 96.





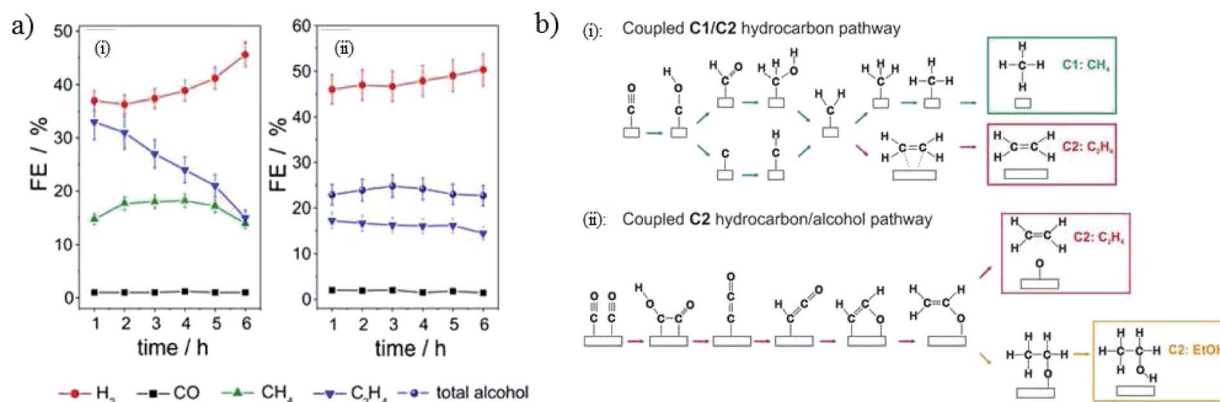


Fig. 16 (a) The faradaic efficiency of CO<sub>2</sub> reduction products for electrodeposited Cu(I) and annealed Cu(II). (b) Proposed schemes for electrodeposited and annealed samples. Experimental conditions:  $-1.1$  V vs. RHE,  $0.5$  M KHCO<sub>3</sub>. Reproduced from ref. 156 with permission from the American Chemical Society, 2017.

**Electrodeposited/oxide-derived Cu.** In contrast to the annealed-redox process above, the electrodeposited/annealed and electrodeposited Cu<sub>2</sub>O film could also promote C<sub>2</sub> products besides HCOO<sup>−</sup> or CO in CO<sub>2</sub> reduction compared with pure Cu. P. Broekmann and co-workers<sup>132</sup> compared two types of oxide-derived catalyst, annealed skeleton (300 °C, 12 h) and electrodeposited Cu nanofoam on 3D Cu skeleton. Both the annealed and electrodeposited skeleton catalysts showed preferential (100) texturing and profound activities toward C<sub>2</sub> product formation (C<sub>2</sub>H<sub>4</sub> and C<sub>2</sub>H<sub>6</sub>) in  $0.5$  M NaHCO<sub>3</sub>. Later, they<sup>156</sup> electrodeposited dendritic Cu on Cu mesh *via* the mass control of Cu(II) ions, followed by thermal annealing at 300 °C in air. Electrodeposited dendritic Cu showed high HCOO<sup>−</sup> and C<sub>2</sub>H<sub>4</sub> production, while the electrodeposited/annealed sample directed product selectivity toward C<sub>2</sub> and C<sub>3</sub> alcohols (detailed data given in Table 1) and high resistance against degradation (Fig. 16a). An identical location SEM study showed that Cu nanoparticles and nm-sized cavities and cracks on large dendritic structures were present for the annealed sample. They assigned the difference in stability to the change in reaction mechanism; namely, the electrodeposited sample relied on a coupled C<sub>1</sub>/C<sub>2</sub> pathway (catalyst poisoning/blocking effect predominantly caused by C<sub>1</sub> hydrocarbon pathway), while the annealed sample relied on a coupled C<sub>2</sub> hydrocarbon/alcohol pathway (Fig. 16b).

There is a dependence of CO<sub>2</sub> activity on film thickness for electrodeposited Cu<sub>2</sub>O film. J. Baltrusaitis, G. Mul and co-workers<sup>72</sup> electrodeposited Cu<sub>2</sub>O film on a Cu plate. A C<sub>2</sub>H<sub>4</sub>/CH<sub>4</sub> ratio of  $\sim 8$ – $12$  was observed for thin film at  $-1.1$  V vs. RHE, with a larger amount of CH<sub>4</sub> for thicker film ( $0.1$  M KHCO<sub>3</sub>,  $5$  sccm CO<sub>2</sub>). B. S. Yeo and co-workers<sup>81</sup> electrodeposited Cu<sub>2</sub>O film with different film thicknesses on Cu discs. A maximum of 34–39% C<sub>2</sub>H<sub>4</sub> with a ratio of C<sub>2</sub>H<sub>4</sub>/CH<sub>4</sub> up to 100, and 9–16% C<sub>2</sub>H<sub>5</sub>OH was obtained at  $-1.0$  V vs. RHE, as shown in Fig. 17a. Then they<sup>146</sup> prepared Cu<sub>2</sub>O- and CuO-derived Cu with different thicknesses *via* a hydrothermal method (1.3 and 11.5  $\mu$ m). In contrast to other works proposing the protonation of C<sub>2</sub>H<sub>4</sub>, they showed that C<sub>2</sub>H<sub>6</sub> and C<sub>2</sub>H<sub>5</sub>OH were likely to form *via* the

dimerization of  $-\text{CH}_3$  intermediates on thick oxide-derived Cu (Fig. 17b). They observed that Cu<sub>2</sub>O was rapidly reduced to metallic Cu during CO<sub>2</sub> reduction by using *in situ* Raman spectroscopy. The surface reoxidized in tens of seconds after the cathodic potential was removed. This is in contrast to the Lee group's<sup>150</sup> work on electrodeposited Cu<sub>2</sub>O/GDE, where they found that Cu<sub>2</sub>O was only partially reduced on the basis of *ex situ* XRD and Auger electron spectroscopy. Later again, the Yeo group only observed signals belonging to CO adsorbed on Cu metallic sites rather than oxide sites for electrodeposited Cu<sub>x</sub>Zn.<sup>84</sup>

**Cl<sup>−</sup>/oxide-derived Cu.** Although the formation mechanism may still be unclear, cycling a Cu precursor in the presence of Cl<sup>−</sup> will lead to Cu nanocubes, which will in turn favour C<sub>2</sub>H<sub>4</sub> production. A. Nilsson and co-workers<sup>157,158</sup> reported a simple *in situ* method to fabricate nanocube-covered Cu by its successive oxidative–reductive cycling in the presence of KCl. Using online electrochemical mass spectrometry (OLEMS), there was an earlier onset potential and relatively high selectivity for C<sub>2</sub>H<sub>4</sub> over CH<sub>4</sub> ( $0.1$  M KHCO<sub>3</sub>). The Yeo group<sup>159</sup> also observed an enhanced C<sub>2</sub>H<sub>4</sub>/CH<sub>4</sub> ratio with Cl<sup>−</sup>/oxide-derived Cu. The Nilsson group ascribed the enhanced C<sub>2</sub>H<sub>4</sub> formation to the large number of exposed (100) facets and the rise in the local pH for the roughened surface of Cu nanocubes. The Ager group and the

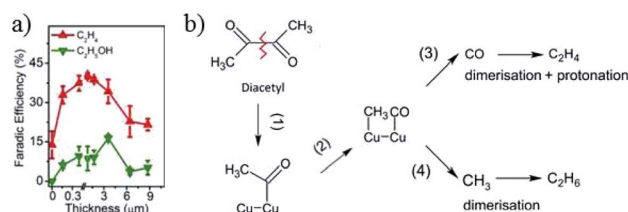


Fig. 17 (a) The faradaic efficiency of C<sub>2</sub>H<sub>4</sub> and C<sub>2</sub>H<sub>5</sub>OH versus the thickness of electrodeposited Cu<sub>2</sub>O. (b) Proposed mechanism for thick oxide-derived Cu and thin oxide-derived Cu, respectively. Experimental conditions:  $-1.0$  V vs. RHE,  $0.1$  M KHCO<sub>3</sub>,  $20$  sccm CO<sub>2</sub>. Reproduced from ref. 81 for (a) and ref. 146 for (b) with permission from the American Chemical Society, 2015 and 2017.



Bell group did more work to understand the effect of pH on product formation for  $\text{Cl}^-$ /oxide-derived Cu nanocubes. Using *in situ* X-ray absorption spectroscopy (XAS), A. Nilsson and co-workers<sup>147</sup> investigated the formation mechanism of the Cu nanocubes. Since no CuCl was observed in the Cu K-edge XAS spectra, they believed that the precursor for nanocube formation was  $\text{Cu}_2\text{O}$ , not CuCl as previously assumed (A. T. Bell and J. W. Ager's work is shown in Fig. 18a).  $\text{CuCO}_3/\text{Cu}(\text{OH})_2$  was also prepared *via* cycling in the absence of KCl. The results of OLEMS during  $\text{CO}_2$  reduction showed that there were no significant differences between  $\text{CuCO}_3/\text{Cu}(\text{OH})_2$ -derived Cu and  $\text{Cl}^-/\text{Cu}_2\text{O}$ -derived Cu. Therefore, they pointed out that the influence of the precursor oxidation state on the selectivity toward  $\text{C}_2\text{H}_4$  formation was not important. They also believed that the active species was metallic Cu, since no significant concentration of residual oxide was detected on the order of a few nanometers in the thin XAS model samples. Their further study<sup>151</sup> used *in situ* ambient pressure X-ray photoelectron spectroscopy (APXPS) and quasi-*in situ* electron energy loss spectra (EELS), which showed that there was a small amount of subsurface oxygen but no residual copper oxide. Combined with DFT simulations, they proposed that the interaction of subsurface oxygen with metal causes higher CO binding energy, resulting in higher CO coverage. Higher CO coverage kinetically favored C–C bond formation.

In contrast to the Nilsson group's study<sup>157</sup> and the Yeo group's study,<sup>159</sup> J. Lee and co-workers<sup>160</sup> observed the preferential formation of multicarbon fuels, especially  $n\text{-C}_3\text{H}_7\text{OH}$  (the first report over 10%  $\text{C}_3\text{--C}_4$  products, 0.1 M KCl), using *in situ* prepared  $\text{Cl}^-$ -induced bi-phasic  $\text{Cu}_2\text{O}$ –Cu. They also found that the catalyst exhibited relatively higher  $\text{Cu}^+$  coverage than oxide-derived Cu and the use of a KCl electrolyte could prolong the preservation of the  $\text{Cu}_2\text{O}$  phase compared to a  $\text{KHCO}_3$  electrolyte.

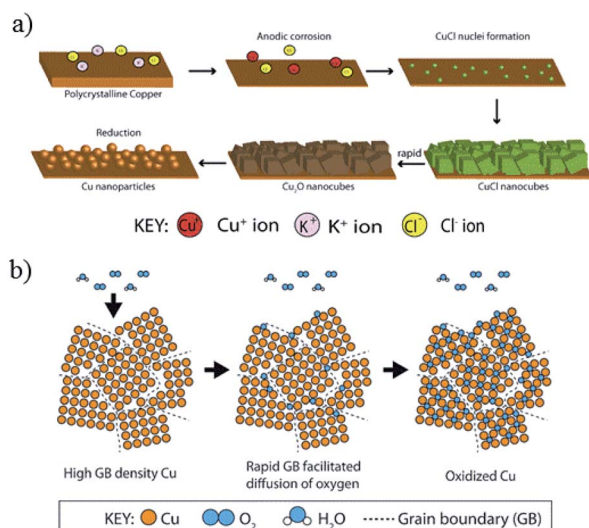


Fig. 18 (a) Proposed mechanism of Cu nanoparticle growth during electrochemical cycling in the presence of  $\text{Cl}^-$ . (b) Rapid oxidation of  $\text{Cl}^-$ /oxide-derived Cu with a high abundance of grain boundaries. Reproduced from ref. 142 for (a) and ref. 143 for (b) with permission from Wiley, 2016 and 2017.

A. T. Bell, J. W. Ager and co-workers<sup>142</sup> electrochemically cycled copper foil in the presence of halide anions KF, KCl, KBr, and KI. They observed an enhanced faradaic efficiency for  $\text{C}_2\text{H}_4$  and  $\text{C}_2\text{H}_5\text{OH}$  (excluding KF). Their observation of  $\text{C}_2\text{H}_5\text{OH}$  was in contrast to the Nilsson group and Yeo group studies. Without electrochemical cycling in halide anions, the product distribution was not significantly changed even with the addition of halide anions in electrolyte for  $\text{CO}_2$  reduction. *In situ* Raman spectroscopy and SEM showed that during the oxidation sweep, anodic corrosion formed a  $\text{Cu}_2\text{O}$  layer, which consisted of cubic crystals  $\sim 150$  nm. CuCl formed cubes when precipitated in the solution at  $\text{pH} > 4$ . In neutral and basic solutions with a low  $\text{Cl}^-$  concentration, CuCl could convert to  $\text{Cu}_2\text{O}$ . During the reduction sweep, irregular Cu nanoparticles (*ca.* 20 nm in diameter) with rounded edges were formed (Fig. 18a). They ascribed the enhancement in  $\text{C}_2\text{H}_4$  formation to a large number of (100) facets (similar to the Nilsson group) and the formation of grain boundaries and defects (similar to the Kanan group). Later they<sup>64</sup> also investigated four types of oxide-derived Cu electrocatalysts: “oxide-derived nanocrystalline Cu” developed by the Kanan group, “Cu nanowire arrays” developed by the Smith group, “electrodeposited  $\text{Cu}_2\text{O}$  films” developed by the Yeo group, and “electrochemical oxidation–reduction cycled Cu” developed by the Nilsson group. There was an optimal roughness factor for the oxide-derived layers to have a high local pH and maintain a high concentration of dissolved  $\text{CO}_2$ . More recently, J. W. Ager and co-workers<sup>143</sup> prepared  $^{18}\text{O}$ -enriched oxide-derived Cu by cycling Cu foil in the presence of KCl in  $\text{H}_2^{18}\text{O}$ . The selectivity of  $\text{C}_2$  and  $\text{C}_3$  products in 0.1 M  $\text{KHCO}_3$  was up to 60%. By analysis with *ex situ* secondary-ion mass spectrometry (SIMS), they found that  $<1\%$  of the original  $^{18}\text{O}$  content remained in the sample after the  $\text{CO}_2$  reduction reaction and believed that the grain boundary was more likely responsible for the high activity, as proposed by the Kanan group. Similarly to the Yeo group, they also observed the rapid re-oxidation of oxide-derived Cu with *in situ* Raman spectroscopy. They believed that this rapid re-oxidation was possibly due to the grain boundaries (Fig. 18b), since Cu film with fewer grain boundaries did not oxidize quickly.

E. H. Sargent and co-workers<sup>82</sup> applied constant potential in  $\text{CO}_2$ -saturated 0.1 M  $\text{KHCO}_3$  to reduce  $\text{Cu}_2(\text{OH})_3\text{Cl}$  precursor on carbon paper. This dissolution and electro-redeposition process could form  $\text{Cu}_2\text{O}$  nanoneedles, which exhibited excellent activity for  $\text{C}_2\text{H}_4$  formation (partial current density 160  $\text{mA cm}^{-2}$ ) with a ratio of  $\text{C}_2\text{H}_4/\text{CH}_4$  of up to 200 at  $-1.0$  V vs. RHE (20 scem  $\text{CO}_2$ ). For the first time, they used *in situ* Cu L-edge XAS to demonstrate that the  $\text{Cu}^+$  surface species could direct  $\text{C}_{2+}$  product selectivity. The process of  $\text{Cu}^{2+}$  to  $\text{Cu}^+$  was quick (within 5 min), while  $\text{Cu}^+$  to  $\text{Cu}^0$  was much slower, and 23%  $\text{Cu}^+$  surface species still remained after 1 h electrolysis at  $-1.2$  V vs. RHE.

In summary,  $\text{Cl}^-$ /oxide-derived Cu shows excellent activity for  $\text{C}_2$  and even  $\text{C}_3\text{--C}_4$  product formation, regardless of whether it is caused by the morphology evolution to nanocubes or the presence of  $\text{Cu}^+$ .

**Plasma/oxide-derived Cu.** Plasma-induced CuO and  $\text{Cu}_2\text{O}$  as a precursor of Cu-based electrocatalysts for efficient  $\text{CO}_2$  reduction was recently reported by B. R. Cuenya and co-



workers.<sup>95</sup> The plasma treatment could suppress  $\text{CH}_4$  formation while enhancing the formation of  $\text{CO}$ ,  $\text{HCOO}^-$  and  $\text{C}_2\text{H}_4$ . The onset potential towards  $\text{CO}$  and  $\text{HCOO}^-$  was shifted to lower overpotentials, similar to the result observed by the Kanan group. However, the presence of strongly binding defect sites such as grain boundaries with intermediates proposed by the Kanan group could explain the early onset potential for  $\text{CO}_2$  reduction, but could not explain the suppression of  $\text{C}_2\text{H}_4$  due to the  $\text{H}_2$  plasma treatment following  $\text{O}_2$  plasma treatment (Fig. 19a). Therefore, using a combination of characterization techniques, including operando X-ray absorption fine-structure spectroscopy (XAFS) and scanning transmission electron microscopy (STEM) equipped with energy dispersive X-ray spectroscopy (EDS), the authors found that the oxides in the surface layer were resistant to reduction and  $\text{Cu}^+$  species remained on the surface during the reaction. By controlling experiments with the same surface roughness ( $\text{O}_2$  plasma plus  $\text{H}_2$  and  $\text{O}_2$  plasma-treated Cu foils), they demonstrated that the roughness of oxide-derived Cu catalysts played only a partial role in determining the catalytic performance, while the presence of  $\text{Cu}^+$  was key for lowering the onset potential and enhancing  $\text{C}_2\text{H}_4$  selectivity. Later, the Cuenya group<sup>149</sup> used the same method to activate Cu nanocube catalysts obtained by

electrochemical cycling of Cu foil in 0.1 M KCl.  $\sim 73\%$   $\text{C}_2$  and  $\text{C}_3$  products were achieved on  $\text{Cl}^-$ -induced Cu nanocubes and  $\text{O}_2$  plasma-treated samples. High  $\text{C}_2\text{H}_5\text{OH}$  ( $\sim 22\%$ ) and  $n\text{-C}_3\text{H}_7\text{OH}$  ( $\sim 9\%$ ) were also obtained for the  $\text{O}_2$  plasma-treated sample at  $-1.0$  V vs. RHE. In their former work,<sup>95</sup> they observed that  $\text{Cu}^+$  is the key. Through controlled experiments in this work (Fig. 19b), they believed that the oxygen content (oxygen ions associated with  $\text{Cu}^+$  species) played a more important role in  $\text{C}_2\text{H}_4$  formation than  $\text{Cu}(100)$  facets.

**In situ/oxide-derived Cu.** *In situ* formation of oxide during  $\text{CO}_2$  electrolysis is a promising method to activate Cu electrocatalysts, although the promoted products are uncertain. A. Engelbrecht and co-workers<sup>161</sup> oxidized Cu *in situ* by using a  $\text{CO}_2/\text{O}_2$  gas mixture instead of pure  $\text{CO}_2$  gas and found that the formation of  $\text{CH}_4$  was largely suppressed, while  $\text{C}_2\text{H}_4$  was favored (0.1 M  $\text{KHCO}_3$ , 100 sccm). J. M. Spurgeon and co-workers<sup>83</sup> used a pulsed-bias technique for  $\text{CO}_2$  reduction on Cu foil. Compared with the conventional potentiostatic technique, there was a major shift in the selectivity (Fig. 20). The syngas  $\text{H}_2$  :  $\text{CO}$  ratio ranged from  $\sim 32 : 1$  to  $9 : 16$  for pulse times between 10 ms and 80 ms, respectively (0.1 M  $\text{KHCO}_3$ , 20 sccm). J. Y. Lee and co-workers<sup>162</sup> also indicated that  $\text{Cu}_2\text{O}$  formed under the anodic cycle in the pulsed electroreduction of  $\text{CO}_2$  and this process also prevented the poisoning of carbon on the Cu surface. Using pulsed voltammetry, P. Rodriguez and co-workers<sup>163</sup> observed that oxygenated products associated to the coverage of OH species on single crystal  $\text{Cu}(100)$  and  $\text{Cu}(111)$ . In contrast to Spurgeon and co-workers' work,<sup>83</sup> however, the selectivity trend shifted to  $\text{CH}_4$  and  $\text{C}_2\text{H}_4$ .

Early last year, however, I. Chorkendorff, I. E. L. Stephens and co-workers<sup>164</sup> investigated CO electroreduction on polycrystalline Cu foil in 0.1 M KOH at low overpotentials from  $-0.4$  to  $-0.6$  V vs. RHE. Compared with oxide-derived nanostructured Cu in the literature, the polycrystalline Cu foil exhibited higher selectivity for  $\text{C}_2$  and  $\text{C}_3$  aldehydes and ethylene. This indicated that future studies should focus on the intrinsic activity of Cu.

In summary, for oxide-derived Cu, various methods have been developed for the preparation of a Cu-oxide precursor ( $\text{Cu}^{2+}$ ,  $\text{Cu}^+$ ) and for its subsequent redox process (*in situ* and *ex situ*, electrochemical and  $\text{H}_2$  reduction). As stated at the beginning of this part, the true active site of Cu-based electrocatalysts fabricated from oxidation–reduction processes is still under discussion. Using Cu-based electrocatalysts with

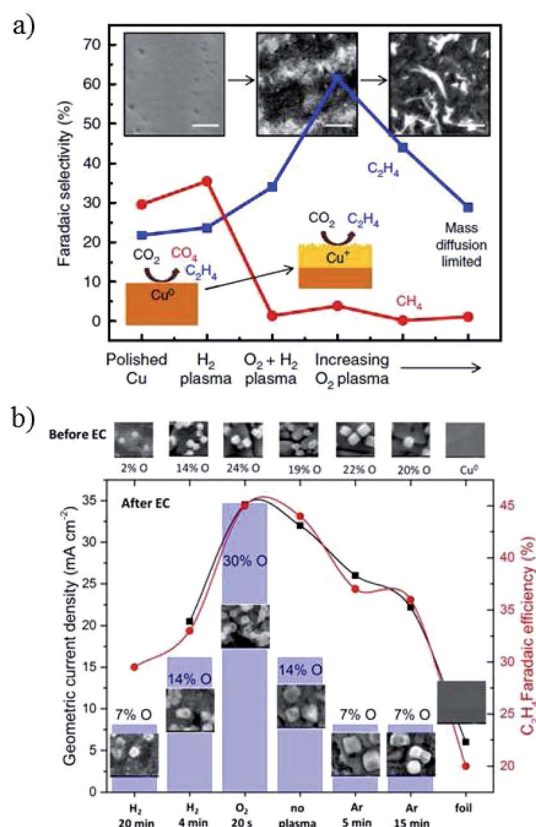


Fig. 19 (a) The faradaic efficiency of hydrocarbon products for plasma-treated Cu foil. (b) Current density and  $\text{C}_2\text{H}_4$  faradaic efficiency for Cu nanocubes with plasma treatment. Experimental conditions: 0.1 M  $\text{KHCO}_3$ ,  $-1.0$  V vs. RHE, 30 sccm  $\text{CO}_2$ . Reproduced from ref. 95 for (a) and ref. 149 for (b) with permission from Springer Nature, 2016, and the American Chemical Society, 2017.

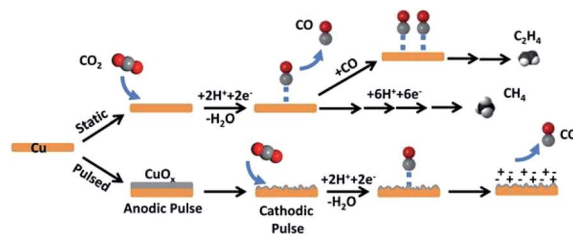


Fig. 20 Schematic diagram for  $\text{CO}_2$  reduction by pulsed-bias method and potentiostatic electrolysis. Reproduced from ref. 83 with permission from the American Chemical Society, 2016.





oxidation–reduction pretreatment, the activity and product selectivity were indeed improved, especially for the ratio of  $C_2H_4$  and  $CH_4$ , which has been proven by many research groups as above. Further mechanism investigations may focus on *in situ* and operando studies to gain more insight into the subsurface oxygen, chemical state or morphology of the  $Cu_xO$  catalyst under  $CO_2$  reduction conditions.

### 4.3 Cu–M bimetallic species

Combining Cu with other metals (M) to form alloys or separated Cu–M composites is another efficient approach to enhance the activity and selectivity for  $CO_2$  reduction. In this part, we summarize Cu–M alloys, including pure metallic alloys and oxide-derived alloys, as well as Cu–M bifunctional interfaces (separated Cu–M composites). For pure metallic alloys, the catalytic activity is affected by the nature of the secondary metal atom. Generally, CO selectivity is enhanced for Cu–M (M = In, Zn, Ag, Au) and  $HCOO^-$  for Cu–M (M = Sn, Pd), while hydrocarbon selectivity increases with increasing Cu atoms in the alloy. When the composition of ordered or separated arrangements is precisely controlled, different behavior will be observed and  $C_2$  products could be promoted. When the alloys are formed from oxide species, different behavior could also be observed, especially for oxide-derived blended and separated composites for  $C_2H_5OH$  production. There are electronic and geometric effects for each individual component of the alloy, while the geometric effects play important roles for separated Cu–M composites. Therefore, we may expect distinct performances of Cu–M bimetallic species *via* precise control of their atom and phase arrangements.

**Cu–M alloy.** Cu-based bimetallic electrocatalysts for  $CO_2$  reduction have been utilized since 1991, as reported by Watanabe and co-workers.<sup>165</sup> Cu alloys such as Cu–Ni, Cu–Sn, Cu–Pb, Cu–Zn, Cu–Cd, and Cu–Ag exhibited different catalytic activities compared to their respective elemental metals. Coupling Cu (d metal) with more oxyphilic materials (sp metals) such as Sn, In, Bi, and Sb might inhibit  $H_2$  evolution while enhancing the adsorption of CO and CHO to facilitate subsequent H addition.<sup>166</sup> G. Zangari and co-workers<sup>166</sup> prepared  $Cu_xIn_y$  electrodes with dendritic morphology by electrodeposition. At  $-1.0$  V vs. RHE (0.1 M  $KHCO_3$ ), the selectivity of  $HCOO^-$  could be up to 62% with 80 atom% In alloy, and the  $CO/H_2$  ratio could be tuned to 2.6 : 1 with 40 atom% In alloy. K. Takanabe and co-workers<sup>73</sup> thermally oxidized a Cu metal sheet to form a hairy  $CuO$  nanowire structure on  $Cu_2O$ –Cu layers. The CuIn electrode was then prepared through *in situ* electrochemical reduction of the oxide-derived Cu in a mixed solution of  $InSO_4$  and citric acid. High efficiency of CO was obtained (>70%) at low overpotential ( $-0.4$  V to  $-0.7$  V vs. RHE), with a maximum of 95% CO at  $-0.7$  V vs. RHE (0.1 M  $KHCO_3$ , 10 sccm  $CO_2$ ). Similar trends were also observed when using Sn and Zn as the second metals. DFT calculations suggested that In was preferentially located at the edges of the Cu surface ( $H_2$  evolution sites are presumably edges) and caused weakened adsorption of H over CO (high-overpotential metal for  $H_2$  formation), while the intact Cu corners might be still responsible for CO production. More

importantly, there was only a slight improvement in CO selectivity for the Cu–In electrode without initial oxidation treatment of the Cu sheet. They<sup>74</sup> also fabricated CuSn alloys using a similar electrodeposition method with initial oxidation. High CO selectivity with FE >90% over a wide potential range of  $-0.4$  V to  $-0.8$  V vs. RHE was achieved. According to their results, to improve the CO selectivity with CuIn or CuSn alloys, initial oxidation could be adopted. C. P. Berlinguette and co-workers<sup>67</sup> investigated ternary alloys of Cu–Zn–Sn for  $CO_2$  reduction to CO and  $HCOO^-$ . With an optimized ratio, >80% CO and  $HCOO^-$  could be achieved with a partial current density of  $3\text{ mA cm}^{-2}$  at an overpotential of 0.2 V (0.5 M  $NaHCO_3$ , 5 sccm  $CO_2$ ).

E. H. Sargent, P. D. Yang and co-workers<sup>89</sup> prepared a Cu-enriched Au nanoneedle electrode *via* an underpotential deposition (UPD) method with various Cu content. Designed syngas ratios were obtained (0.5 M  $KHCO_3$ , 20 sccm  $CO_2$ ). *In situ* SERS and DFT calculations illustrated how the surface electronic structure could be tuned by Cu enrichment to influence CO binding. Tuning the composition of CuAu alloys from Au-rich to Cu-rich resulted in a selectivity change from CO to hydrocarbon, which was also reported in other studies.<sup>167</sup> For Cu-rich alloys in another study, Au addition led to the suppression of  $CH_4$  while increasing CO production.<sup>168</sup> A. T. Bell and co-workers<sup>63</sup> prepared strained CuAg surface alloys *via* melting physical mixtures of Cu and Ag under argon in a vacuum arc furnace. The incorporation of Ag atoms onto the Cu surface modified the Cu electronic structure, where the valence band density states shifted to deeper levels. As a result, the binding energies of H and O relative to CO decreased and the ratio of CO to  $H_2$  products increased (0.05 M  $Cs_2CO_3$ , 5 sccm  $CO_2$ ). An AgCu dendritic catalyst was also electrodeposited on Cu foil and  $Ag_{57}Cu_{43}$  exhibited 2.2 times higher CO production than pure Ag in terms of Ag mass activity at  $-0.83$  V vs. RHE (0.5 M  $KHCO_3$ , 10 sccm  $CO_2$ ).<sup>76</sup> These results indicate that by alloying Cu with Au or Ag, the ratio of CO to  $H_2$  could be tuned. Additionally, additives during the electrodeposition process and the supports applied could affect the morphology of the deposited alloy and its corresponding activity for  $CH_4$  or  $C_{2+}$  products. Through the addition of 3,5-diamino-1,2,4-triazole into the electroplating solution, A. A. Gewirth and co-workers<sup>102</sup> obtained homogeneous CuAg wire samples, which exhibited higher selectivity than their counterparts of up to 60%  $C_2H_4$  and 25%  $C_2H_5OH$  at  $-0.7$  V vs. RHE (1.0 M KOH). T. Meyer and co-

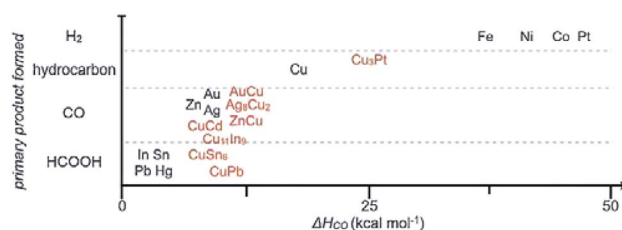


Fig. 21 General relationship between the primary product formed and CO heat of adsorption ( $\Delta H$ ) for pure metal and mixed metal films. Reproduced from ref. 171 with permission from Wiley, 2017.





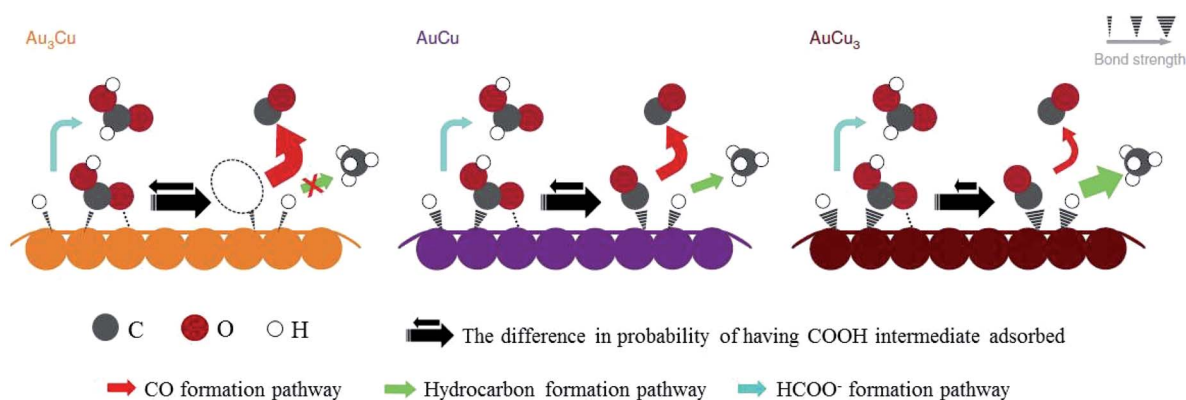


Fig. 22 Proposed mechanism for CO<sub>2</sub> reduction on the surface of Au–Cu bimetallic nanoparticles. Larger arrows indicate higher turnover. Reproduced from ref. 172 with permission from Springer Nature, 2014.

workers<sup>169</sup> electrodeposited  $\sim 6.6$  nm CuPd nanoalloy on a polymeric film. 51% CH<sub>4</sub> was obtained with Cu<sub>2</sub>Pd in organic electrolyte at an overpotential of  $-0.86$  V. They believed that the enhanced CH<sub>4</sub> formation was due to the synergistic interplay between Pd–H sites and Cu–CO sites with the polymer as a basis for local CO<sub>2</sub> concentration. Later, they<sup>170</sup> electrodeposited  $\sim 6$  nm CuAg nanoalloy on this polymer on glassy carbon. At  $0^\circ\text{C}$ , 21% C<sub>2</sub>H<sub>3</sub>OO<sup>−</sup> was achieved with Cu<sub>2</sub>Ag<sub>3</sub> at  $-1.33$  V vs. RHE in  $0.5$  M KHCO<sub>3</sub> with 8 ppm benzotriazole.

As stated before, we separately summarized the electrode used after fabrication without post-treatment and the powder materials used after assembly or drop casting to form films/electrodes. The following catalysts are Cu–M powder alloys, which sometimes have to be mixed with a Nafion binder and finally cast on a conductive substrate. Based on some groups' work, C. P. Berlinguette and co-workers<sup>171</sup> provided a general relationship between the primary product formed and the metal–CO bonding strength (Fig. 21). The best CO formation catalysts often had a CO heat of adsorption ( $\Delta H$ ) of  $10\text{ kcal mol}^{-1}$ . A lower value of  $\Delta H$  is more favorable for HCOO<sup>−</sup> formation, whereas a higher value of  $\Delta H$  favors H<sub>2</sub> and hydrocarbon formation. A series of In–M on titanium substrate was prepared and followed the trend FeIn < CoIn < ZnIn < NiIn < CuIn for CO production.

After preparing different ratios of Au<sub>*x*</sub>Cu<sub>*y*</sub> ( $x = 3, y = 1; x = 1, y = 1; x = 1, y = 3$ ) alloy nanoparticles, P. D. Yang and co-workers<sup>172</sup> obtained corresponding monolayer samples on various substrates *via* self-assembly by the Langmuir–Schaefer method. The monolayer samples showed great mass activity, achieving 67% CO with a partial current of  $-230\text{ mA mg}^{-1}$  at  $-0.73$  V vs. RHE for Au<sub>3</sub>Cu. The activity for CO<sub>2</sub> reduction exhibited a volcano shape, where Au<sub>3</sub>Cu represented the peak, as determined by the electronic and geometric effects (Fig. 22). These effects were associated with the local atomic arrangements at the active sites. In contrast to the AuCu alloys, alloying Pd with Cu could enhance CO and/or C<sub>2</sub> products. M. Yamachi, P. J. A. Kenis and co-workers<sup>86</sup> designed CuPd nanoalloys with ordered, disordered, and phase-separated elemental arrangements (Fig. 23). With the same atomic ratio, phase-

separated arrangements (more sites with neighbouring Cu atoms) favored the production of C<sub>2</sub> products compared to the other two arrangements, with >60% (48% C<sub>2</sub>H<sub>4</sub> and 15% C<sub>2</sub>H<sub>5</sub>OH) at  $-0.7$  V vs. RHE. CuPd with ordered arrangements gave 75% CO at  $-0.7$  V vs. RHE. Surface valence bond spectra suggested that geometric effects were key in determining the selectivity compared to electronic effects. N. Umezawa, J. H. Ye and co-workers<sup>173</sup> electrodeposited CuPd on glassy carbon and optimized the ratio between Pd and Cu. 80% faradaic efficiency of CO was obtained with optimal Pd<sub>7</sub>Cu<sub>3</sub> at  $-0.8$  V vs. RHE. DFT calculations suggested that synergistic geometric and electronic

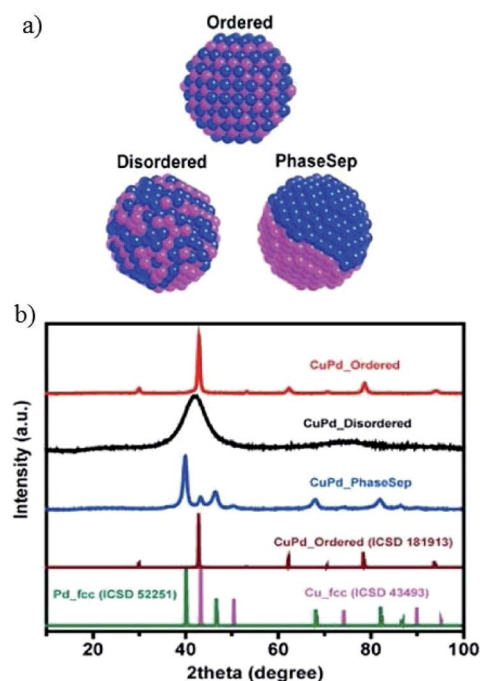


Fig. 23 (a) Illustration of prepared CuPd nanoalloys with different atomic mixing patterns: ordered, disordered, and phase separated. (b) XRD patterns of prepared CuPd nanoalloys, as well as previously reported pure Cu, pure Pd and CuPd alloys. Reproduced from ref. 86 with permission from the American Chemical Society, 2017.



effects were responsible for the high selectivity. D. Ma, G. X. Wang and co-workers<sup>174</sup> loaded CuPd nanoparticles (3.3 nm) on carbon black, and Pd<sub>85</sub>Cu<sub>15</sub>/C achieved 86% CO at −0.89 V vs. RHE.

**Cu–M bifunctional interface.** Compared with Cu alloys, separated Cu–M composites have shown their own advantages in tuning product selectivity. *Via* theoretical calculations, Y. S. Jung, Y. T. Kim and co-workers<sup>175</sup> found that a Au–Cu bifunctional interface was more favorable for the stabilizing \*COOH intermediate (Fig. 24a) and its intrinsic electronic properties were less affected compared to the bulk alloy. T. Takashima and co-workers<sup>176</sup> synthesized atomic layers of Cu on Pd particles (Cu–Pd) without the formation of an alloy by underpotential deposition. They ascribed the improved CO tolerance and HCOO<sup>−</sup> production to the charge transfer from Pd to Cu and a downward shift of the d band centre to the Fermi level (0.5 M NaHCO<sub>3</sub>, 16 sccm CO<sub>2</sub>). Additionally, C<sub>2</sub>H<sub>5</sub>OH selectivity could be promoted on a Cu–M bifunctional surface *via* a two-site mechanism. B. S. Yeo and co-workers<sup>84</sup> electrodeposited Cu–Zn oxides with various amounts of Zn dopants, which exhibited different C<sub>2</sub>H<sub>5</sub>OH selectivities. XRD did not show any alloy signals except separated Cu and Zn. The maximum faradaic efficiency of 29% C<sub>2</sub>H<sub>5</sub>OH was obtained on Cu<sub>4</sub>–Zn at −1.05 V vs. RHE (0.1 M KHCO<sub>3</sub>, 20 sccm CO<sub>2</sub>). J. Y. Lee and co-workers<sup>177</sup> incorporated Ag in Cu<sub>2</sub>O by electrodeposition and found that phase blended Ag–Cu<sub>2</sub>O exhibited higher C<sub>2</sub>H<sub>5</sub>OH selectivity (34%) than its phase separated counterpart (20%), with 3 times the selectivity of Cu<sub>2</sub>O (11%) at −1.2 V vs. RHE, as illustrated in Fig. 24b. This was because of the role of the Ag dopant and the closer distance between Ag and Cu was efficient for the insertion of CO on Ag sites to other C<sub>1</sub> intermediates on Cu sites, as illustrated in Fig. 24c.

To design Cu–M bimetallic species, therefore, the first aspect to be considered is the group that the parent metals belong to. The preparation method also has an influence on the activity.

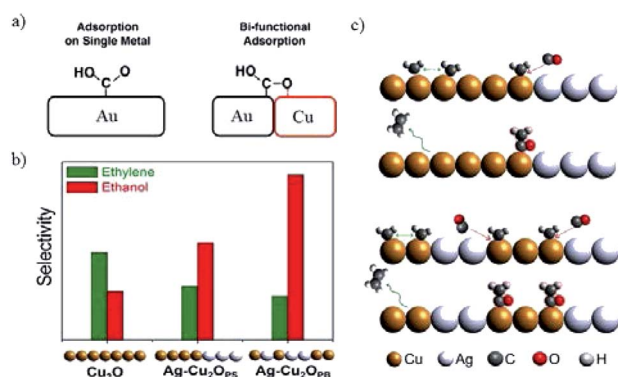


Fig. 24 (a) The stabilization of \*COOH by introducing bi-functional effects. (b) The selectivity of C<sub>2</sub>H<sub>4</sub> and C<sub>2</sub>H<sub>5</sub>OH for Cu<sub>2</sub>O and Ag-incorporated Cu<sub>2</sub>O. Experimental conditions: −1.2 V vs. RHE in 0.2 M KCl. (c) The proposed CO-insertion mechanism indicating the transfer of CO from Ag site that weakly binds CO to Cu site that binds residual C<sub>1</sub> intermediates in the case of phase separated and phase blended samples in (b). Reproduced from ref. 175 for (a) and ref. 177 for (b) and (c) with permission from the American Chemical Society, 2016 and 2017.

The most important thing for mechanism investigation in this system is precise control of the composition, morphology and position of the bimetallic species.

#### 4.4 Surface modification of Cu-based electrocatalysts

In recent years, surface modification has also been investigated for Cu-based electrocatalysts, including inorganic and organic outlayer species. Inorganic overlayers could protect the Cu surface and alter the direct contact between the electrolyte and Cu surface. Then the stability and activity could be altered compared to bare Cu-based electrocatalysts. Y. J. Liang, H. L. Wang and co-workers<sup>60</sup> decorated Pd atoms on Cu mesh by soaking it in PdCl<sub>2</sub> + HCl solution. During CO<sub>2</sub> reduction, the foreign Pd atoms induced continuous restructuring of the Cu surface, in turn preventing the deactivation of catalysts by incorporating or desorbing accumulated carbonaceous species (Fig. 25). The deactivation of electrodes caused by the adsorption of carbon or intermediates has been reported by many researchers.<sup>24,178,179</sup> According to their reports, the Pd content should be optimized to inhibit the deactivation of the Cu electrode and maintain the CO<sub>2</sub> reduction activity, since less Pd is not sufficient to improve catalyst durability, while more Pd will change the product selectivity and lead to more H<sub>2</sub> production. The selectivity of CH<sub>4</sub> and C<sub>2</sub>H<sub>4</sub> remained above 50% for 4 h continuous electrolysis at −0.96 V vs. RHE (0.5 M KHCO<sub>3</sub>, 20 sccm). J. P. Ramírez and co-workers<sup>180</sup> found that Cu–In nano-alloys evolved to a separated core–shell (Cu–In(OH)<sub>3</sub>) structure after successive electrochemical cycles. The separated catalysts with an In(OH)<sub>3</sub> shell showed high selectivity for CO production, and In(OH)<sub>3</sub> modification plays an important role in this enhanced selectivity. Later, they also observed >80% HCOO<sup>−</sup> at −0.8 V vs. RHE (0.1 M KHCO<sub>3</sub>) with submicron S-modified Cu.<sup>181</sup> J. S. Luo, M. Grätzel and co-workers<sup>61</sup> modified the surface of CuO nanowire electrodes with SnO<sub>2</sub> *via* atomic layer deposition (ALD) and as high as 97% CO was achieved at −0.7 V vs. RHE (10 sccm CO<sub>2</sub>). Gas phase absorption measurements confirmed the significantly decreased binding strength of both CO and adsorbed H\* after SnO<sub>2</sub> modification. However, whether the residual oxides (mainly Sn<sup>2+</sup> with some Cu<sup>+</sup>) were active catalysts remained uncertain.

Besides modification with inorganic materials, organic ligands are coated on the Cu surface to enhance CO<sub>2</sub> reduction, especially for CH<sub>4</sub> and C<sub>2</sub>H<sub>4</sub> products through the interactions between key intermediates and the functional groups of

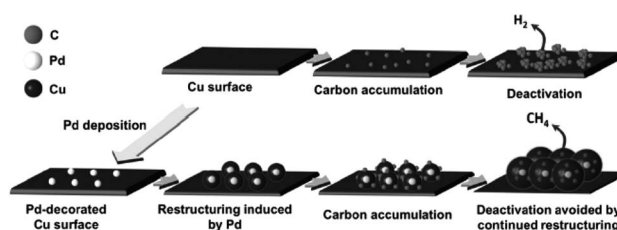


Fig. 25 Schematic diagram of Pd-induced surface restructuring that avoids the accumulation of carbonaceous species on the Cu surface. Reproduced from ref. 60 with permission from Wiley, 2017.



ligands. By properly modifying Cu(OH)<sub>2</sub> nanowires with amino acid,<sup>182</sup> H<sub>2</sub> formation could be suppressed and CO<sub>2</sub> reduction was promoted since the interaction between the key intermediate CHO\* and -NH<sub>3</sub><sup>+</sup> of the adsorbed zwitterionic glycine stabilized this key intermediate during CO<sub>2</sub> reduction. E. Andreoli and co-workers<sup>183</sup> modified the Cu foam surface with polyamide and obtained enhanced C<sub>2</sub>H<sub>4</sub> production with unaffected CH<sub>4</sub> (0.1 M NaHCO<sub>3</sub>). They ascribed this enhancement to the charge transfer to the Cu surface, stabilization of the CO dimer by the -NH<sub>2</sub> group, and the adsorption of CO near the polymer.

#### 4.5 Supports for Cu-based electrocatalysts

We list all the substrates and/or supports in Table 2, since supports also have an influence on activity. Supports can maintain good dispersion and stabilization of active sites, as well as creating synergistic interactions or active interfaces between supports and copper catalysts. CuO on CO<sub>2</sub> capture material exhibited higher C<sub>2</sub>H<sub>4</sub> faradaic efficiency than CuO on carbon black or without support.<sup>184</sup> Supports with sufficient surface area were also critical for the high C<sub>2</sub>-C<sub>3</sub> products for densely packed Cu nanoparticles.<sup>122</sup> Electrodeposited Cu gave higher activity on graphene oxide and pure graphite than on glassy carbon, which was attributed to the preferential deposition of Cu nanoparticles at defects present on the graphene layers of the former supports.<sup>57</sup>

Generally, Cu foil, Cu plate, Cu mesh, or even FTO is used as a substrate for Cu-based electrocatalysts for EC CO<sub>2</sub> reduction, while glassy carbon is used for Cu powder electrocatalysts. Gas diffusion layers (GDL) or gas diffusion electrodes (GDE) were also chosen as substrates to enhance the performance of the corresponding loaded Cu-based electrocatalysts due to their gas/electrolyte penetrability.<sup>86,150</sup> Polymer on FTO<sup>169</sup> or glassy carbon<sup>170</sup> was used as a substrate to enhance the local concentration of CO<sub>2</sub>. Polymer-based diffusion layers or electrodes have also been fabricated recently to enhance the activity and stability of Cu electrocatalysts, where as high as 76% C<sub>2</sub>H<sub>4</sub> was obtained at -0.55 V vs. RHE.<sup>103,185</sup>

Therefore, in order to improve the performance of Cu-based electrocatalysts, supports or substrates with high surface area and high gas and liquid penetrability should be considered. More recently, it was found that Cu<sub>3</sub>N support could act as an underlying stable Cu<sup>+</sup> species to reduce the CO dimerization energy barrier.<sup>186</sup> This might be another consideration when choosing supports for copper electrocatalysts.

## 5. Electrolyte effect on CO<sub>2</sub> reduction with Cu-based heterogeneous electrocatalysts

In EC CO<sub>2</sub> reduction, aqueous electrolytes are generally selected by researchers due to their environmentally friendly properties, low cost and potential for coupling with water oxidation. Non-aqueous electrolytes are also studied by many researchers due to their large electrochemical window, high CO<sub>2</sub> solubility and low proton availability.

### 5.1 Aqueous electrolytes

In a pioneering study, Hori and co-workers<sup>34</sup> investigated CO<sub>2</sub> reduction on Cu sheet electrodes in various electrolytes at 5 mA cm<sup>-2</sup>. The major product was H<sub>2</sub> with FE >70% in KH<sub>2</sub>PO<sub>4</sub>/K<sub>2</sub>HPO<sub>4</sub>, which decreased to 10% in KClO<sub>4</sub>. C<sub>2</sub>H<sub>4</sub> and alcohols were favored in KCl, K<sub>2</sub>SO<sub>4</sub>, KClO<sub>4</sub> and diluted KHCO<sub>3</sub> electrolytes, whereas CH<sub>4</sub> was favored in concentrated KHCO<sub>3</sub> and KH<sub>2</sub>PO<sub>4</sub>/K<sub>2</sub>HPO<sub>4</sub>.

The concentration of bicarbonate and cation size both play important roles during CO<sub>2</sub> reduction. A high concentration of bicarbonate leads to a relatively high pH, which in turn favors CH<sub>4</sub> formation, while a big cation size promotes C<sub>2</sub>H<sub>4</sub> and other C<sub>2</sub> products. G. Mul and co-workers<sup>24</sup> investigated the influence of the electrolyte on the selectivity of Cu<sub>2</sub>O-derived Cu. An increased electrolyte concentration led to a decreased C<sub>2</sub>H<sub>4</sub>/CH<sub>4</sub> ratio (0.05 M, 0.1 M, 0.2 M KHCO<sub>3</sub>, 50 sccm CO<sub>2</sub>). P. Strasser and co-workers<sup>25</sup> also observed that a low concentration of bicarbonate electrolyte favored H<sub>2</sub> and CH<sub>4</sub> formation, while a high concentration of bicarbonate, which showed a high interfacial pH near the Cu surface, favored C<sub>2</sub>H<sub>4</sub> formation (0.05 to 0.2 M KHCO<sub>3</sub>). For various different concentrations of electrolytes, E. H. Sargent, D. Sinton and co-workers<sup>79</sup> predicted the pH and CO<sub>2</sub> concentration at the electrode surface using a diffusion-based model (Fig. 26). CO<sub>2</sub> limitation occurred under high local pH conditions. In 1991, Hori and co-workers found that cationic species (Li<sup>+</sup>, Na<sup>+</sup>, K<sup>+</sup> and Cs<sup>+</sup>) in bicarbonate solution affected the product selectivity (C<sub>2</sub>H<sub>4</sub>/CH<sub>4</sub>).<sup>187</sup> A. T. Bell and co-workers<sup>188,189</sup> recently also reported that there was a decrease in faradaic efficiency for H<sub>2</sub> and CH<sub>4</sub>, and an increase in faradaic efficiency for C<sub>2</sub>H<sub>4</sub> and C<sub>2</sub>H<sub>5</sub>OH for Cu cathodes with increasing cation size (Li<sup>+</sup>, Na<sup>+</sup>, K<sup>+</sup>, Rb<sup>+</sup>, and Cs<sup>+</sup>) (Fig. 27a). They ascribed the effect of the electrolyte cation size on CO<sub>2</sub> reduction to cation hydrolysis in the vicinity of the cathode. The pK<sub>a</sub> for hydrolysed cations decreased and they served as buffer agents to lower the local pH, leading to an increase in the local concentration of dissolved CO<sub>2</sub> (Fig. 27b and c). The concentration of molecular CO<sub>2</sub> decreased with increasing pH due to its rapid consumption by hydroxyl anions to form HCO<sub>3</sub><sup>-</sup> and CO<sub>3</sub><sup>2-</sup>. This process occurred at much higher rates than the rate of CO<sub>2</sub> reduction. In contrast to CO<sub>2</sub> reduction, by using single-crystal Cu(100), single-crystal Cu(111), and polycrystalline Cu electrodes, M. T. Koper, F. C. Vallejo and co-workers<sup>190</sup> found that the cation effects were potential- and structure-dependent

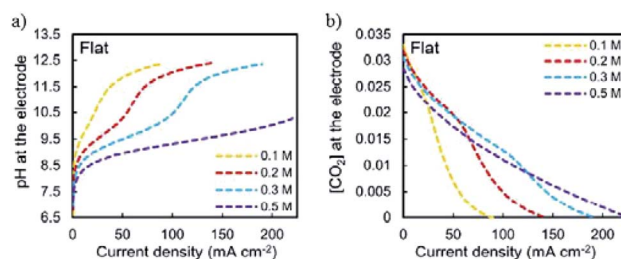


Fig. 26 (a) Predicted local pH and (b) CO<sub>2</sub> concentration at the electrode surface using a diffusion-based model. Reproduced from ref. 79 with permission from the Royal Society of Chemistry, 2017.





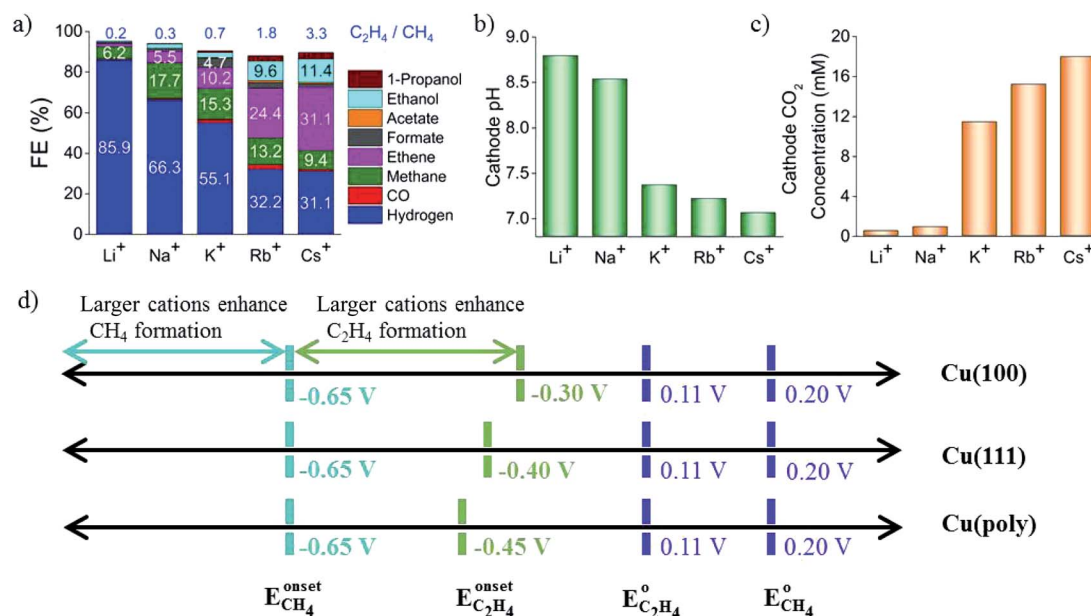


Fig. 27 (a) The selectivity of CO<sub>2</sub> reduction products in different bicarbonate electrolytes. (b) Calculated local pH. (c) CO<sub>2</sub> concentration at the Cu surface. Schematics of structure- and potential-dependent cation effects. Experimental conditions:  $-1.0$  V vs. RHE,  $0.1$  M LiHCO<sub>3</sub>, NaHCO<sub>3</sub>, KHCO<sub>3</sub>, RbHCO<sub>3</sub>, and CsHCO<sub>3</sub>. Reproduced from ref. 188 for (a) to (c) and ref. 190 for (d) with permission from the American Chemical Society, 2016 and 2017.

in CO reduction (Fig. 27d); the onset potential for C<sub>2</sub>H<sub>4</sub> was lower for the single crystals ( $-0.3$  V and  $-0.4$  V vs. RHE for Cu(100) and Cu(111)) than for the polycrystalline electrode, for which the overpotential increased with increasing cation size. The onset potential for CH<sub>4</sub> ( $-0.65$  V vs. RHE) was independent of both cation size and surface structure. When the applied potential was more negative than  $-0.65$  V vs. RHE, larger cations enhanced CH<sub>4</sub> formation. When the applied potential was from  $-0.65$  V to  $-0.3$  V vs. RHE, larger cations increased C<sub>2</sub>H<sub>4</sub> selectivity.

Halides are sometimes directly added into aqueous electrolytes to enhance the CO<sub>2</sub> reduction and suppress the competing H<sub>2</sub> evolution. P. Strasser and co-workers<sup>191</sup> added various concentrations of halides into KHCO<sub>3</sub> electrolytes and observed that the addition of Cl<sup>−</sup> and Br<sup>−</sup> resulted in increased CO selectivity. The adsorbed I<sup>−</sup> exhibited a larger effect on CH<sub>4</sub> production than C<sub>2</sub>H<sub>4</sub>. The probable reason was the induced negative charge possessed a remarkably positive effect favoring the protonation of CO. KCl was also used as a catholyte because it resulted in a higher local pH and the formation of bi-phasic Cu<sub>2</sub>O–Cu, favored for multicarbon fuel production.<sup>177</sup>

As indicated above, high concentrations, large cation sizes and halide additives could be considered for CO<sub>2</sub> reduction in bicarbonate electrolytes in order to obtain more hydrocarbon products. Moreover, regarding the role of bicarbonate aqueous electrolytes, recently M. H. Shao's group<sup>192</sup> directly observed that CO<sub>2</sub> molecules were mediated to the Cu surface *via* their equilibrium with bicarbonate anions rather than direct adsorption from the solution (Fig. 28), using attenuated total

reflection surface-enhanced infrared absorption spectroscopy, isotopic labelling, and potential stepping techniques.

## 5.2 Non-aqueous solvents

**Organic electrolytes.** Organic solvents have been studied in CO<sub>2</sub> reduction since the early 1980s.<sup>193,194</sup> Although organic solvents have environmental and safety issues, these solvents possess unique advantages in EC CO<sub>2</sub> reduction, such as (1) large electrochemical window. For example, with  $0.65$  M supporting electrolyte, the reduction/oxidation potential window is  $-2.8$  V to  $+3.3$  V vs. SCE for acetonitrile (MeCN),  $-3.0$  V to  $+1.6$  V vs. SCE for dimethylformamide (DMF), and  $-2.9$  V to  $+1.5$  V vs. SCE for dimethyl sulfoxide (DMSO). (2) Low proton availability: thus, the application of organic solvent could suppress the competing H<sub>2</sub> evolution reaction

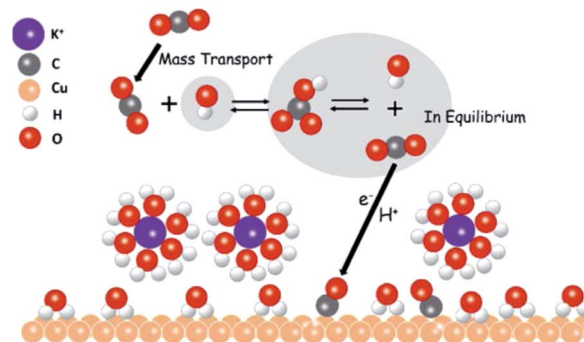


Fig. 28 The proposed role of bicarbonate anions in EC CO<sub>2</sub> reduction. Reproduced from ref. 192 with permission from the American Chemical Society, 2017.



and improve the total faradaic efficiency for CO<sub>2</sub> reduction. (3) High CO<sub>2</sub> solubility: in 2000, Hori's group also studied the Pt system in MeCN–H<sub>2</sub>O mixtures. They showed that the CO<sub>2</sub> concentration could be up to 270 mM in MeCN with a low water concentration, 8 times higher than in aqueous solution (33 mM),<sup>195</sup> as shown in Fig. 29. We will discuss recent work on EC CO<sub>2</sub> reduction with Cu-based heterogeneous catalysts in organic electrolytes.<sup>196–199</sup> In these studies, the organic electrolyte contained 0.1 M supporting electrolyte, such as tetrabutylammonium tetrafluoroborate (nBu<sub>4</sub>NBF<sub>4</sub>), tetraethylammonium tetrafluoroborate (TEABF<sub>4</sub>), tetraethylammonium trifluoromethanesulfonate (TEATfO) and sodium trifluoromethanesulfonate (NaTfO), to enhance the conductivity of the organic system. V. Artero, M. Fontocave and co-workers<sup>196</sup> electrodeposited [Cu(cyclam)](ClO<sub>4</sub>)<sub>2</sub> complex (cyclam = 1,4,8,11-tetraazacyclotetradecane) on FTO. The composite formed (Cu, CuO complex) achieved 90% HCOO<sup>−</sup> at −2.0 V vs. Fc<sup>+</sup>/Fc in DMF/H<sub>2</sub>O (97 : 3 v/v), which is much higher than that in aqueous solution. However, the current density is only −1.15 mA cm<sup>−2</sup>. They<sup>197</sup> also electrodeposited Cu<sub>2</sub>O on FTO and achieved almost 90% HCOO<sup>−</sup> in DMF/H<sub>2</sub>O (99 : 1, v/v) at −2.0 V vs. Fc<sup>+</sup>/Fc with current density −1.5 mA cm<sup>−2</sup>. Z. C. J. Xu and co-workers<sup>199</sup> tuned Cu electrodeposition by the addition of phosphate buffer and obtained 80% HCOO<sup>−</sup> selectivity at −1.45 V vs. NHE in MeCN (*E*<sub>1/2</sub> of Fc<sup>+</sup>/Fc couple was 0.40 V vs. NHE in MeCN), with current density −1.35 mA cm<sup>−2</sup>.

**Ionic liquids.** In the past 15 years, ionic liquid has been emerged as a promising candidate for CO<sub>2</sub> capture.<sup>200</sup> Ionic liquid also possesses a large potential window. It has been reported that ionic molecules could complex with CO<sub>2</sub><sup>2−</sup> intermediates to reduce the energy barriers or potentials for Ag-based systems<sup>201</sup> and could change the selectivity for Bi-based systems.<sup>202–204</sup> The controlled selectivity of CO<sub>2</sub> reduction with Cu nanoparticles-modified boron-doped diamond electrode in 1-ethyl-3-methylimidazolium tetrafluoroborate (EMIM·BF<sub>4</sub>) ionic liquid was also achieved.<sup>205</sup> Using porous (30–40 μm) dendritic copper nanofoam (10 wt% Cu<sub>2</sub>O) in ionic liquid–water mixture [EMIM](BF<sub>4</sub>)/H<sub>2</sub>O (92/8 v/v) as the electrolyte, V. Artero, M. Fontocave and co-workers<sup>206</sup> obtained almost 90% HCOO<sup>−</sup> at −1.55 V vs. Fc<sup>+</sup>/Fc with current density −5.0 mA

cm<sup>−2</sup>, a much lower potential than that required in their former work without ionic liquid.<sup>196,197</sup>

Therefore, organic solvents and ionic liquids are better choices for suppressing H<sub>2</sub> evolution in catalyst systems not suitable for aqueous solutions. In aqueous systems, alkaline conditions could promote C–C coupling during CO<sub>2</sub> reduction.<sup>207,208</sup> For the ultimate goal of CO<sub>2</sub> recycling, neutral aqueous solution is the best choice and various concentrations and cations could be applied to tune the activity.

## 6. EC/PEC CO<sub>2</sub> reduction and H<sub>2</sub>O oxidation as an overall reaction system for Cu-based electrocatalysts

### 6.1 EC

The EC CO<sub>2</sub> reduction and H<sub>2</sub>O splitting produces carbon-based fuels and oxygen. Realizing the overall reaction with one catalyst in a single device is desirable. In such a system, the catholyte and anolyte may be different for specific half reactions. T. J. Meyer and co-workers<sup>209</sup> combined two half reactions catalyzed by Cu(II)/Cu(0) electrode. As shown in Fig. 30, the electrode for CO<sub>2</sub> reduction into CO/HCOO<sup>−</sup> was Cu(0) film electrodeposited on a boron-doped diamond electrode. A boron-doped diamond electrode immersed in Cu(II) was used for H<sub>2</sub>O oxidation into O<sub>2</sub>. This report demonstrates that a simple Cu(II)/Cu(0) electrode is sufficient to catalyze CO<sub>2</sub> reduction and H<sub>2</sub>O splitting in neutral aqueous solution with a H-type cell. However, more aspects should be considered when choosing different catholytes and anolytes, for example the membrane used in the H-type cell. By using SnO<sub>2</sub>-modified CuO nanowire electrodes as both the cathode for CO<sub>2</sub> reduction and the anode for the oxygen evolution reaction, J. S. Luo, M. Grätzel and co-workers<sup>61</sup> constructed a complete CO<sub>2</sub> electrolysis system with a bipolar membrane. Bipolar membranes consisting of a cation exchange layer and an anion exchange layer were also investigated in other systems for CO<sub>2</sub> reduction and H<sub>2</sub>O oxidation with different catholytes and anolytes. Bipolar membranes needed a lower cell voltage than monopolar membranes.<sup>210</sup>

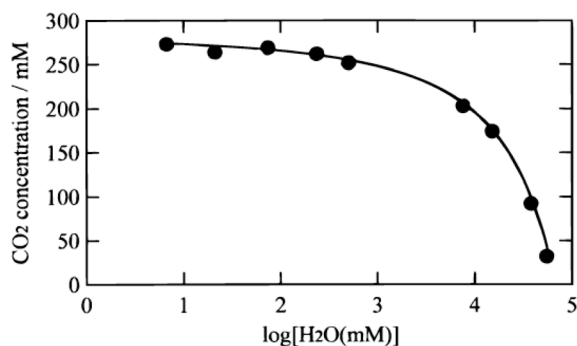


Fig. 29 CO<sub>2</sub> concentration in a mixture of CH<sub>3</sub>CN and H<sub>2</sub>O versus the H<sub>2</sub>O content. Reproduced from ref. 195 with permission from the Electrochemical Society, 2000.

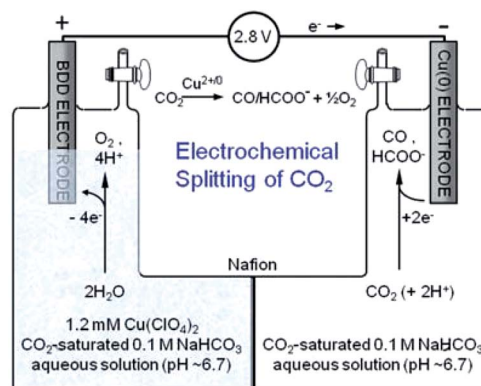


Fig. 30 Schematic diagram for overall reaction of CO<sub>2</sub> reduction and H<sub>2</sub>O oxidation using Cu electrode in H-type cell. Reproduced from ref. 209 with permission from the Royal Society of Chemistry, 2013.



## 6.2 PEC

Solar energy is the largest source of renewable energy. Coupling solar irradiation with EC CO<sub>2</sub> reduction is of considerable interest.<sup>211,212</sup> In this review, we do not discuss photocatalytic (PC) CO<sub>2</sub> reduction with Cu-based materials; readers interested in this topic are directed to some recent reports, including of p-type CuI,<sup>213</sup> Cu-decorated TiO<sub>2</sub>,<sup>214</sup> CuO nanoclusters on Nb<sub>3</sub>O<sub>8</sub> nanosheets,<sup>215</sup> Au–Cu nanoalloys supported on TiO<sub>2</sub>,<sup>216</sup> carbon-decorated Cu<sub>2</sub>O mesoporous nanorods,<sup>217</sup> *etc.* We will focus on photoelectrochemical (PEC) CO<sub>2</sub> reduction with Cu-based catalysts, where similar photoelectrolysis cells as for PEC water splitting are made for PEC CO<sub>2</sub> reduction.

In a PEC CO<sub>2</sub> reduction system, sunlight, visible light and UV light are three options for the light source. For the purpose of solar energy utilization, sunlight irradiation without bias potential is the ultimate goal. Cu<sub>2</sub>O with a direct band gap of ~2.0 eV is a promising material for enhancing CO<sub>2</sub> activity and inhibiting H<sub>2</sub> evolution in PEC CO<sub>2</sub> reduction systems. N. R. Tacconi, K. Rajeshwar and co-workers<sup>218,219</sup> first reported the utilization of Cu<sub>2</sub>O for CO<sub>2</sub> PEC reduction. They electrodeposited Cu<sub>2</sub>O nanocrystals on CuO nanorod arrays. 95% CH<sub>3</sub>OH was formed with a bias potential of +0.17 using this CuO@Cu<sub>2</sub>O nanorod array as a photocathode (AM 1.5, 70 mW cm<sup>-2</sup>). Modifying the Cu-based photocathode could lead to different enhanced CO<sub>2</sub> reduction products. L. R. Baker and co-workers<sup>220</sup> electrodeposited CuFeO<sub>2</sub>/CuO on FTO and used it as a photocathode. 80% CH<sub>3</sub>COO<sup>-</sup> was detected with a bias potential of +0.2 V under white-light LED illumination (100 mW cm<sup>-2</sup>). P. D. Yang and co-workers<sup>221</sup> directly assembled Au<sub>3</sub>Cu nanoparticles on the surface of TiO<sub>2</sub>-protected silicon nanowire as a photocathode. Compared with the planar counterpart, lower overpotential or additional bias (~120 mV lower) was needed to drive CO<sub>2</sub> reduction to CO. 80% CO could be achieved at -0.2 V vs. RHE (LED light source with intensity 20 mW cm<sup>-2</sup>, wavelength  $\lambda$  = 740 nm).

When Cu-based electrocatalysts are used as a cathode, both the cathode and the photoanode could be manipulated to

enhance the performance of the overall system. J. S. Lee and co-workers<sup>222</sup> constructed a PEC system comprising a WO<sub>3</sub> photoanode and Cu cathode for CO<sub>2</sub> reduction. 71.6% carbonic products (65% CH<sub>4</sub>) were obtained at +0.65 V vs. RHE under visible light irradiation (>420 nm). M. Miyauchi, H. Abe and co-workers<sup>223</sup> obtained 79% HCOO<sup>-</sup> when using Cu–Zn alloy film as a cathode in 0.1 M KHCO<sub>3</sub> and SrTiO<sub>3</sub> as a photoanode in 0.1 M KCl + 0.01 M NaOH under UV light illumination without applied bias potential. Y. S. Kang and co-workers<sup>224</sup> engineered a (040) facet BiVO<sub>4</sub> photoanode and integrated it with a Cu cathode for CO<sub>2</sub> PEC reduction (Cu cathode|NaCl|BiVO<sub>4</sub> photoanode). Different products were obtained by tuning the bias potential, such as 65.4% HCOO<sup>-</sup> (+0.75 V), 85.1% HCHO (+0.9 V), 6.89% CH<sub>3</sub>OH and 4.4% C<sub>2</sub>H<sub>5</sub>OH (+1.35 V) in 0.5 M NaCl (AM 1.5).

When using Cu<sub>x</sub>O as a photocathode or cathode, corrosion will happen. Protective layers such as TiO<sub>2</sub> were applied in studies done well by M. Grätzel's group. J. L. Gong and co-workers<sup>225</sup> introduced a simple strategy by using Cu<sub>2</sub>O as the cathode and TiO<sub>2</sub> nanorods as the photoanode for PEC reduction of CO<sub>2</sub>. 92.6% carbonic products (54% CH<sub>4</sub>, 30% CO, 3% CH<sub>3</sub>OH) were obtained at +0.75 V vs. RHE bias potential (AM 1.5, 100 mW cm<sup>-2</sup>). Through cut-off filter experiments, they confirmed that the photogenerated electrons were not the main reason for Cu<sub>2</sub>O corrosion; instead, photogenerated holes were primarily responsible for the instability of Cu<sub>2</sub>O. As shown in Fig. 31, the photogenerated electrons were consumed at the electrode/electrolyte interface, while the holes moved to the back contact and the counter electrode. Back illumination (the travel distance of the electrons was longer than that of the holes) was favorable for the stability of Cu<sub>2</sub>O.

The photocurrent density is relatively low for the above reported systems, as listed in Table 2. One future aim is to improve the photocurrent density in PEC CO<sub>2</sub> conversion. Constructing a hybrid catalyst consisting of a molecular catalyst and semiconductor material for PEC CO<sub>2</sub> reduction could improve the selectivity and efficiency.<sup>226–228</sup> For a hybrid system, careful design of the semiconductor is also important. As shown in Fig. 32a, M. T. Mayer, M. Grätzel and co-workers<sup>229</sup> designed a heterogeneous catalyst system by

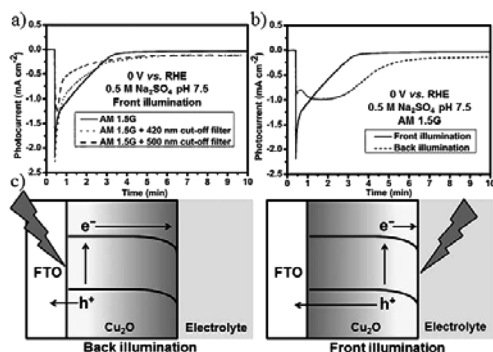


Fig. 31 Photocurrent–time curves of Cu<sub>2</sub>O photocathode under (a) different light sources and (b) front and back illumination. Experimental conditions: 0.5 M N<sub>2</sub>-saturated Na<sub>2</sub>SO<sub>4</sub>, 0 V vs. RHE, 100 mW cm<sup>-2</sup>. (c) The travel distances of electrons and holes under front and back illumination. Reproduced from ref. 225 with permission from Wiley, 2016.

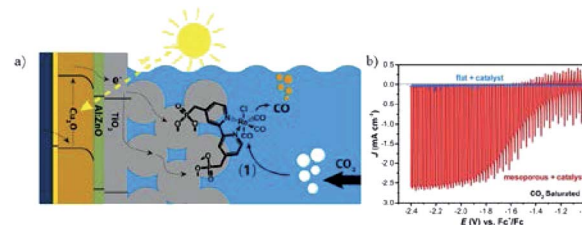


Fig. 32 (a) Schematic of hybrid system of protected Cu<sub>2</sub>O photocathode with covalent-bound Re(bpy)(CO)<sub>3</sub>Cl. (b) Corresponding PEC performance with and without mesoporous TiO<sub>2</sub> layer on the surface of protected Cu<sub>2</sub>O photocathode. Experimental conditions: CO<sub>2</sub>-saturated CH<sub>3</sub>CN (0.1 M Bu<sub>4</sub>NPF<sub>6</sub>), scan rate 10 mV s<sup>-1</sup>, 100 mW cm<sup>-2</sup>. Reproduced from ref. 229 with permission from the American Chemical Society, 2016.



covalently immobilizing molecular  $\text{Re}(\text{bpy}) (\text{CO})_3\text{Cl}$  onto a  $\text{TiO}_2$ -protected  $\text{Cu}_2\text{O}$  photocathode ( $\text{Cu}_2\text{O}/\text{AZO}/\text{TiO}_2$ ) *via* phosphonate linkers. On the  $\text{TiO}_2$  layer there was also a mesoporous film of 4.5 to 5  $\mu\text{m}$  thickness with 18 nm  $\text{TiO}_2$  particles. The catalyst system without mesoporous  $\text{TiO}_2$  did not show substantial photocurrents, while mesoporous  $\text{TiO}_2$  (enhanced roughness and catalyst loading) exhibited enhanced photocurrents (Fig. 32b). 80–95% CO was achieved under chopped light illumination with photocurrent density of  $2.5 \text{ mA cm}^{-2}$  at  $-1.9 \text{ V vs. Fc}^+/\text{Fc}$ .

### 6.3 PV cells or PV-electrolyzers

The potential bias could be supplied by other forms of energy for PEC electrocatalysis, such as solar PV panels.<sup>36,212,230–233</sup> The first idea to apply PV cells for PEC water splitting into hydrogen and oxygen was proposed in 1995 (ref. 234) and has been widely used, whereas its use for the overall reaction of  $\text{CO}_2$  reduction and  $\text{H}_2\text{O}$  oxidation was reported in 2008 (ref. 235) and there are very few examples for the overall reaction system. Recently, J. S. Luo, M. Grätzel and co-workers<sup>61</sup> designed a triple-junction  $\text{GaInP}/\text{GaInAs}/\text{Ge}$  solar cell driving a  $\text{CuO}/\text{SnO}$  photocathode/photoanode system (Fig. 33a). At a voltage of 2.38 V (AM 1.5,  $100 \text{ mW cm}^{-2}$ ), a solar-to-CO free-energy

conversion efficiency peaking at 13.4% with 81% CO selectivity was obtained at  $-0.55 \text{ V vs. RHE}$  (Fig. 33b) and the photocurrent could be up to  $12 \text{ mA cm}^{-2}$ .

The use of other forms of sustainable energy such as solar energy to drive the overall reaction of  $\text{CO}_2$  reduction and water splitting is promising.  $\text{Cu}_x\text{O}$  could be used as both a cathode and photocathode after surface protection, as stated above. It is also promising to use Cu oxide species directly as cathodes and photocathodes, since the Schottky junction between  $\text{Cu}_2\text{O}$  and Cu could facilitate electron and hole separation, leading to enhanced activity.<sup>236</sup> The morphology and activity evolution of  $\text{Cu}_x\text{O}$  is worthy of further investigation because the chemical changes of  $\text{Cu}_x\text{O}$  due to photocorrosion and electroreduction processes were indeed pre-activation steps for  $\text{CO}_2$  reduction, as discussed in this review for oxide-derived Cu.

## 7. Summary and outlook

As part of the response to the energy crisis and environmental issues, the electrochemical reduction of  $\text{CO}_2$  has attracted increasing attention from researchers. Until now, Cu-based materials remain the most investigated heterogeneous systems for  $\text{CO}_2$  electrolysis due to their distinct advantages for hydrocarbon formation. The high abundance and low cost of Cu will further enable it to become a “star” material in the future.

In this review, the latest progress on Cu-based heterogeneous electrocatalysts for EC  $\text{CO}_2$  reduction was discussed. We summarized the benchmark activity for specific products in Section 3 and various types of Cu-based materials reported by different research groups in Section 4. The  $\text{H}_2$  evolution reaction is inevitable because its equilibrium potential is lower than that of  $\text{CO}_2$  reduction. Apart from engineering the material, therefore, adjusting the electrolyte composition from aqueous to non-aqueous, adding ionic liquid or other additives, and careful pre-treatment of the system are also important. Through the discussions in this review, we hope we could provide useful information to newcomers to the field through detailed information about the experimental conditions, and to those already experienced in the topic through the comparison data in Table 2 and our focus on the more recent literature about Cu-based heterogeneous electrocatalysts (2013–2019).

In summary, the design of efficient and selective Cu-based electrocatalysts is inspiring but still challenging. Several considerations may also be helpful for engineering efficient systems:

(1) PEC  $\text{CO}_2$  reduction with Cu-based materials. Here, we could manipulate two aspects, one of which is energy supply, such as solar energy and other forms of renewable and clean energy for lower applied overpotentials. Optimization of this technique may develop commercially feasible  $\text{CO}_2$  reduction systems. Another aspect to consider is the Cu (photo)cathode. The photocorrosion of copper oxide species is known by many researchers and studies have been done to prolong its stability under irradiation. However, the instability should not be considered a disadvantage when using the copper

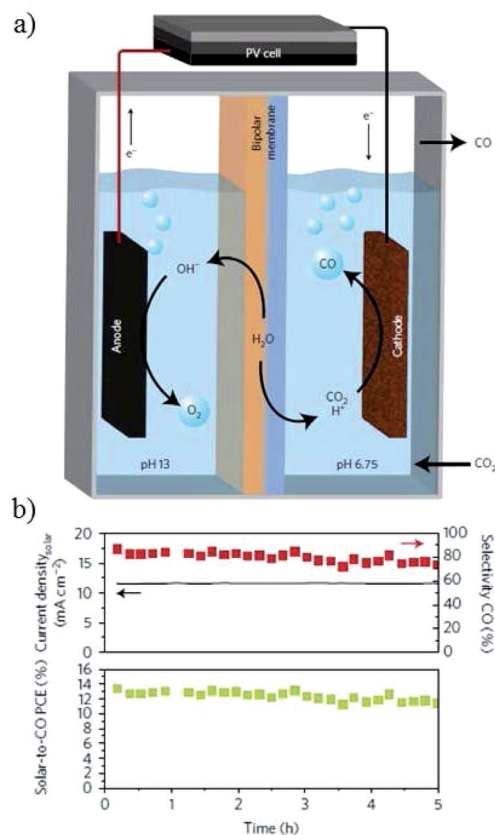


Fig. 33 (a) Schematic of PEC  $\text{CO}_2$  reduction with PV cell. (b) Solar-to-CO conversion efficiency and selectivity of CO *versus* time. Experimental conditions: 0.1 M  $\text{CsHCO}_3$ ||0.25 M  $\text{CsOH}$ ,  $-0.55 \text{ V vs. RHE}$ , PV cell ( $0.5625 \text{ cm}^2$ ,  $100 \text{ mW cm}^{-2}$ , 2.38 V). Reproduced from ref. 61 with permission from Springer Nature, 2017.



oxide species as (photo)cathodes for CO<sub>2</sub> reduction. This is because oxide-derived Cu exhibited better performance than its parent counterpart. Moreover, Cu nanostructures possess localized surface plasmonic (LSPR) effects, which have been used for photocatalytic organic synthesis.<sup>237,238</sup> To the best of our knowledge, there is no report yet for CO<sub>2</sub> reduction utilizing Cu LSPR effects. Future efforts should be made towards this.

(2) Complete systems coupling the reduction of CO<sub>2</sub> and H<sub>2</sub>O oxidation, as well as other significant oxidation reactions. Studying only the half reaction (CO<sub>2</sub> reduction) is not sufficient to achieve a commercially feasible CO<sub>2</sub> reduction system. The performance of anodic reactions also needs to be investigated. It is necessary to explore Cu-based materials as both cathodes and anodes.

(3) Hybrid system of Cu-based materials and metal complexes. Metal molecular catalysts or metal complexes could coordinate CO<sub>2</sub>/intermediates with the metal center and ligands. Covalent-attached metal complexes on Cu-based materials will combine the key features of Cu-based materials and allow molecular-level tunability. This may also address the large overpotential required for the Cu electrode and the instability issue of the molecular catalyst.

(4) 3D Cu porous networks. The pore length and pore size of 3D Cu porous structures will influence the diffusion of reactants and intermediates. Tailoring the pore length as well as the pore size from the macropore to mesopore, micropore, and nanopore region will tune the diffusion and, in turn, the performance of the catalyst. In addition, through designing abundant active sites in this porous network to prolong the retention time of specific intermediates, we could expect high selectivity for specific products.

(5) Cu nanoclusters. Although the size effects of Cu nanoparticles have been discussed widely, ultrasmall, atomically precisely controlled Cu nanoclusters are rarely reported. Similar to Au and Ag nanoclusters,<sup>239</sup> investigating the reaction mechanism to get a fundamental understanding *via* the atomic precise control of Cu nanoclusters is critical to design highly efficient and stable Cu nanocluster electrocatalysts.

(6) Design of the flow cell. The fabrication of an efficient flow cell with a designed gas diffusion electrode (GDE) could dramatically promote the activity and stability of CO<sub>2</sub> electrocatalysts. More and more attention has been paid to this area over the past two years,<sup>103,110,185,208,240</sup> and future efforts could be also made towards this aspect.

Table 2 Summary of Cu-based electrocatalysts for CO<sub>2</sub> reduction<sup>a</sup>

Electrocatalysts	Electrolyte saturated with CO <sub>2</sub> , flow rate of CO <sub>2</sub> gas, and reference electrode used	Faradaic efficiency (FE) and current density for major products, and products distribution	Ref.
All potentials are converted to <i>versus</i> RHE if not specified			
<b>Morphology</b>			
Cu sheet	0.1 M KHCO <sub>3</sub>	CO and HCOO <sup>−</sup> as main products (>−0.6 V); hydrocarbons and alcohols are favorably produced (<−0.7 V)	1989 (ref. 34)
	0.1 M KHCO <sub>3</sub>	29% CH <sub>4</sub> , 30% C <sub>2</sub> H <sub>4</sub> , 7% EtOH, 9% HCOO <sup>−</sup> , 11% H <sub>2</sub> (−0.81 V), current density 5.0 mA cm <sup>−2</sup>	
	0.1 M KClO <sub>4</sub>	10% CH <sub>4</sub> , 48% C <sub>2</sub> H <sub>4</sub> , 16% EtOH, 9% HCOO <sup>−</sup> , 7% H <sub>2</sub> (−0.89 V), current density 5.0 mA cm <sup>−2</sup>	
	0.1 M K <sub>2</sub> HPO <sub>4</sub>	17% CH <sub>4</sub> , 5% HCOO <sup>−</sup> , 72% H <sub>2</sub> (−0.64 V), current density 5.0 mA cm <sup>−2</sup>	
Cycling-derived Cu nanoparticle (50–100 nm) covered Cu foil	0.1 M KClO <sub>4</sub> (pH = 6.0)	Electropolished (smooth): 14% C <sub>2</sub> H <sub>4</sub> and 5% CH <sub>4</sub> (at −1.1 V), LSV onset potential −1.0 V	2012 (ref. 114)
		Nanoparticle covered: 36% C <sub>2</sub> H <sub>4</sub> and 1% CH <sub>4</sub> (at −1.1 V), LSV onset potential −0.6 V	
Cu nanoparticles on glassy carbon plate	0.1 M KHCO <sub>3</sub> , 30 sccm CO <sub>2</sub>	Sputtered: 26% C <sub>2</sub> H <sub>4</sub> and 8% CH <sub>4</sub> (at −1.1 V), LSV onset potential −0.8 V	2014 (ref. 65)
	Ag/AgCl	5–15 nm: 20–25% CO, 60–70% H <sub>2</sub> , 10–15% CH <sub>4</sub> , 0–10% C <sub>2</sub> H <sub>4</sub> (−1.1 V), current density −48 mA cm <sup>−2</sup> for 2 nm Cu foil: 5% CO, 20% H <sub>2</sub> , 57% CH <sub>4</sub> , 20% C <sub>2</sub> H <sub>4</sub> (−1.1 V), current density −23 mA cm <sup>−2</sup>	
Cu nanoparticle spin-coated on glassy carbon (7 nm evolved to 23 nm during reaction)	0.1 M NaHCO <sub>3</sub> , 20 sccm CO <sub>2</sub>	Cu nanoparticle (7–25 nm): 76% CH <sub>4</sub> at −1.35 V with partial current density 9.5 mA cm <sup>−2</sup> , FE onset potential −0.95 V	2014 (ref. 77)
	Ag/AgCl	Cu foil: 44% CH <sub>4</sub> , 35% H <sub>2</sub> (−1.35 V)	
Cu nanoparticles (100 nm) on carbon paper by pulse electrodeposition	0.5 M NaHCO <sub>3</sub> , 1 sccm CO <sub>2</sub>	85% CH <sub>4</sub> at −2.1 V with partial current density 38 mA cm <sup>−2</sup> , FE onset potential −1.1 V	2017 (ref. 115)
	SCE		
	0.1 M KHCO <sub>3</sub> , 20 sccm CO <sub>2</sub>	Amorphous (3.3 nm): 37% HCOOH, 22% C <sub>2</sub> H <sub>5</sub> OH (−0.8 V), partial current density 6 mA cm <sup>−2</sup> , FE onset potential −0.6 V	2018 (ref. 78)





Table 2 (Contd.)

Electrocatalysts	Electrolyte saturated with CO <sub>2</sub> , flow rate of CO <sub>2</sub> gas, and reference electrode used	Faradaic efficiency (FE) and current density for major products, and products distribution All potentials are converted to <i>versus</i> RHE if not specified	Ref.
Amorphous Cu nanoparticles (3.3 nm) on carbon cloth 1 mg/1 × 1 cm <sup>2</sup>	Ag/AgCl (saturated KCl)	Crystalline (3.4 nm): 26% HCOOH (−0.8 V), 6% C <sub>2</sub> H <sub>5</sub> OH (−1.1 V)	2019 (ref. 121)
Cu nanoparticles (2–4 nm)/C on glassy carbon plate	0.1 M KHCO <sub>3</sub> , 20 sccm CO <sub>2</sub>	57% C <sub>2</sub> H <sub>4</sub> at −1.1 V, current density −17.5 mA cm <sup>−2</sup>	
0.2 mg/0.5 cm <sup>2</sup>	Ag/AgCl (3 M NaCl)	70% C <sub>2</sub> H <sub>4</sub> at −1.0 V with partial current density −17.0 mA cm <sup>−2</sup>	2019 (ref. 106)
Branched CuO nanoparticles drop-casted on glass carbon	0.1 M KHCO <sub>3</sub> , 60 sccm CO <sub>2</sub>		
0.2 mg/0.5 cm <sup>2</sup>	Ag/AgCl	63 nm: 63% for carbeneous products: 25% C <sub>2</sub> H <sub>4</sub> , 11% CH <sub>4</sub>	2016 (ref. 129)
Cu nanocubes spin-coated on glassy carbon	0.1 M KHCO <sub>3</sub> , 5 sccm CO <sub>2</sub>		
0.2 mg/2.5 × 2.5 cm <sup>2</sup>	Ag/AgCl	44 nm: 80% for carbeneous products: 41% C <sub>2</sub> H <sub>4</sub> , 20% CH <sub>4</sub> 24 nm: 43% for carbeneous products: 9% C <sub>2</sub> H <sub>4</sub> , 14% CH <sub>4</sub> , 15% HCOO <sup>−</sup> At −1.1 V, current density −0.5, −5.5, −7.5 mA/cm <sub>ECSA</sub> <sup>2</sup> respectively Cu foil: 20% C <sub>2</sub> H <sub>4</sub> , 20% CH <sub>4</sub> , 7% HCOO <sup>−</sup> (−1.1 V)	2014 (ref. 88)
Electrodeposited Cu nanofoam (pore sizes 20–50 μm)	0.1 M KHCO <sub>3</sub> (pH = 6.8)	Major products: HCOOH, H <sub>2</sub> , and CO	
	Ag/AgCl	Minor products (<2%): C <sub>2</sub> H <sub>4</sub> , C <sub>2</sub> H <sub>6</sub> , CH <sub>4</sub> , and C <sub>3</sub> H <sub>6</sub> Not quantified (<1%): CH <sub>3</sub> OH, C <sub>2</sub> H <sub>5</sub> OH The onset potential for HCOOH is −0.4 V; with a FE of 26% at −0.5 V; with a maximum FE of 37% at −0.9 V The FE for smooth copper electrode is <1% at −0.5 V, 25% at −0.9 V Cu main products: C <sub>1</sub> (CO 2% + CH <sub>4</sub> 46%) 48%, C <sub>2</sub> (C <sub>2</sub> H <sub>4</sub> ) 8% at −1.3 V, current density 10 mA cm <sup>−2</sup> , LSV onset potential −0.56 V	2016 (ref. 133)
Cu mesopore (pore size/depth, 300 nm/40 nm, 30 nm/40 nm, 30 nm/70 nm)	0.1 M KHCO <sub>3</sub>		
	Ag/AgCl (3 M KCl)	300 nm/40 nm: C <sub>1</sub> (CO 2% + CH <sub>4</sub> 16%) 18%, C <sub>1</sub> (HCOOH)32%, C <sub>2</sub> (C <sub>2</sub> H <sub>4</sub> )9% 30 nm/40 nm: C <sub>1</sub> (CO 5% + CH <sub>4</sub> 14%)19%, C <sub>2</sub> (C <sub>2</sub> H <sub>4</sub> )38% 30 nm/70 nm: C <sub>1</sub> (CO 8% + CH <sub>4</sub> 6%)14%, C <sub>2</sub> (C <sub>2</sub> H <sub>4</sub> )3%, C <sub>2</sub> (C <sub>2</sub> H <sub>6</sub> )46% At −1.3 V, current density 14.3 mA cm <sup>−2</sup> , LSV onset potential −0.56 V A maximum of C <sub>2</sub> H <sub>4</sub> 40% with partial current density 40 mA cm <sup>−2</sup> and C <sub>2</sub> H <sub>5</sub> OH 20% with partial current density 15 mA cm <sup>−2</sup> at −0.5 V, FE onset potential −0.35 V	2017 (ref. 87)
Nanoporous CuDAT-wire (DAT-3,5-diamino-1,2,4-triazole, additive during electrodeposition) 0.28 mg cm <sup>−2</sup>	1 M KOH (flow cell)		
	Ag/AgCl		2016 (ref. 31)
3D porous hollow fibre Cu (hydrogenation of CuO)	0.3 M KHCO <sub>3</sub> , 20 sccm CO <sub>2</sub>	72% CO at −0.4 V with partial current density 5.6 mA cm <sup>−2</sup> , FE onset potential −0.15 V	
	Ag/AgCl (3 M NaCl)		
<b>Oxide-derived Cu</b>			
Annealed Cu foil (thick Cu <sub>2</sub> O)-derived Cu (≥~3 μm thickness)	0.5 M NaHCO <sub>3</sub> (pH = 7.2), 5 sccm CO <sub>2</sub>	Cu foil: a maximum of CO 20% at −0.8 V, 33% HCOOH at −0.7 to −0.9 V	2012 (ref. 69)
	Ag/AgCl (3 M KCl)	Annealed Cu foil: a peak of CO 45% at −0.3 to −0.5 V, 33% HCOOH at −0.45 to −0.65 V, current density 0.5–7 mA cm <sup>−2</sup> at −0.3 to −0.65 V	
Annealed Cu gauze (CuO nanowire)-derived Cu (size 50–100 nm, length 10–50 μm)	0.1 M KHCO <sub>3</sub> (pH = 6.8), 20 sccm CO <sub>2</sub>	Electrochemical reduction: CO + HCOOH 70–80% at −0.3 to −0.5 V; a peak of CO 61.8% at −0.4 V, HCOOH 30.7% at −0.6 V, current density 0.5–10 mA cm <sup>−2</sup> at −0.3 V to −0.6 V	2015 (ref. 80)
	Ag/AgCl (saturated KCl)	Forming gas reduction: H <sub>2</sub> >90% at −0.3 to −0.5 V, FE onset potential for CO <sub>2</sub> reduction is −0.6 V	



Table 2 (Contd.)

Electrocatalysts	Electrolyte saturated with CO <sub>2</sub> , flow rate of CO <sub>2</sub> gas, and reference electrode used	Faradaic efficiency (FE) and current density for major products, and products distribution	Ref.
Annealed Cu(OH) <sub>2</sub> foil (CuO nanowire)-derived Cu (length 8.1 μm)	0.1 M KHCO <sub>3</sub> (pH = 6.8)	8% C <sub>3</sub> H <sub>7</sub> OH (FE onset potential −0.9 V), 4% C <sub>2</sub> H <sub>5</sub> OH (FE onset potential −0.7 V), 2% C <sub>2</sub> H <sub>6</sub> (FE onset potential −0.7 V), 17% C <sub>2</sub> H <sub>4</sub> , 18% HCOOH, 40% H <sub>2</sub> at −1.1 V	2016 (ref. 134)
	Ag/AgCl (saturated KCl + AgCl)	Cu foil: 3% C <sub>2</sub> H <sub>4</sub> , 12% HCOOH, 80% H <sub>2</sub> at −1.1 V	
Electrodeposited Cu <sub>2</sub> O film on Cu plate	0.1 M KHCO <sub>3</sub> (pH = 6.8), 5 sccm CO <sub>2</sub>	A maximum of C <sub>2</sub> H <sub>4</sub> 33% with partial current density 12 mA cm <sup>−2</sup> , ratio of C <sub>2</sub> H <sub>4</sub> /CH <sub>4</sub> 8–12 (−1.1 V), FE onset potential −0.8 V	2014 (ref. 72)
	Ag/AgCl (3 M NaCl)		
Electrodeposited Cu <sub>2</sub> O film on GDE	0.5 M KHCO <sub>3</sub>	A maximum of C <sub>2</sub> H <sub>4</sub> 26%, ratio of C <sub>2</sub> H <sub>4</sub> /CH <sub>4</sub> up to 26 (−1.2 V), current density 12.5 mA cm <sup>−2</sup>	2015 (ref. 150)
	Ag/AgCl		
Electrodeposited Cu <sub>2</sub> O film (1.7–3.6 μm) on Cu disc	0.1 M KHCO <sub>3</sub> , 20 sccm CO <sub>2</sub>	A maximum of C <sub>2</sub> H <sub>4</sub> 34–39% and C <sub>2</sub> H <sub>5</sub> OH 9–16%, ratio of C <sub>2</sub> H <sub>4</sub> /CH <sub>4</sub> up to 100 (−1.0 V), current density −30 mA cm <sup>−2</sup>	2015 (ref. 81)
	Ag/AgCl (saturated)	Cu <sub>2</sub> O-derived (0.9 μm): 40% C <sub>2</sub> H <sub>4</sub> , 9% C <sub>2</sub> H <sub>5</sub> OH, 8% HCOO <sup>−</sup> (−1.0 V)	
		Cu foil: 9% CO, 14% C <sub>2</sub> H <sub>4</sub> , 13% HCOO <sup>−</sup> (−1.0 V)	
Electrodeposited/oxide-derived Cu nanofoam (pore sizes 50–100 μm)	0.5 M NaHCO <sub>3</sub> (pH = 7.2)	Major products: H <sub>2</sub> , CO, CH <sub>4</sub> , C <sub>2</sub> H <sub>4</sub> , C <sub>2</sub> H <sub>6</sub> , HCOOH	2016 (ref. 131)
	Ag/AgCl (3 M KCl)	Not quantified (<1%): CH <sub>3</sub> OH, C <sub>2</sub> H <sub>5</sub> OH FE HCOOH <6% at any potentials A maximum FE CO of 45% in potentials ranging between −0.6 V and −0.7 V. A maximum of FE C <sub>2</sub> (C <sub>2</sub> H <sub>4</sub> , C <sub>2</sub> H <sub>6</sub> ) 55% at −0.8 V with partial current density 6 mA cm <sup>−2</sup> 20% C <sub>2</sub> H <sub>4</sub> , 35% C <sub>2</sub> H <sub>6</sub> , 15% CO, 6% HCOO <sup>−</sup> , 15% H <sub>2</sub> (−0.8 V) 15% C <sub>2</sub> H <sub>4</sub> , 8% C <sub>2</sub> H <sub>6</sub> , 25% CO, 8% HCOO <sup>−</sup> , 25% H <sub>2</sub> (−0.8 V)–Cu wafer	
Skeleton Cu (annealed, Cu foam electrodeposition)	0.5 M NaHCO <sub>3</sub> (pH = 7.2), 10 sccm CO <sub>2</sub>	Electropolished Cu skeleton: at all potentials from −0.6 V to −1.3 V, CO <3%	2017 (ref. 132)
	Ag/AgCl (3 M KCl)	Annealed Cu skeleton: CO 15% (−0.6 V), a maximum C <sub>2</sub> H <sub>4</sub> + C <sub>2</sub> H <sub>6</sub> 32% (−1.1 V), FE onset for C <sub>2</sub> −0.7 V Electrodeposited Cu foam on Cu skeleton: CO 19% (−0.6 V), a maximum C <sub>2</sub> H <sub>4</sub> + C <sub>2</sub> H <sub>6</sub> 29% (−1.1 V), FE onset for C <sub>2</sub> −0.7 V	
Dendritic Cu (electrodeposition, annealed)	0.5 M KHCO <sub>3</sub> (pH = 7.2), 10 sccm CO <sub>2</sub>	Electrodeposited dendritic Cu : HCOOH 49% (−0.7 V); C <sub>2</sub> H <sub>4</sub> 34% (−1.1 V)	2017 (ref. 156)
	Ag/AgCl (3 M KCl)	Annealed dendritic Cu : C <sub>2</sub> H <sub>5</sub> OH + C <sub>3</sub> H <sub>7</sub> OH 25% (−1.0 V, C <sub>2</sub> H <sub>5</sub> OH 13%) with partial current density 2.8 mA/cm <sub>ECSA</sub> <sup>2</sup> ; C <sub>3</sub> H <sub>7</sub> OH 13% (−0.9 V) with partial current density 0.9 mA/cm <sub>ECSA</sub> <sup>2</sup> ; FE onset potential −0.8 V	
Galvanostatic cycling in Cu <sup>2+</sup> -(Cu <sub>2</sub> O) derived Cu nanocubes on Cu foil	0.25 M KHCO <sub>3</sub> , 50 sccm CO <sub>2</sub>	60% C <sub>2</sub> +(C <sub>2</sub> H <sub>4</sub> , C <sub>2</sub> H <sub>5</sub> OH, <i>n</i> -C <sub>3</sub> H <sub>7</sub> OH) with partial current density 42.5 mA cm <sup>−2</sup> at −0.963 V, FE onset for C <sub>2</sub> −0.705 V and C <sub>3</sub> −0.857 V	2018 (ref. 59)
	SCE		
Hydrothermally prepared Cu <sub>2</sub> O (1.3 and 11.2 μm) on Cu disc	0.1 M KHCO <sub>3</sub> , 20 sccm CO <sub>2</sub>	Cu <sub>2</sub> O derived (1.3 μm): a maximum of C <sub>2</sub> H <sub>4</sub> 27% (−1.0 V), C <sub>2</sub> H <sub>6</sub> <3% (−0.5 to −1.1 V)	2017 (ref. 146)
	Ag/AgCl (saturated)	Cu <sub>2</sub> O derived (11.2 μm): a maximum of C <sub>2</sub> H <sub>4</sub> 15% (−0.8 V), C <sub>2</sub> H <sub>6</sub> 8% (−0.8 V) with FE onset −0.6 V, current density 20 mA cm <sup>−2</sup> CuO derived (11.5 μm): a maximum of C <sub>2</sub> H <sub>4</sub> 13% (−0.8 V), C <sub>2</sub> H <sub>6</sub> 11% (−0.8 V) with FE onset −0.6 V, current density 20 mA cm <sup>−2</sup>	
Plasma-treated Cu foil	0.1 M KHCO <sub>3</sub> , 30 sccm CO <sub>2</sub>	Cu foil: C <sub>2</sub> H <sub>4</sub> 30% at −0.9 V, FE onset potential −0.85 V	2016 (ref. 95)
	Ag/AgCl	O <sub>2</sub> plasma activated Cu : C <sub>2</sub> H <sub>4</sub> 60% (−0.9 V, FE onset potential −0.5 V)	
Plasma-treated Cl <sup>−</sup> -induced Cu <sub>2</sub> O–Cu nanocube	0.1 M KHCO <sub>3</sub> , 20 sccm CO <sub>2</sub>	C <sub>2</sub> + C <sub>3</sub> 73% at −1.0 V C <sub>2</sub> H <sub>4</sub> 45%, C <sub>2</sub> H <sub>5</sub> OH 20%, <i>n</i> -C <sub>3</sub> H <sub>7</sub> OH 9%, current density 37 mA cm <sup>−2</sup> at −1.0 V	2017 (ref. 149)
	Ag/AgCl		
Cl <sup>−</sup> -induced Cu <sub>2</sub> O–Cu	0.1 M KCl (catholyte), 0.1 M KHCO <sub>3</sub> (anolyte)	From Cu <sub>2</sub> O: 46% C <sub>2</sub> (22% C <sub>2</sub> H <sub>4</sub> and 24% C <sub>2</sub> H <sub>5</sub> OH), 10% C <sub>3</sub> –C <sub>4</sub> (9% C <sub>3</sub> H <sub>7</sub> OH, 1% C <sub>4</sub> H <sub>10</sub> ) at −1.6 V, FE onset for C <sub>2</sub> −0.6 V and C <sub>3</sub> –C <sub>4</sub> −1.0 V	2015 (ref. 160)
	Ag/AgCl (3 M KCl)	From Cu: 18% C <sub>2</sub> H <sub>4</sub> , 6% C <sub>2</sub> H <sub>5</sub> OH, 25% CH <sub>4</sub> at −1.6 V	



Table 2 (Contd.)

Electrocatalysts	Electrolyte saturated with CO <sub>2</sub> , flow rate of CO <sub>2</sub> gas, and reference electrode used	Faradaic efficiency (FE) and current density for major products, and products distribution All potentials are converted to <i>versus</i> RHE if not specified	Ref.
Halide-induced Cu <sub>2</sub> O–Cu	0.1 M KHCO <sub>3</sub> (pH = 6.8), 5 sccm CO <sub>2</sub> Ag/AgCl (saturated KCl)	Cycling Cu foil in halide: 16% C <sub>2</sub> H <sub>4</sub> , 8% C <sub>2</sub> H <sub>5</sub> OH at –1.0 V, current density 12 mA cm <sup>–2</sup> , FE onset for C <sub>2</sub> H <sub>5</sub> OH –0.6 V and C <sub>2</sub> H <sub>4</sub> –0.8 V Cu foil: 9% C <sub>2</sub> H <sub>4</sub> , 3% C <sub>2</sub> H <sub>5</sub> OH at –1.0 V	2016 (ref. 142)
Cl <sup>–</sup> -induced Cu <sub>2</sub> <sup>18</sup> O–Cu on Si (1 μm)	0.1 M KHCO <sub>3</sub> , 5 sccm CO <sub>2</sub> Ag/AgCl	Cycling Cu foil in KCl : C <sub>2</sub> /C <sub>3</sub> 60% (C <sub>2</sub> H <sub>4</sub> 34% with partial current density –7.5 mA cm <sup>–2</sup> ), C <sub>1</sub> 6.5% at –1.0 V, current density –10.9 mA cm <sup>–2</sup> Cu foil: C <sub>2</sub> /C <sub>3</sub> 37%, C <sub>1</sub> 25% at –1.0 V, current density 6.9 mA cm <sup>–2</sup>	2017 (ref. 143)
Cu <sub>2</sub> (OH) <sub>3</sub> Cl-induced Cu <sub>2</sub> O–Cu nanoneedle on carbon paper (electrodeposited/oxide-derived)	0.1 M KHCO <sub>3</sub> , 20 sccm CO <sub>2</sub> Ag/AgCl (saturated KCl)	54% C <sub>2</sub> +(C <sub>2</sub> H <sub>4</sub> , CH <sub>3</sub> COOH, C <sub>2</sub> H <sub>5</sub> OH), 18% C <sub>1</sub> + (CH <sub>4</sub> , CO, HCOOH), C <sub>2</sub> H <sub>4</sub> /CH <sub>4</sub> = 130 at –1.2 V with a C <sub>2</sub> H <sub>4</sub> partial current density 22 mA cm <sup>–2</sup> , FE onset potential –0.7 V Flow cell: C <sub>2</sub> H <sub>4</sub> /CH <sub>4</sub> = 200 at –1.0 V with a C <sub>2</sub> H <sub>4</sub> partial current density 160 mA cm <sup>–2</sup>	2018 (ref. 82)
<b>Surface modification</b> Amino acid-modified Cu(OH) <sub>2</sub> nanowire derived Cu (diameter 100–200 nm, length tens of μm)	0.1 M KHCO <sub>3</sub> Ag/AgCl (saturated KCl)	Amino acid modified Cu nanowire: 13% C <sub>2</sub> H <sub>4</sub> , 21% C <sub>2</sub> H <sub>6</sub> , 52H <sub>2</sub> % (–1.3 V), with partial current density for C <sub>x</sub> H <sub>y</sub> 3 mA cm <sup>–2</sup> Cu nanowire: 6% C <sub>2</sub> H <sub>4</sub> , 12% C <sub>2</sub> H <sub>6</sub> , 76H <sub>2</sub> % (–1.3 V)	2016 (ref. 182)
Pd atoms-modified Cu mesh	0.5 M KHCO <sub>3</sub> , 20 sccm CO <sub>2</sub> Ag/AgCl	Cu: after 4 h, H <sub>2</sub> (100%) at –0.96 V Pd-decorated Cu: initial and after 4 h, H <sub>2</sub> (40%), 50% (CH <sub>4</sub> + C <sub>2</sub> H <sub>4</sub> ) at –0.96 V, current density 50 mA cm <sup>–2</sup>	2017 (ref. 60)
SnO-modified CuO nanowire	0.1 M NaHCO <sub>3</sub> (pH = 6.75), 10 sccm CO <sub>2</sub> Ag/AgCl (saturated KCl)	CuO nanowire: 36% CO with a partial current density –0.25 mA cm <sup>–2</sup> at –0.7 V SnO <sub>2</sub> -modified CuO nanowire: 97% CO with a partial current density –1.1 mA cm <sup>–2</sup> at –0.7 V	2017 (ref. 61)
<b>Bimetallic species</b> Dendritic Cu–In electrode (dendrite tips of ~50 nm width)	0.1 M KHCO <sub>3</sub> Ag/AgCl	Pure dendritic Cu: at all potentials from –0.8 V to –1.1 V, HCOOH <10% Pure In: a maximum of HCOOH 40% at –1.0 V Cu–in alloy: At –0.8 and –0.9 V, HCOOH 60% (60 or 80 at% In) At –1.0 V, 50% HCOOH and the ratio of H <sub>2</sub> : CO <sub>2</sub> is 2.6 : 1(40 at% In); a maximum of HCOOH 62% (80 at% In)	2017 (ref. 166)
Cu–In alloy ( <i>in situ</i> reduction of annealed/oxide-derived Cu in In solution)	0.1 M KHCO <sub>3</sub> , 10 sccm CO <sub>2</sub> Ag/AgCl (saturated KCl)	Oxide-derived Cu: a maximum of CO (40%) at –0.6 V, current density –1.7 mA cm <sup>–2</sup> , FE onset potential –0.3 V Cu–in alloy: 95% CO at –0.7 V, current density –1.7 mA cm <sup>–2</sup> , FE onset potential –0.3 V	2015 (ref. 73)
Cu–Sn alloy ( <i>in situ</i> reduction of oxide-derived Cu in Sn solution)	0.1 M KHCO <sub>3</sub> , 10 sccm CO <sub>2</sub> Ag/AgCl (saturated KCl)	>80% CO at –0.4 to –0.8 V, 90% CO with current density at –0.6 V A maximum of C <sub>2</sub> H <sub>5</sub> OH 29% at –1.05 V with partial current density –8 mA cm <sup>–2</sup> , FE onset potential –0.95 V	2016 (ref. 74)
Electrodeposited Cu <sub>x</sub> Zn oxides film	0.1 M KHCO <sub>3</sub> , 20 sccm CO <sub>2</sub> Ag/AgCl (saturated)	Au: 60% CO with a partial current –180 mA mg <sup>–1</sup> at –0.73 V, current density 2.6 mA cm <sup>–2</sup>	2016 (ref. 84)
Au <sub>x</sub> Cu <sub>y</sub> alloy nanoparticles assembled on glassy carbon	0.1 M KHCO <sub>3</sub> , 30 sccm CO <sub>2</sub> Ag/AgCl (1 M KCl)	Au <sub>3</sub> Cu: 67% CO with a partial current –230 mA mg <sup>–1</sup> at –0.73 V, current density 2.6 mA cm <sup>–2</sup>	2014 (ref. 172)





Table 2 (Contd.)

Electrocatalysts	Electrolyte saturated with CO <sub>2</sub> , flow rate of CO <sub>2</sub> gas, and reference electrode used	Faradaic efficiency (FE) and current density for major products, and products distribution	Ref.
		All potentials are converted to <i>versus</i> RHE if not specified	
Ag–Cu alloy (Ag–Cu <sub>2</sub> O derived)	0.2 M KCl (catholyte) 0.1 M KHCO <sub>3</sub> (anolyte) Ag/AgCl	AuCu <sub>3</sub> : 15% CO with a partial current density 1.4 mA cm <sup>−2</sup> Cu: 2–3% CO with a partial current density 0.7 mA cm <sup>−2</sup>	
Electrodeposited Cu–Ag alloy on carbon paper (GDL) with the addition of 3,5-diamino-1,2,4-triazole	1 M KOH, 7 sccm CO <sub>2</sub> Ag/AgCl	Phase-separated Ag–Cu <sub>2</sub> O: 20% C <sub>2</sub> H <sub>5</sub> OH at −1.2 V, FE onset potential −1.0 V Phase blended Ag–Cu <sub>2</sub> O: 34% C <sub>2</sub> H <sub>5</sub> OH at −1.2 V, FE onset potential −0.9 V Pure Cu <sub>2</sub> O: 11% C <sub>2</sub> H <sub>5</sub> OH, FE onset potential −1.0 V 6% Ag in CuAg alloy: 60% C <sub>2</sub> H <sub>4</sub> with a partial current density −180 mA cm <sup>−2</sup> and 25% C <sub>2</sub> H <sub>5</sub> OH with a partial current density −90 mA cm <sup>−2</sup> at −0.7 V	2017 (ref. 177) 2018 (ref. 102)
Electrodeposited Cu–Ag alloy (~6 nm) on polymer on glassy carbon	0 °C, 0.5 M KHCO <sub>3</sub> (8 ppm benzotriazole) SCE	21% CH <sub>3</sub> COO <sup>−</sup> at −1.33 V, FE onset potential −1.1 V	2018 (ref. 170)
Electrodeposited Cu–Pd alloy (~6.6 nm) on polymer on FTO	0.1 M TBAPF <sub>6</sub> /CH <sub>3</sub> CN (1 M H <sub>2</sub> O), Ag/AgNO <sub>3</sub> ; 0.1 M KHCO <sub>3</sub> , SCE	Cu <sub>2</sub> Pd: 51% CH <sub>4</sub> at with an overpotential 0.86 V, current density −6.0 mA cm <sup>−2</sup>	2015 (ref. 169)
Electrodeposited Cu–Pd alloy on glassy carbon	0.1 M KHCO <sub>3</sub> Ag/AgCl (saturated KCl)	Pd <sub>7</sub> Cu <sub>3</sub> 80% CO at −0.8 V, current density −1.0 mA cm <sup>−2</sup> , FE onset potential −0.7 V	2016 (ref. 173)
Cu–Pd alloy nanoparticles on Vulcan carbon coated on carbon paper 2 mg/1 × 2 cm <sup>2</sup>	0.1 M KHCO <sub>3</sub> Ag/AgCl	Pd <sub>85</sub> Cu <sub>15</sub> , 86% CO with a partial current density −6.9 mA cm <sup>−2</sup> at −0.9 V, FE onset potential −0.6 V	2016 (ref. 174)
Cu–Pd alloy nanoparticles on GDE 4 mg/5.0 × 0.8 cm <sup>2</sup>	0.1 M KOH, 7 sccm CO <sub>2</sub> , electrolyte flow rate 0.5 sccm at −2 V to −3.5 V and 0.1 sccm at −1.6 V to −2 V vs. Ag/AgCl	Phase-separated CuPd: 48% C <sub>2</sub> H <sub>4</sub> , 15% C <sub>2</sub> H <sub>5</sub> OH, 15% CO at −0.7 V, FE C <sub>2</sub> H <sub>4</sub> onset −0.4 V, FE C <sub>2</sub> H <sub>5</sub> OH onset −0.5 V	2016 (ref. 86)
Cu–Pd alloy nanoparticles on Vulcan carbon coated on carbon paper 1 mg cm <sup>−2</sup>	0.1 M KHCO <sub>3</sub> , 10 sccm CO <sub>2</sub> , Ag/AgCl (saturated KCl)	Disordered CuPd: 12% C <sub>2</sub> H <sub>4</sub> , 5% C <sub>2</sub> H <sub>5</sub> OH, 50% CO, 4% CH <sub>4</sub> at −0.7 V, FE C <sub>2</sub> H <sub>4</sub> onset −0.6 V, FE C <sub>2</sub> H <sub>5</sub> OH onset −0.6 V Ordered CuPd: 75% CO, 2% CH <sub>4</sub> at −0.7 V, FE C <sub>2</sub> H <sub>4</sub> onset −0.7 V, FE C <sub>2</sub> H <sub>5</sub> OH onset −0.9 V 87% CO at −0.9 V with partial current density 30 mA mg <sup>−1</sup> (30 mA cm <sup>−2</sup> )	2019 (ref. 241)
<b>Aqueous electrolyte</b>			
Cu foil	0.1 M MHCO <sub>3</sub> (M = Li, Na, K, Rb, Cs, pH = 6.8), 5 sccm CO <sub>2</sub> Ag/AgCl (saturated KCl)	C <sub>2</sub> H <sub>4</sub> /CH <sub>4</sub> (Li <sup>+</sup> 0.2, Na <sup>+</sup> 0.3, K <sup>+</sup> 0.7, Rb <sup>+</sup> 1.8, Cs <sup>+</sup> 3.3), H <sub>2</sub> (Li <sup>+</sup> 85.9%, Na <sup>+</sup> 66.3%, K <sup>+</sup> 55.1%, Rb <sup>+</sup> 32.2%, Cs <sup>+</sup> 31.1%) C <sub>2</sub> H <sub>5</sub> OH (Rb <sup>+</sup> 9.6%, Cs <sup>+</sup> 11.4%) −1.0 V, current density increased from 2.5 mA cm <sup>−2</sup> to 5.5 mA cm <sup>−2</sup> with the increase of cation size	2016 (ref. 188)
Cu foil	0.1 M KHCO <sub>3</sub> , 30 sccm CO <sub>2</sub> 0.3 M KBr + 0.1 M KHCO <sub>3</sub> , 30 sccm CO <sub>2</sub> 0.3 M KI + 0.1 M KHCO <sub>3</sub> , 30 sccm CO <sub>2</sub>	15% CH <sub>4</sub> , 10% C <sub>2</sub> H <sub>4</sub> , 8% CO, 22% HCOO <sup>−</sup> , 40% H <sub>2</sub> (−0.95 V), current density 2.5 mA cm <sup>−2</sup> 5% CH <sub>4</sub> , 7% C <sub>2</sub> H <sub>4</sub> , 27% CO, 18% HCOO <sup>−</sup> , 40% H <sub>2</sub> (−0.95 V), current density 2.5 mA cm <sup>−2</sup> 41% CH <sub>4</sub> , 17% C <sub>2</sub> H <sub>4</sub> , 5% CO, 10% HCOO <sup>−</sup> , 30% H <sub>2</sub> (−0.95 V), current density 9.5 mA cm <sup>−2</sup>	2016 (ref. 191)



Table 2 (Contd.)

Electrocatalysts	Electrolyte saturated with CO <sub>2</sub> , flow rate of CO <sub>2</sub> gas, and reference electrode used	Faradaic efficiency (FE) and current density for major products, and products distribution All potentials are converted to <i>versus</i> RHE if not specified	Ref.
<b>Non-aqueous electrolyte</b>			
Cu–Cu <sub>2</sub> O–[Cu(cyclam)](ClO <sub>4</sub> ) <sub>2</sub> composite on FTO	0.1 M <i>n</i> -Bu <sub>4</sub> BF <sub>4</sub> in DMF/H <sub>2</sub> O (97 : 3 v/v)	90% HCOO <sup>−</sup> at −2.0 V <i>vs.</i> Fc <sup>+</sup> /Fc, current density −1.15 mA cm <sup>−2</sup>	2015 (ref. 196)
Electrodeposited Cu <sub>2</sub> O on FTO	Ag/AgCl (3 M KCl) 0.1 M <i>n</i> -Bu <sub>4</sub> BF <sub>4</sub> in DMF/H <sub>2</sub> O (99 : 1 v/v)	90% HCOO <sup>−</sup> at −2.0 V <i>vs.</i> Fc <sup>+</sup> /Fc, current density −1.5 mA cm <sup>−2</sup>	2016 (ref. 197)
Cu foil	Ag/AgCl (3 M KCl) 0.1 M supporting electrolyte in MeCN Ag/Ag <sup>+</sup> (0.1 M AgClO <sub>4</sub> in MeCN)	CO, carbonate, bicarbonate as main products	2016 (ref. 198)
Porous dendritic Cu nanofoam (pore size 30–40 μm, 10 wt% Cu <sub>2</sub> O) on Cu plate	Ionic liquid [EMIM](BF <sub>4</sub> )/H <sub>2</sub> O (98 : 2 v/v)	Porous dendritic Cu: 83% HCOO <sup>−</sup> at −1.55 V <i>vs.</i> Fc <sup>+</sup> /Fc, current density −5.0 mA cm <sup>−2</sup>	2017 (ref. 206)
Phosphate modified dendritic Cu	Ag/AgCl (3 M KCl) 0.1 M supporting electrolyte in MeCN Ag/Ag <sup>+</sup> (0.1 M AgNO <sub>3</sub> in MeCN)	Cu foil: 45% HCOO <sup>−</sup> at −1.55 V <i>vs.</i> Fc <sup>+</sup> /Fc 81% HCOO <sup>−</sup> at −1.45 V <i>vs.</i> NHE, current density −1.35 mA cm <sup>−2</sup>	2017 (ref. 199)
<b>PEC</b>			
Cu <sub>2</sub> O nanocrystal/CuO nanorod (photocathode)  Pt (anode)	0.1 M Na <sub>2</sub> SO <sub>4</sub> , simulated AM 1.5 illumination (70 mW cm <sup>−2</sup> )	95% CH <sub>3</sub> OH, +0.17 V bias potential, photocurrent density 0.2 mA cm <sup>−2</sup>	2013 (ref. 218)
Cu <sub>2</sub> O/AZO/TiO <sub>2</sub> (photocathode)  Pt (anode)	MeCN, 0.1 M Bu <sub>4</sub> NPF <sub>6</sub> , under filtered 450 W Xe arc lamp (1 sun) Ag/AgCl wire	80–95% CO at −1.9 V <i>vs.</i> Fc <sup>+</sup> /Fc, photocurrent density 2.5 mA cm <sup>−2</sup>	2016 (ref. 229)
CuFeO <sub>2</sub> /CuO (photocathode)  Pt (anode)	0.1 M NaHCO <sub>3</sub> + KPi, white-light LED illumination (100 mW cm <sup>−2</sup> )	80% CH <sub>3</sub> COO <sup>−</sup> , +0.2 V bias potential, photocurrent density 0.15 mA cm <sup>−2</sup>	2017 (ref. 220)
Cu (cathode)  WO <sub>3</sub> (photoanode)	0.5 M KHCO <sub>3</sub> (pH = 7.5), visible light (>420 nm) using a 500 W Hg lamp	71.6% carbonic product (65% CH <sub>4</sub> ), +0.65 V bias potential, photocurrent density 0.25 mA cm <sup>−2</sup>	2014 (ref. 222)
Cu <sub>2</sub> O (cathode)  TiO <sub>2</sub> (photoanode)	0.1 M KHCO <sub>3</sub> (pH = 6.9), AM 1.5G illumination (100 mW cm <sup>−2</sup> )	92.6% carbonic products (54% CH <sub>4</sub> , 30% CO, 3% CH <sub>3</sub> OH), +0.75 V bias potential, photocurrent density 1.34 mA cm <sup>−2</sup>	2016 (ref. 225)
Cu–Zn alloy (cathode)  SrTiO <sub>3</sub> (photoanode)	0.1 M KHCO <sub>3</sub> (pH = 6.8), 0.1 M KCl + 0.01 M NaOH (anolyte), UV light Hg–Xe lamp (240–300 nm)	79% HCOO <sup>−</sup> without bias potential	2017 (ref. 223)
Cu (cathode)  BiVO <sub>4</sub> (photoanode)	0.5 M NaCl, 300 W Xe arc lamp with AM 1.5G filter (100 mW cm <sup>−2</sup> )	65.4% HCOO <sup>−</sup> at 0.75 V bias potential, photocurrent density 0.1 mA cm <sup>−2</sup> ; 85.1% HCHO at 0.9 V bias potential, photocurrent density 0.35 mA cm <sup>−2</sup> ; 6.89% CH <sub>3</sub> OH and 4.4% C <sub>2</sub> H <sub>5</sub> OH at 1.35 V bias potential, photocurrent density 0.75 mA cm <sup>−2</sup>	2018 (ref. 224)
PV cell (GaInP/GaInAs/Ge)–CuO@SnO <sub>2</sub> (cathode and anode)	0.1 M CsHCO <sub>3</sub> (pH = 6.75, catholyte)  0.25 M CsOH (pH = 13.3, anolyte), AM 1.5G illumination (100 mW cm <sup>−2</sup> ) and a voltage of 2.38 V	13.4% solar to CO efficiency at +0.55 V, photocurrent density 12 mA cm <sup>−2</sup>	2017 (ref. 61)

<sup>a</sup> The potential applied for EC CO<sub>2</sub> reduction *versus* RHE is calculated according to the equation  $E$  (*vs.* RHE) =  $E^0$  (*vs.* Ag/AgCl) +  $E$  (*vs.* Ag/AgCl) + 0.0591pH −  $\eta$ (IR<sub>drop</sub>) in aqueous solution.  $E^0$  (*vs.* Ag/AgCl) = 0.21 V, 0.197 V, and 0.21 V for 3 M KCl, saturated KCl, and 3 M NaCl, respectively.



## Conflicts of interest

There are no conflicts to declare.

## Acknowledgements

Financial support of this work by the National Science Foundation of China (NSFC, 21703154) and the Natural Science Foundation of Tianjin (18JCYBJC43100) is gratefully acknowledged. X. K. thanks the EPSRC (EP/S025537/1) for financial support.

## Notes and references

- Z. W. Seh, J. Kibsgaard, C. F. Dickens, I. Chorkendorff, J. K. Nørskov and T. F. Jaramillo, *Science*, 2017, **355**.
- E. V. Kondratenko, G. Mul, J. Baltrusaitis, G. O. Larrazábal and J. Pérez-Ramírez, *Energy Environ. Sci.*, 2013, **6**, 3112–3135.
- R. J. Lim, M. Xie, M. A. Sk, J.-M. Lee, A. Fisher, X. Wang and K. H. Lim, *Catal. Today*, 2013.
- A. M. Appel, J. E. Bercaw, A. B. Bocarsly, H. Dobbek, D. L. Dubois, M. Dupuis, J. G. Ferry, E. Fujita, R. Hille, P. J. Kenis, C. A. Kerfeld, R. H. Morris, C. H. Peden, A. R. Portis, S. W. Ragsdale, T. B. Rauchfuss, J. N. Reek, L. C. Seefeldt, R. K. Thauer and G. L. Waldrop, *Chem. Rev.*, 2013, **113**, 6621–6658.
- Q. W. Song, Z. H. Zhou and L. N. He, *Green Chem.*, 2017, **19**, 3707–3728.
- F. Studt, I. Sharafutdinov, F. Abild-Pedersen, C. F. Elkjær, J. S. Hummelshøj, S. Dahl, I. Chorkendorff and J. K. Nørskov, *Nat. Chem.*, 2014, **6**, 320–324.
- S. Kattel, P. Liu and J. G. Chen, *J. Am. Chem. Soc.*, 2017, **139**, 9739–9754.
- M. Bersani, K. Gupta, A. K. Mishra, R. Lanza, S. F. R. Taylor, H. U. Islam, N. Hollingsworth, C. Hardacre, N. H. de Leeuw and J. A. Darr, *ACS Catal.*, 2016, **6**, 5823–5833.
- B. Rungtaweeworani, J. Baek, J. R. Araujo, B. S. Archanjo, K. M. Choi, O. M. Yaghi and G. A. Somorjai, *Nano Lett.*, 2016, **16**, 7645–7649.
- B. Yang, C. Liu, A. Halder, E. C. Tyo, A. B. F. Martinson, S. Seifert, P. Zapol, L. A. Curtiss and S. Vajda, *J. Phys. Chem. C*, 2017, **121**, 10406–10412.
- K. Kobl, S. Thomas, Y. Zimmermann, K. Parkhomenko and A. C. Roger, *Catal. Today*, 2016, **270**, 31–42.
- W. Tu, Y. Zhou and Z. Zou, *Adv. Mater.*, 2014, **26**, 4607–4626.
- S. C. Roy, O. K. Varghese, M. Paulose and C. A. Grimes, *ACS Nano*, 2010, **4**, 1259–1278.
- J. Ran, M. Jaroniec and S. Z. Qiao, *Adv. Mater.*, 2018, **30**, 1704649.
- D. Gao, F. Cai, G. Wang and X. Bao, *Curr. Opin. Green Sustain. Chem.*, 2017, **3**, 39–44.
- B. Khezri, A. C. Fisher and M. Pumera, *J. Mater. Chem. A*, 2017, **5**, 8230–8246.
- Q. Lu, J. Rosen and F. Jiao, *ChemCatChem*, 2015, **7**, 38–47.
- T. Ma, Q. Fan, H. Tao, Z. Han, M. Jia, Y. Gao, W. Ma and Z. Sun, *Nanotechnology*, 2017, **28**, 472001.
- L. Shi, G. H. Yang, K. Tao, Y. Yoneyama, Y. S. Tan and N. Tsubaki, *Acc. Chem. Res.*, 2013, **46**, 1838–1847.
- L. Wang, Y. Yi, C. Wu, H. Guo and X. Tu, *Angew. Chem., Int. Ed.*, 2017, **56**, 13679–13683.
- Z. L. Wang, C. Li and Y. Yamauchi, *Nano Today*, 2016, **11**, 373–391.
- W. Zhang, Y. Hu, L. Ma, G. Zhu, Y. Wang, X. Xue, R. Chen, S. Yang and Z. Jin, *Adv. Sci.*, 2018, **5**, 1700275.
- J. Qiao, Y. Liu, F. Hong and J. Zhang, *Chem. Soc. Rev.*, 2014, **43**, 631–675.
- R. Kas, R. Kortlever, H. Yilmaz, M. T. M. Koper and G. Mul, *ChemElectroChem*, 2015, **2**, 354–358.
- A. S. Varela, M. Kroschel, T. Reier and P. Strasser, *Catal. Today*, 2016, **260**, 8–13.
- K. J. P. Schouten, E. Pérez Gallent and M. T. M. Koper, *J. Electroanal. Chem.*, 2014, **716**, 53–57.
- A. Wuttig, C. Liu, Q. Peng, M. Yaguchi, C. H. Hendon, K. Motobayashi, S. Ye, M. Osawa and Y. Surendranath, *ACS Cent. Sci.*, 2016, **2**, 522–528.
- M. R. Singh, E. L. Clark and A. T. Bell, *Phys. Chem. Chem. Phys.*, 2015, **17**, 18924–18936.
- D. Ren, J. Fong and B. S. Yeo, *Nat. Commun.*, 2018, **9**, 925.
- K. Hara, A. Tsuneto, A. Kudo and T. Sakata, *J. Electrochem. Soc.*, 1994, **141**, 2097–2103.
- R. Kas, K. K. Hummadi, R. Kortlever, P. de Wit, A. Milbrat, M. W. Luiten-Olieman, N. E. Benes, M. T. Koper and G. Mul, *Nat. Commun.*, 2016, **7**, 10748.
- D. W. DeWulf, T. Jin and A. J. Bard, *J. Electrochem. Soc.*, 1989, **136**, 1686–1691.
- S. T. Ahn, I. Abu-Baker and G. T. R. Palmore, *Catal. Today*, 2017, **288**, 24–29.
- Y. Hori, A. Murata and R. Takahashi, *J. Chem. Soc., Faraday Trans. 1*, 1989, **85**, 2309–2326.
- Y. Hori, H. Wakebe, T. Tsukamoto and O. Koga, *Electrochim. Acta*, 1994, **39**, 1833–1839.
- R. Daiyan, X. Lu, Y. H. Ng and R. Amal, *ChemSusChem*, 2017, **10**, 4342–4358.
- M. Gattrell, N. Gupta and A. Co, *J. Electroanal. Chem.*, 2006, **594**, 1–19.
- S. Lee and J. Lee, *ChemSusChem*, 2016, **9**, 333–344.
- M. R. Dubois and D. L. Dubois, *Acc. Chem. Res.*, 2009, **42**, 1974–1982.
- A. J. Morris, G. J. Meyer and E. Fujita, *Acc. Chem. Res.*, 2009, **42**, 1983–1994.
- J. M. Savéant, *Chem. Rev.*, 2008, **108**, 2348–2378.
- C. Costentin, M. Robert and J. M. Savéant, *Chem. Soc. Rev.*, 2013, **42**, 2423–2436.
- P. Kang, Z. Chen, M. Brookhart and T. J. Meyer, *Top. Catal.*, 2015, **58**, 30–45.
- R. Angamuthu, P. Byers, M. Lutz, A. L. Spek and E. Bouwman, *Science*, 2010, **327**, 313–315.
- Z. Weng, J. Jiang, Y. Wu, Z. Wu, X. Guo, K. L. Materna, W. Liu, V. S. Batista, G. W. Brudvig and H. Wang, *J. Am. Chem. Soc.*, 2016, **138**, 8076–8079.
- Z. Weng, Y. Wu, M. Wang, J. Jiang, K. Yang, S. Huo, X. F. Wang, Q. Ma, G. W. Brudvig, V. S. Batista, Y. Liang, Z. Feng and H. Wang, *Nat. Commun.*, 2018, **9**, 415.





- 47 A. Hicken, A. J. P. White and M. R. Crimmin, *Angew. Chem., Int. Ed.*, 2017, **56**, 15127–15130.
- 48 C. M. Zall, J. C. Linehan and A. M. Appel, *J. Am. Chem. Soc.*, 2016, **138**, 9968–9977.
- 49 Q. Tang, Y. Lee, D. Y. Li, W. Choi, C. W. Liu, D. Lee and D. E. Jiang, *J. Am. Chem. Soc.*, 2017, **139**, 9728–9736.
- 50 T. Ikuno, J. Zheng, A. Vjunov, M. Sanchez-Sanchez, M. A. Ortuno, D. R. Pahls, J. L. Fulton, D. M. Camaioni, Z. Li, D. Ray, B. L. Mehdi, N. D. Browning, O. K. Farha, J. T. Hupp, C. J. Cramer, L. Gagliardi and J. A. Lercher, *J. Am. Chem. Soc.*, 2017, **139**, 10294–10301.
- 51 J. Albo, D. Vallejo, G. Beobide, O. Castillo, P. Castaço and A. Irabien, *ChemSusChem*, 2017, **10**, 1100–1109.
- 52 H. Xie, J. Wang, K. Ithisuphalap, G. Wu and Q. Li, *J. Energy Chem.*, 2017, **26**, 1039–1049.
- 53 H. Xie, T. Y. Wang, J. S. Liang, Q. Li and S. H. Sun, *Nano Today*, 2018, **21**, 41–54.
- 54 C. W. Lee, K. D. Yang, D. H. Nam, J. H. Jang, N. H. Cho, S. W. Im and K. T. Nam, *Adv. Mater.*, 2018, **30**, 1704717.
- 55 S. Nitopi, E. Bertheussen, S. B. Scott, X. Liu, A. K. Engstfeld, S. Horch, B. Seger, I. E. L. Stephens, K. Chan, C. Hahn, J. K. Nørskov, T. F. Jaramillo and I. Chorkendorff, *Chem. Rev.*, 2019, **119**, 7610–7672.
- 56 Y. Hori, H. Konishi, T. Futamura, A. Murata, O. Koga, H. Sakurai and K. Oguma, *Electrochim. Acta*, 2005, **50**, 5354–5369.
- 57 Y. Lum, Y. Kwon, P. Lobaccaro, L. Chen, E. L. Clark, A. T. Bell and J. W. Ager, *ACS Catal.*, 2016, **6**, 202–209.
- 58 J. T. Billy and A. C. Co, *ACS Catal.*, 2017, **7**, 8467–8479.
- 59 K. Jiang, R. B. Sandberg, A. J. Akey, X. Liu, D. C. Bell, J. K. Nørskov, K. Chan and H. Wang, *Nat. Catal.*, 2018, **1**, 111–119.
- 60 Z. Weng, X. Zhang, Y. Wu, S. Huo, J. Jiang, W. Liu, G. He, Y. Liang and H. Wang, *Angew. Chem., Int. Ed.*, 2017, **56**, 13135–13139.
- 61 M. Schreier, F. Héroguel, L. Steier, S. Ahmad, J. S. Luterbacher, M. T. Mayer, J. Luo and M. Grätzel, *Nat. Energy*, 2017, **2**, 17087.
- 62 A. Wuttig and Y. Surendranath, *ACS Catal.*, 2015, **5**, 4479–4484.
- 63 E. L. Clark, C. Hahn, T. F. Jaramillo and A. T. Bell, *J. Am. Chem. Soc.*, 2017, **139**, 15848–15857.
- 64 Y. Lum, B. Yue, P. Lobaccaro, A. T. Bell and J. W. Ager, *J. Phys. Chem. C*, 2017, **121**, 14191–14203.
- 65 R. Reske, H. Mistry, F. Beharfarid, B. Roldan Cuenya and P. Strasser, *J. Am. Chem. Soc.*, 2014, **136**, 6978–6986.
- 66 K. J. Schouten, Z. Qin, E. Perez Gallent and M. T. Koper, *J. Am. Chem. Soc.*, 2012, **134**, 9864–9867.
- 67 J. He, K. E. Dettelbach, A. Huang and C. P. Berlinguette, *Angew. Chem., Int. Ed.*, 2017, **56**, 16579–16582.
- 68 C. W. Li, J. Ciston and M. W. Kanan, *Nature*, 2014, **508**, 504–507.
- 69 C. W. Li and M. W. Kanan, *J. Am. Chem. Soc.*, 2012, **134**, 7231–7234.
- 70 A. Verdager-Casadevall, C. W. Li, T. P. Johansson, S. B. Scott, J. T. McKeown, M. Kumar, I. E. Stephens, M. W. Kanan and I. Chorkendorff, *J. Am. Chem. Soc.*, 2015, **137**, 9808–9811.
- 71 X. Feng, K. Jiang, S. Fan and M. W. Kanan, *ACS Cent. Sci.*, 2016, **2**, 169–174.
- 72 R. Kas, R. Kortlever, A. Milbrat, M. T. Koper, G. Mul and J. Baltrusaitis, *Phys. Chem. Chem. Phys.*, 2014, **16**, 12194–12201.
- 73 S. Rasul, D. H. Anjum, A. Jedidi, Y. Minenkov, L. Cavallo and K. Takanabe, *Angew. Chem., Int. Ed.*, 2015, **54**, 2146–2150.
- 74 S. Sarfraz, A. T. Garcia-Esparza, A. Jedidi, L. Cavallo and K. Takanabe, *ACS Catal.*, 2016, **6**, 2842–2851.
- 75 A. Jedidi, S. Rasul, D. Masih, L. Cavallo and K. Takanabe, *J. Mater. Chem. A*, 2015, **3**, 19085–19092.
- 76 J. Choi, M. J. Kim, S. H. Ahn, I. Choi, J. H. Jang, Y. S. Ham, J. J. Kim and S.-K. Kim, *Chem. Eng. J.*, 2016, **299**, 37–44.
- 77 K. Manthiram, B. J. Beberwyck and A. P. Alivisatos, *J. Am. Chem. Soc.*, 2014, **136**, 13319–13325.
- 78 Y. X. Duan, F. L. Meng, K. H. Liu, S. S. Yi, S. J. Li, J. M. Yan and Q. Jiang, *Adv. Mater.*, 2018, **30**, 1706194.
- 79 Y. Pang, T. Burdyny, C. T. Dinh, M. G. Kibria, J. Z. Fan, M. Liu, E. H. Sargent and D. Sinton, *Green Chem.*, 2017, **19**, 4023–4030.
- 80 D. Raciti, K. J. Livi and C. Wang, *Nano Lett.*, 2015, **15**, 6829–6835.
- 81 D. Ren, Y. Deng, A. D. Handoko, C. S. Chen, S. Malkhandi and B. S. Yeo, *ACS Catal.*, 2015, **5**, 2814–2821.
- 82 P. De Luna, R. Quintero-Bermudez, C.-T. Dinh, M. B. Ross, O. S. Bushuyev, P. Todorović, T. Regier, S. O. Kelley, P. Yang and E. H. Sargent, *Nat. Catal.*, 2018, **1**, 103–110.
- 83 B. Kumar, J. P. Brian, V. Atla, S. Kumari, K. A. Bertram, R. T. White and J. M. Spurgeon, *ACS Catal.*, 2016, **6**, 4739–4745.
- 84 D. Ren, B. S.-H. Ang and B. S. Yeo, *ACS Catal.*, 2016, **6**, 8239–8247.
- 85 C. Reller, R. Krause, E. Volkova, B. Schmid, S. Neubauer, A. Rucki, M. Schuster and G. Schmid, *Adv. Energy Mater.*, 2017, **7**, 1602114.
- 86 S. Ma, M. Sadakiyo, M. Heima, R. Luo, R. T. Haasch, J. I. Gold, M. Yamauchi and P. J. Kenis, *J. Am. Chem. Soc.*, 2017, **139**, 47–50.
- 87 T. T. H. Hoang, S. Ma, J. I. Gold, P. J. A. Kenis and A. A. Gewirth, *ACS Catal.*, 2017, **7**, 3313–3321.
- 88 S. Sen, D. Liu and G. T. R. Palmore, *ACS Catal.*, 2014, **4**, 3091–3095.
- 89 M. B. Ross, C. T. Dinh, Y. Li, D. Kim, P. De Luna, E. H. Sargent and P. Yang, *J. Am. Chem. Soc.*, 2017, **139**, 9359–9363.
- 90 C. F. C. Lim, D. A. Harrington and A. T. Marshall, *Electrochim. Acta*, 2017, **238**, 56–63.
- 91 D. M. Weekes, D. A. Salvatore, A. Reyes, A. Huang and C. P. Berlinguette, *Acc. Chem. Res.*, 2018, **51**, 910–918.
- 92 J. Hong, W. Zhang, J. Ren and R. Xu, *Anal. Methods*, 2013, **5**, 1086.
- 93 K. P. Kuhl, E. R. Cave, D. N. Abram and T. F. Jaramillo, *Energy Environ. Sci.*, 2012, **5**, 7050–7059.



- 94 K. J. P. Schouten, Y. Kwon, C. J. Ham, Z. Qin and M. T. M. Koper, *Chem. Sci.*, 2011, **2**, 1902–1909.
- 95 H. Mistry, A. S. Varela, C. S. Bonifacio, I. Zegkinoglou, I. Sinev, Y. W. Choi, K. Kisslinger, E. A. Stach, J. C. Yang, P. Strasser and B. R. Cuenya, *Nat. Commun.*, 2016, **7**, 12123.
- 96 M. Favaro, H. Xiao, T. Cheng, W. A. Goddard III, J. Yano and E. J. Crumlin, *Proc. Natl. Acad. Sci. U. S. A.*, 2017, **114**, 6706–6711.
- 97 Y. Lum and J. W. Ager, *Nat. Catal.*, 2019, **2**, 86–93.
- 98 I. V. Chernyshova, P. Somasundaran and S. Ponnuram, *Proc. Natl. Acad. Sci. U. S. A.*, 2018, **115**, E9261–E9270.
- 99 L. Dai, Q. Qin, P. Wang, X. Zhao, C. Hu, P. Liu, R. Qin, M. Chen, D. Ou, C. Xu, S. Mo, B. Wu, G. Fu, P. Zhang and N. Zheng, *Sci. Adv.*, 2017, **3**, e1701069.
- 100 J. Jiao, R. Lin, S. Liu, W. C. Cheong, C. Zhang, Z. Chen, Y. Pan, J. Tang, K. Wu, S. F. Hung, H. M. Chen, L. Zheng, Q. Lu, X. Yang, B. Xu, H. Xiao, J. Li, D. Wang, Q. Peng, C. Chen and Y. Li, *Nat. Chem.*, 2019, **11**, 222–228.
- 101 E. Bertheussen, A. Verdager-Casadevall, D. Ravasio, J. H. Montoya, D. B. Trimarco, C. Roy, S. Meier, J. Wendland, J. K. Nørskov, I. E. L. Stephens and I. Chorkendorff, *Angew. Chem., Int. Ed.*, 2016, **55**, 1450–1454.
- 102 T. T. H. Hoang, S. Verma, S. Ma, T. T. Fister, J. Timoshenko, A. I. Frenkel, P. J. A. Kenis and A. A. Gewirth, *J. Am. Chem. Soc.*, 2018, **140**, 5791–5797.
- 103 T. Burdyny, C. T. Dinh, M. G. Kibria, A. Seifitokaldani, F. P. G. Arquer, C. M. Gabardo, A. Kiani, P. D. Luna, J. P. Edwards, O. S. Bushuyev, C. Q. Zou, Y. J. Pang, R. Q. Bermudez, D. Sinton and E. H. Sargent, *Science*, 2018, **360**, 783–787.
- 104 Q. Zhu, X. Sun, D. Yang, J. Ma, X. Kang, L. Zheng, L. Zhang, Z. Wu and B. Han, *Nat. Commun.*, 2019, **10**, 3851.
- 105 W. Luc, X. Fu, J. Shi, J. J. Lv, M. Jouny, B. H. Ko, Y. Xu, Q. Tu, X. Hu, J. Wu, Q. Yue, Y. Liu, F. Jiao and Y. Kang, *Nat. Catal.*, 2019, **2**, 423–430.
- 106 J. Kim, W. Choi, J. W. Park, C. Kim, M. Kim and H. Song, *J. Am. Chem. Soc.*, 2019, **141**, 6986–6994.
- 107 Y. Hori, I. Takahashi, O. Koga and N. Hoshi, *J. Phys. Chem. B*, 2002, **106**, 15–17.
- 108 S. Lee, D. Kim and J. Lee, *Angew. Chem., Int. Ed.*, 2015, **54**, 14701–14705.
- 109 T. T. Zhuang, Y. Pang, Z. Q. Liang, Z. Wang, Y. Li, C. S. Tan, J. Li, C. T. Dinh, P. D. Luna, P. L. Hsieh, T. Burdyny, H. H. Li, M. Liu, Y. Wang, F. Li, A. Proppe, A. Johnston, D. H. Nam, Z. Y. Wu, Y. R. Zheng, A. H. Ip, H. Tan, L. J. Chen, S. H. Yu, S. O. Kelley, D. Sinton and E. H. Sargent, *Nat. Catal.*, 2018, **1**, 946–951.
- 110 Y. Zheng, A. Vasileff, X. Zhou, Y. Jiao, M. Jaroniec and S. Z. Qiao, *J. Am. Chem. Soc.*, 2019, **141**, 7646–7659.
- 111 M. B. Ross, P. De Luna, Y. Li, C.-T. Dinh, D. Kim, P. Yang and E. H. Sargent, *Nat. Catal.*, 2019, **2**, 648–658.
- 112 D. Gao, R. M. Arán-Ais, H. S. Jeon and B. R. Cuenya, *Nat. Catal.*, 2019, **2**, 198–210.
- 113 Y. Y. Birdja, E. Pérez-Gallent, M. C. Figueiredo, A. J. Göttle, F. Calle-Vallejo and M. T. M. Koper, *Nat. Energy*, 2019, **4**, 732–745.
- 114 W. Tang, A. A. Peterson, A. S. Varela, Z. P. Jovanov, L. Bech, W. J. Durand, S. Dahl, J. K. Nørskov and I. Chorkendorff, *Phys. Chem. Chem. Phys.*, 2012, **14**, 76–81.
- 115 Y. L. Qiu, H. X. Zhong, T. T. Zhang, W. B. Xu, X. F. Li and H. M. Zhang, *ACS Catal.*, 2017, **7**, 6302–6310.
- 116 C. W. Kung, C. O. Audu, A. W. Peters, H. Noh, O. K. Farha and J. T. Hupp, *ACS Energy Lett.*, 2017, **2**, 2394–2401.
- 117 O. A. Baturina, Q. Lu, M. A. Padilla, L. Xin, W. Li, A. Serov, K. Artyushkova, P. Atanassov, F. Xu, A. Epshteyn, T. Brintlinger, M. Schuette and G. E. Collins, *ACS Catal.*, 2014, **4**, 3682–3695.
- 118 H. Mistry, A. S. Varela, S. Kühl, P. Strasser and B. R. Cuenya, *Nat. Rev. Mater.*, 2016, **1**, 16009.
- 119 H. Mistry, F. Behafarid, R. Reske, A. S. Varela, P. Strasser and B. R. Cuenya, *ACS Catal.*, 2016, **6**, 1075–1080.
- 120 X. L. Wang, A. S. Varela, A. Bergmann, S. Kehl and P. Strasser, *ChemSusChem*, 2017, **10**, 4642–4649.
- 121 H. Jung, S. Y. Lee, C. W. Lee, M. K. Cho, D. H. Won, C. Kim, H. S. Oh, B. K. Min and Y. J. Hwang, *J. Am. Chem. Soc.*, 2019, **141**, 4624–4633.
- 122 D. Kim, C. S. Kley, Y. Li and P. Yang, *Proc. Natl. Acad. Sci. U. S. A.*, 2017, **114**, 10560–10565.
- 123 C. Choi, T. Cheng, M. F. Espinosa, H. Fei, X. Duan, W. A. Goddard and Y. Huang, *Adv. Mater.*, 2019, **31**, e1805405.
- 124 H. S. Jeon, S. Kunze, F. Scholten and B. Roldan Cuenya, *ACS Catal.*, 2018, **8**, 531–535.
- 125 J. Chung, D. H. Won, J. Koh, E.-H. Kim and S. I. Woo, *Phys. Chem. Chem. Phys.*, 2016, **18**, 6252–6258.
- 126 H. Jiang, Z. Hou and Y. Luo, *Angew. Chem.*, 2017, **56**, 15617–15621.
- 127 S. L. Chu, S. Hong, J. Masa, X. Lia and Z. Y. Sun, *Chem. Commun.*, 2019, **55**, 12380–12383.
- 128 S. J. Huo, Z. Weng, Z. S. Wu, Y. R. Zhong, Y. S. Wu, J. H. Fang and H. L. Wang, *ACS Appl. Mater. Interfaces*, 2017, **9**, 28519–28526.
- 129 A. Loiudice, P. Lobaccaro, E. A. Kamali, T. Thao, B. H. Huang, J. W. Ager and R. Buonsanti, *Angew. Chem., Int. Ed.*, 2016, **55**, 5789–5792.
- 130 Y. Li, F. Cui, M. B. Ross, D. Kim, Y. Sun and P. Yang, *Nano Lett.*, 2017, **17**, 1312–1317.
- 131 A. Dutta, M. Rahaman, N. C. Luedi, M. Mohos and P. Broekmann, *ACS Catal.*, 2016, **6**, 3804–3814.
- 132 A. Dutta, M. Rahaman, M. Mohos, A. Zanetti and P. Broekmann, *ACS Catal.*, 2017, **7**, 5431–5437.
- 133 K. D. Yang, W. R. Ko, J. H. Lee, S. J. Kim, H. Lee, M. H. Lee and K. T. Nam, *Angew. Chem., Int. Ed.*, 2017, **56**, 796–800.
- 134 M. Ma, K. Djanashvili and W. A. Smith, *Angew. Chem., Int. Ed.*, 2016, **55**, 6680–6684.
- 135 J. J. Lv, M. Jouny, W. Luc, W. Zhu, J. J. Zhu and F. Jiao, *Adv. Mater.*, 2018, **30**, 1803111.
- 136 M. Ma, K. Djanashvili and W. A. Smith, *Phys. Chem. Chem. Phys.*, 2015, **17**, 20861–20867.
- 137 Z. Wang, G. Yang, Z. Zhang, M. Jin and Y. Yin, *ACS Nano*, 2016, **10**, 4559–4564.
- 138 W. Luo, X. Nie, M. J. Janik and A. Asthagiri, *ACS Catal.*, 2016, **6**, 219–229.



- 139 K. J. P. Schouten, E. Pérez Gallent and M. T. M. Koper, *ACS Catal.*, 2013, **3**, 1292–1295.
- 140 F. Calle-Vallejo and M. T. Koper, *Angew. Chem., Int. Ed.*, 2013, **52**, 7282–7285.
- 141 Y. Huang, A. D. Handoko, P. Hirunsit and B. S. Yeo, *ACS Catal.*, 2017, **7**, 1749–1756.
- 142 Y. Kwon, Y. Lum, E. L. Clark, J. W. Ager and A. T. Bell, *ChemElectroChem*, 2016, **3**, 1012–1019.
- 143 Y. Lum and J. W. Ager, *Angew. Chem., Int. Ed.*, 2018, **57**, 551–554.
- 144 D. Raciti, L. Cao, K. J. T. Livi, P. F. Rottmann, X. Tang, C. Li, Z. Hicks, K. H. Bowen, K. J. Hemker, T. Mueller and C. Wang, *ACS Catal.*, 2017, **7**, 4467–4472.
- 145 L. Cao, D. Raciti, C. Li, K. J. T. Livi, P. F. Rottmann, K. J. Hemker, T. Mueller and C. Wang, *ACS Catal.*, 2017, **7**, 8578–8587.
- 146 A. D. Handoko, K. W. Chan and B. S. Yeo, *ACS Energy Lett.*, 2017, **2**, 2103–2109.
- 147 A. Eilert, F. S. Roberts, D. Friebe and A. Nilsson, *J. Phys. Chem. Lett.*, 2016, **7**, 1466–1470.
- 148 A. J. Garza, A. T. Bell and M. Head-Gordon, *J. Phys. Chem. Lett.*, 2018, **9**, 601–606.
- 149 D. Gao, I. Zegkinoglou, N. J. Divins, F. Scholten, I. Sinev, P. Grosse and B. R. Cuenya, *ACS Nano*, 2017, **11**, 4825–4831.
- 150 D. Kim, S. Lee, J. D. Ocon, B. Jeong, J. K. Lee and J. Lee, *Phys. Chem. Chem. Phys.*, 2015, **17**, 824–830.
- 151 A. Eilert, F. Cavalca, F. S. Roberts, J. Osterwalder, C. Liu, M. Favaro, E. J. Crumlin, H. Ogasawara, D. Friebe, L. G. Pettersson and A. Nilsson, *J. Phys. Chem. Lett.*, 2017, **8**, 285–290.
- 152 C. Liu, M. P. Lourenço, S. Hedström, F. Cavalca, O. Diaz-Morales, H. A. Duarte, A. Nilsson and L. G. M. Pettersson, *J. Phys. Chem. C*, 2017, **121**, 25010–25017.
- 153 H. Xiao, W. A. Goddard III, T. Cheng and Y. Liu, *Proc. Natl. Acad. Sci. U. S. A.*, 2017, **114**, 6685–6688.
- 154 D. Bourissou, *Nat. Chem.*, 2019, **11**, 199–200.
- 155 J. Qiao, P. Jiang, J. Liu and J. Zhang, *Electrochem. Commun.*, 2014, **38**, 8–11.
- 156 M. Rahaman, A. Dutta, A. Zanetti and P. Broekmann, *ACS Catal.*, 2017, **7**, 7946–7956.
- 157 F. S. Roberts, K. P. Kuhl and A. Nilsson, *Angew. Chem., Int. Ed.*, 2015, **54**, 5179–5182.
- 158 F. S. Roberts, K. P. Kuhl and A. Nilsson, *ChemCatChem*, 2016, **8**, 1119–1124.
- 159 C. S. Chen, A. D. Handoko, J. H. Wan, L. Ma, D. Ren and B. S. Yeo, *Catal. Sci. Technol.*, 2015, **5**, 161–168.
- 160 S. Lee, D. Kim and J. Lee, *Angew. Chem., Int. Ed.*, 2015, **54**, 14701–14705.
- 161 A. Engelbrecht, M. Hämmerle, R. Moos, M. Fleischer and G. Schmid, *Electrochim. Acta*, 2017, **224**, 642–648.
- 162 J. Lee and Y. Tak, *Electrochim. Acta*, 2001, **46**, 3015–3022.
- 163 C. S. L. Duff, M. J. Lawrence and P. Rodriguez, *Angew. Chem., Int. Ed.*, 2017, **56**, 12919–12924.
- 164 E. Bertheussen, T. V. Hogg, Y. Abghoui, A. K. Engstfeld, I. Chorkendorff and I. E. L. Stephens, *ACS Energy Lett.*, 2018, **3**, 634–640.
- 165 M. Watanabe, M. Shibata, A. Kato, M. Azuma and T. Sakata, *J. Electrochem. Soc.*, 1991, **138**, 3382–3389.
- 166 Z. B. Hoffman, T. S. Gray, K. B. Moraveck, T. B. Gunnoe and G. Zangari, *ACS Catal.*, 2017, **7**, 5381–5390.
- 167 J. Christophe, T. Doneux and C. Buess-Herman, *Electrocatalysis*, 2012, **3**, 139–146.
- 168 W. Zhao, L. Yang, Y. Yin and M. Jin, *J. Mater. Chem. A*, 2014, **2**, 902–906.
- 169 S. Zhang, P. Kang, M. Bakir, A. M. Lapidés, C. J. Dares and T. J. Meyer, *Proc. Natl. Acad. Sci. U. S. A.*, 2015, **112**, 15809–15814.
- 170 Y. Wang, D. Wang, C. J. Dares, S. L. Marquard, M. V. Sheridan and T. J. Meyer, *Proc. Natl. Acad. Sci. U. S. A.*, 2018, **115**, 278–283.
- 171 J. He, K. E. Dettelbach, D. A. Salvatore, T. Li and C. P. Berlinguette, *Angew. Chem., Int. Ed.*, 2017, **56**, 6068–6072.
- 172 D. Kim, J. Resasco, Y. Yu, A. M. Asiri and P. Yang, *Nat. Commun.*, 2014, **5**, 4948.
- 173 M. Li, J. Wang, P. Li, K. Chang, C. Li, T. Wang, B. Jiang, H. Zhang, H. Liu, Y. Yamauchi, N. Umezawa and J. Ye, *J. Mater. Chem. A*, 2016, **4**, 4776–4782.
- 174 Z. Yin, D. Gao, S. Yao, B. Zhao, F. Cai, L. Lin, P. Tang, P. Zhai, G. Wang, D. Ma and X. Bao, *Nano Energy*, 2016, **27**, 35–43.
- 175 S. Back, J. H. Kim, Y. T. Kim and Y. Jung, *ACS Appl. Mater. Interfaces*, 2016, **8**, 23022–23027.
- 176 T. Takashima, T. Suzuki and H. Irie, *Electrochim. Acta*, 2017, **229**, 415–421.
- 177 S. Lee, G. Park and J. Lee, *ACS Catal.*, 2017, **7**, 8594–8604.
- 178 B. Jermann and J. Augustynski, *Electrochim. Acta*, 1994, **39**, 1891–1896.
- 179 G. Kyriacou and A. Anagnostopoulos, *J. Electroanal. Chem.*, 1992, **322**, 233–246.
- 180 G. O. Larrazábal, A. J. Martín, S. Mitchell, R. Hauert and J. Pérez-Ramírez, *ACS Catal.*, 2016, **6**, 6265–6274.
- 181 T. Shinagawa, G. O. Larrazábal, A. J. Martín, F. Krumeich and J. Pérez-Ramírez, *ACS Catal.*, 2018, **8**, 837–844.
- 182 M. S. Xie, B. Y. Xia, Y. W. Li, Y. Yan, Y. H. Yang, Q. Sun, S. H. Chan, A. Fisher and X. Wang, *Energy Environ. Sci.*, 2016, **9**, 1687–1695.
- 183 S. Ahn, K. Klyukin, R. J. Wakeham, J. A. Rudd, A. R. Lewis, S. Alexander, F. Carla, V. Alexandrov and E. Andreoli, *ACS Catal.*, 2018, **8**, 4132–4142.
- 184 H. J. Yang, H. Yang, Y. H. Hong, P. Y. Zhang, T. Wang, L. N. Chen, F. Y. Zhang, Q. H. Wu, N. Tian, Z. Y. Zhou and S. G. Sun, *ChemSusChem*, 2018, **11**, 881–887.
- 185 T. T. Zhuang, Z. Q. Liang, A. Seifitokaldani, Y. Li, P. De Luna, T. Burdyny, F. Che, F. Meng, Y. Min, R. Quintero-Bermudez, C. T. Dinh, Y. Pang, M. Zhong, B. Zhang, J. Li, P. N. Chen, X. L. Zheng, H. Liang, W. N. Ge, B. J. Ye, D. Sinton, S. H. Yu and E. H. Sargent, *Nat. Catal.*, 2018, **1**, 421–428.
- 186 Z. Q. Liang, T. T. Zhuang, A. Seifitokaldani, J. Li, C. W. Huang, C. S. Tan, Y. Li, P. De Luna, C. T. Dinh, Y. Hu, Q. Xiao, P. L. Hsieh, Y. Wang, F. Li, R. Quintero-Bermudez, Y. Zhou, P. Chen, Y. Pang, S. C. Lo, L. J. Chen,





- H. Tan, Z. Xu, S. Zhao, D. Sinton and E. H. Sargent, *Nat. Commun.*, 2018, **9**, 3828.
- 187 A. Murata and Y. Hori, *Bull. Chem. Soc. Jpn.*, 1991, **64**, 123–127.
- 188 M. R. Singh, Y. Kwon, Y. Lum, J. W. Ager and A. T. Bell, *J. Am. Chem. Soc.*, 2016, **138**, 13006–13012.
- 189 J. Resasco, L. D. Chen, E. Clark, C. Tsai, C. Hahn, T. F. Jaramillo, K. Chan and A. T. Bell, *J. Am. Chem. Soc.*, 2017, **139**, 11277–11287.
- 190 E. Perez-Gallent, G. Marcandalli, M. C. Figueiredo, F. Calle-Vallejo and M. T. M. Koper, *J. Am. Chem. Soc.*, 2017, **139**, 16412–16419.
- 191 A. S. Varela, W. Ju, T. Reier and P. Strasser, *ACS Catal.*, 2016, **6**, 2136–2144.
- 192 S. Q. Zhu, B. Jiang, W. B. Cai and M. H. Shao, *J. Am. Chem. Soc.*, 2017, **139**, 15664–15667.
- 193 S. Ikeda, T. Takagi and K. Ito, *Bull. Chem. Soc. Jpn.*, 1987, **60**, 2517–2522.
- 194 C. Amatore and J. M. Saveant, *J. Am. Chem. Soc.*, 1981, **103**, 5021–5023.
- 195 Y. Tomita, S. Teruya, O. Koga and Y. Horiz, *J. Electrochem. Soc.*, 2000, **147**, 4164–4167.
- 196 T. N. Huan, E. S. Andreiadis, J. Heidkamp, P. Simon, E. Derat, S. Cobo, G. Royal, A. Bergmann, P. Strasser, H. Dau, V. Artero and M. Fontecave, *J. Mater. Chem. A*, 2015, **3**, 3901–3907.
- 197 T. N. Huan, P. Simon, A. Benayad, L. Guetaz, V. Artero and M. Fontecave, *Chem.–Eur. J.*, 2016, **22**, 14029–14035.
- 198 M. C. Figueiredo, I. Ledezma-Yanez and M. T. M. Koper, *ACS Catal.*, 2016, **6**, 2382–2392.
- 199 J. Zhao, L. Sun, S. Canepa, H. Sun, M. N. Yesibolati, M. Sherburne, R. Xu, T. Sritharan, J. S. C. Loo, J. W. Ager III, J. Barber, K. Møhlhave and Z. J. Xu, *J. Mater. Chem. A*, 2017, **5**, 11905–11916.
- 200 S. Zeng, X. Zhang, L. Bai, X. Zhang, H. Wang, J. Wang, D. Bao, M. Li, X. Liu and S. Zhang, *Chem. Rev.*, 2017, **117**, 9625–9673.
- 201 B. A. Rosen, A. Salehi-Khojin, M. R. Thorson, W. Zhu, D. T. Whipple, P. J. Kenis and R. I. Masel, *Science*, 2011, **334**, 643–644.
- 202 J. L. DiMeglio and J. Rosenthal, *J. Am. Chem. Soc.*, 2013, **135**, 8798–8801.
- 203 J. Medina-Ramos, J. L. DiMeglio and J. Rosenthal, *J. Am. Chem. Soc.*, 2014, **136**, 8361–8367.
- 204 A. Atifi, D. W. Boyce, J. L. DiMeglio and J. Rosenthal, *ACS Catal.*, 2018, **8**, 2857–2863.
- 205 N. Roy, Y. Shibano, C. Terashima, K.-i. Katsumata, K. Nakata, T. Kondo, M. Yuasa and A. Fujishima, *ChemElectroChem*, 2016, **3**, 1044–1047.
- 206 T. N. Huan, P. Simon, G. Rousse, I. Génois, V. Artero and M. Fontecave, *Chem. Sci.*, 2017, **8**, 742–747.
- 207 L. Wang, S. A. Nitopi, E. Bertheussen, M. Orazov, C. G. Morales-Guio, X. Liu, D. C. Higgins, K. Chan, J. K. Nørskov, C. Hahn and T. F. Jaramillo, *ACS Catal.*, 2018, **8**, 7445–7454.
- 208 H. Xiang, S. Rasul, K. Scott, J. Portoles, P. Cumpson and E. H. Yu, *J. CO<sub>2</sub> Util.*, 2019, **30**, 214–221.
- 209 Z. F. Chen, P. Kang, M. T. Zhang, B. R. Stoner and T. J. Meyer, *Energy Environ. Sci.*, 2013, **6**, 813–817.
- 210 D. A. Vermaas and W. A. Smith, *ACS Energy Lett.*, 2016, **1**, 1143–1148.
- 211 G. Centi and S. Perathoner, *ChemSusChem*, 2010, **3**, 195–208.
- 212 B. Kumar, M. Llorente, J. Froehlich, T. Dang, A. Sathrum and C. P. Kubiak, *Annu. Rev. Phys. Chem.*, 2012, **63**, 541–569.
- 213 T. Baran, S. Wojtyla, A. Dibenedetto, M. Aresta and W. Macyk, *ChemSusChem*, 2016, **9**, 2933–2938.
- 214 T. Zhang, J. Low, X. Huang, J. F. Al-Sharab, J. Yu and T. Asefa, *ChemCatChem*, 2017, **9**, 3054–3062.
- 215 G. Yin, M. Nishikawa, Y. Nosaka, N. Srinivasan, D. Atarashi, E. Sakai and M. Miyauchi, *ACS Nano*, 2015, **9**, 2111–2119.
- 216 S. Neatu, J. A. Macia-Agullo, P. Concepcion and H. Garcia, *J. Am. Chem. Soc.*, 2014, **136**, 15969–15976.
- 217 L. Yu, G. Li, X. Zhang, X. Ba, G. Shi, Y. Li, P. K. Wong, J. C. Yu and Y. Yu, *ACS Catal.*, 2016, **6**, 6444–6454.
- 218 G. Ghadimkhani, N. R. de Tacconi, W. Chanmanee, C. Janaky and K. Rajeshwar, *Chem. Commun.*, 2013, **49**, 1297–1299.
- 219 K. Rajeshwar, N. R. de Tacconi, G. Ghadimkhani, W. Chanmanee and C. Janaky, *ChemPhysChem*, 2013, **14**, 2251–2259.
- 220 X. Yang, E. A. Fugate, Y. Mueanngern and L. R. Baker, *ACS Catal.*, 2017, **7**, 177–180.
- 221 Q. Kong, D. Kim, C. Liu, Y. Yu, Y. Su, Y. Li and P. Yang, *Nano Lett.*, 2016, **16**, 5675–5680.
- 222 G. Magesh, E. S. Kim, H. J. Kang, M. Banu, J. Y. Kim, J. H. Kim and J. S. Lee, *J. Mater. Chem. A*, 2014, **2**, 2044–2049.
- 223 G. Yin, H. Abe, R. Kodiyath, S. Ueda, N. Srinivasan, A. Yamaguchi and M. Miyauchi, *J. Mater. Chem. A*, 2017, **5**, 12113–12119.
- 224 C. W. Kim, M. J. Kang, S. Ji and Y. S. Kang, *ACS Catal.*, 2018, **8**, 968–974.
- 225 X. Chang, T. Wang, P. Zhang, Y. Wei, J. Zhao and J. Gong, *Angew. Chem., Int. Ed.*, 2016, **55**, 8840–8845.
- 226 J. Zhao, X. Wang, Z. C. Xu and J. S. Loo, *J. Mater. Chem. A*, 2014, **2**, 15228–15233.
- 227 X. Liu, S. Inagaki and J. Gong, *Angew. Chem., Int. Ed.*, 2016, **55**, 14924–14950.
- 228 M. K. Brennaman, R. J. Dillon, L. Alibabaei, M. K. Gish, C. J. Dares, D. L. Ashford, R. L. House, G. J. Meyer, J. M. Papanikolas and T. J. Meyer, *J. Am. Chem. Soc.*, 2016, **138**, 13085–13102.
- 229 M. Schreier, J. Luo, P. Gao, T. Moehl, M. T. Mayer and M. Grätzel, *J. Am. Chem. Soc.*, 2016, **138**, 1938–1946.
- 230 M. R. Singh, E. L. Clark and A. T. Bell, *Proc. Natl. Acad. Sci. U. S. A.*, 2015, **112**, E6111–E6118.
- 231 M. Aresta, A. Dibenedetto and A. Angelini, *J. CO<sub>2</sub> Util.*, 2013, **3–4**, 65–73.
- 232 C. Ampelli, G. Centi, R. Passalacqua and S. Perathoner, *Energy Environ. Sci.*, 2010, **3**, 292–301.
- 233 J. L. White, M. F. Baruch, J. E. Pander III, Y. Hu, I. C. Fortmeyer, J. E. Park, T. Zhang, K. Liao, J. Gu,



- Y. Yan, T. W. Shaw, E. Abelev and A. B. Bocarsly, *Chem. Rev.*, 2015, **115**, 12888–12935.
- 234 A. J. Bard and M. A. Fox, *Acc. Chem. Res.*, 1995, **28**, 141–145.
- 235 C. Delacourt, P. L. Ridgway, J. B. Kerr and J. Newman, *J. Electrochem. Soc.*, 2008, **155**, B42.
- 236 C. Janáky, D. Hursán, B. Endrődi, W. Chanmanee, D. Roy, D. Liu, N. R. de Tacconi, B. H. Dennis and K. Rajeshwar, *ACS Energy Lett.*, 2016, **1**, 332–338.
- 237 A. Marimuthu, J. Zhang and S. Linic, *Science*, 2013, **339**, 1590–1593.
- 238 X. Guo, C. Hao, G. Jin, H. Y. Zhu and X. Y. Guo, *Angew. Chem., Int. Ed.*, 2014, **53**, 1973–1977.
- 239 S. Zhao, R. Jin and R. Jin, *ACS Energy Lett.*, 2018, **3**, 452–462.
- 240 D. S. Ripatti, T. R. Veltman and M. W. Kanan, *Joule*, 2018, **3**, 1–7.
- 241 Y. Mun, S. Lee, A. Cho, S. Kim, J. W. Han and J. Lee, *Appl. Catal., B*, 2019, **246**, 82–88.

